

Felix Widmann
Master Thesis

P-REX: A PISTON RECONSTRUCTION EXPERIMENT FOR LARGE OPTICAL INTERFEROMETERS

A Master Thesis in Physics at Heidelberg University, conducted
at the Max Planck Institute for Astronomy in Heidelberg



Department of Physics and Astronomy

HEIDELBERG UNIVERSITY

Master Thesis in Physics
submitted by

Felix Benjamin Widmann

born in Stuttgart (Germany)

2017

Image on cover page from: ESO/S. Brunier

Felix Widmann: P-REx: a piston reconstruction experiment for large optical interferometers

This Master Thesis has been carried out at the
Max Planck Institute for Astronomy, Heidelberg

Under the supervision of
Dr. Jörg-Uwe Pott
(Max Planck Institute for Astronomy, Heidelberg)
and
Prof. Dr. Andreas Quirrenbach
(Landessternwarte, Heidelberg)

Examined by
Prof. Dr. Andreas Quirrenbach
(Landessternwarte, Heidelberg)
and
Prof. Dr. Lucas Labadie
(I. Physicalisches Institut, Köln)

ABSTRACT — ENGLISH

For infrared and optical interferometry, one of the main limitations is the continuous change in the optical path, introduced by the piston variation due to a turbulent atmosphere. The differential piston between the telescopes limits the coherence and therefore the sensitivity of the interferometer and is classically controlled by the use of a fringe tracker. In this work, I develop a method, called Piston Reconstruction Experiment (P-REx), to reconstruct the temporal piston variation. This method uses real-time data from adaptive optics wavefront sensing. In this work the P-REx algorithms are extensively tested, both in realistic end-to-end simulations and with real data from the Large Binocular Telescope (LBT). The goal for these tests is to demonstrate the benefit of using P-REx as an auxiliary system in a real interferometer. By stabilizing the fringe position with P-REx over short timescales, one allows longer exposure times for the fringe tracker, which improves its sensitivity.

In order to understand the principle performance of the system in a realistic multilayer atmosphere and to optimize the algorithms, it is first extensively tested in simulations. This includes a wide study of parameter ranges for the adaptive optics system and the atmosphere. By doing this I find the required conditions for the piston reconstruction to work. The insights from the simulations are then used to apply P-REx to real data, where the performance can be tested under real conditions.

All the tests on simulations and real data show positive results, which encourage a real implementation of P-REx. Especially the tests on real data showed that the atmosphere is, under decent observing conditions, sufficiently well structured and stable, in order to apply the piston drift reconstruction. In the used data it is possible to conveniently reconstruct the piston evolution in two thirds of the available datasets from good observing conditions. The main conclusion of my work is that applying the P-REx algorithms in a real system would reduce the piston variation down to 1 to 2 μm over timescales of up to two seconds. This suggests an application of P-REx for mid-infrared interferometry, for example for MATISSE at the VLTI or the LBTI.

ABSTRACT — DEUTSCH

Eine der größten Einschränkungen der Interferometrie bei optischen und nah-infraroten Wellenlängen ist die kontinuierliche Veränderung der optischen Weglänge, hervorgerufen durch die Veränderung des Pistons (über die Apertur gemittelte Phase) in der Atmosphäre. Der sich verändernde Gangunterschied zwischen den Teleskopen reduziert die Empfindlichkeit des Interferometers und wird üblicherweise durch einen Fringe Tracker reguliert. Mit dieser Arbeit entwickle ich eine neue Methode um die Veränderung des Pistons mithilfe der Daten eines adaptiven optischen Systems in Echtzeit zu rekonstruieren: das Piston Rekonstruktions Experiment (kurz: P-REx). In dieser Arbeit werden die P-REx Algorithmen intensiv mit Simulationen und realen Daten vom Large Binocular Telescope (LBT) getestet. Das Ziel dieser Tests ist es zu zeigen, dass man P-REx als zusätzliches System nutzen kann, um die Position des Interferenzmusters über kurze Zeiträume stabil zu halten. Dadurch kann die Belichtungszeit des Fringe Trackers verlängert werden, was dessen Empfindlichkeit erhöht.

Um die allgemeinen Möglichkeiten von P-REx besser zu verstehen und um die Algorithmen zu verbessern, teste ich es zuerst an simulierten Daten mit einer realistischen, vielschichtigen Atmosphäre. Diese Tests beinhalten auch eine breite Studie von Eigenschaften des adaptiven optischen Systems und der Atmosphäre, um zu testen welche Voraussetzungen für die Piston Rekonstruktion nötig sind. Mithilfe der Erkenntnisse der Simulationen wird P-REx dann auf reale Daten angewendet, um die Performance unter realen Bedingungen zu testen.

Insgesamt sind die Resultate von Simulationen und realen Daten vielversprechend und bestärken den Einsatz von P-REx. Ein wichtiges Resultat der realen Daten ist dabei, dass die Atmosphäre bei guten Bedingungen stabil und strukturiert genug ist, um die Piston Rekonstruktion anzuwenden. In den vorhandenen Daten konnte die Piston Entwicklung in zwei dritteln der Datensets mit guten Beobachtungsbedingungen rekonstruiert werden. Die zentrale Schlussfolgerung dieser Arbeit ist daher, dass durch die Anwendung von P-REx in einem realen System die Piston Schwankung in einem Zeitraum von zwei Sekunden auf 1 bis 2 μm reduziert werden kann. Diese Werte legen eine Anwendung von P-REx bei mittleren infraroten Wellenlängen nahe, zum Beispiel für MATISSE am VLTI oder für das LBTI.

ACKNOWLEDGMENTS

As this thesis marks the final chapter of my studies in Heidelberg, I want to take this opportunity to thank all the people who took this path with me and supported me during this time. This especially includes everybody who helped me with this work by offering advice and help, or just encouraged me by discussing my research.

I especially want to thank my two examiners Prof. Andreas Quirrenbach and Prof. Lucas Labadie who agreed to examine and also partially supervise this thesis without great benefits for their own works. Without their effort it would not be possible for me to conduct this thesis and I am deeply grateful for this opportunity. Furthermore, I thank Jörg-Uwe Pott, firstly for offering me this thesis project, but also for all the support and help during the last year and for the great supervision of my work.

During the time of my thesis, I worked with a lot of different tools and datasets and received input from many people to mention them all. Therefore, I thank everybody who helped me understand and use different datasets or master all the occurring problems in different software tools.

Likewise, I thank everybody who helps random people via the Internet, either by posting code on GitHub, or by answering questions in countless forums. Without you, today's student life would be much more difficult!

CONTENTS

List of Abbreviations	ix
---------------------------------	----

SETTING THE STAGE

1 Introduction	3
2 Atmospheric Turbulence	5
2.1 The Atmosphere in astronomical observations	5
2.2 Turbulence models	6
2.3 Taylor's Frozen Flow Hypothesis	10
3 Adaptive Optics	15
3.1 Basics of Adaptive Optics	15
3.2 Wavefront Sensor	16
3.3 Deformable Mirror	19
3.4 Complex AO systems	20
3.5 AO systems at LBT & VLTI	21
4 Optical Interferometry	23
4.1 Basic Theory	23
4.2 Optical interferometry	27
4.3 Fringe Tracker	29
5 Piston Reconstruction	35
5.1 Motivation	35
5.2 P-REx	36

WORKING WITH SIMULATIONS

6 Yorick Adaptive Optics	45
7 Wind Vector determination	47
7.1 Normalized Cross Correlation	47
7.2 Wind vector from WFS measurements	52
8 First Results	57

8.1	Comparing the two algorithms	57
8.2	Error considerations	62
8.3	Single and multilayer atmosphere	70
9	Realistic AO systems	71
9.1	Single-Conjugated Adaptive Optics	71
9.2	Ground Layer Adaptive Optics	74
9.3	Multi-Conjugated Adaptive Optics	77
9.4	Conclusion from simulations	78
WORKING WITH LBT DATA		
10	Wind vector measurement	81
10.1	Introduction to the data	81
10.2	Wind measurement	83
10.3	Boiling	84
11	Piston reconstruction	87
11.1	Principle of the verification method	87
11.2	Test on simulation	89
11.3	Results from LBT data	91
11.4	Conclusion from LBT data	95
12	Conclusion and Outlook	97
APPENDICES		
A	Zernike Reconstruction	101
B	Code examples	103
B.1	Wind detection	103
B.2	P-REx	104
C	YAO parameter files	107
C.1	SCAO system	107
C.2	GLAO system	108
List of Figures		
		111
List of Tables		
		113
Bibliography		
		115

LIST OF ABBREVIATIONS

AO	adaptive optics
AT	Auxiliary Telescopes
CM	control matrix
DM	deformable mirror
ELT	Extremely Large Telescope
FFT	fast Fourier transformation
FLAO	first light AO
FWHM	full width at half maximum
GLAO	ground layer adaptive optics
IM	interaction matrix
LBT	Large Binocular Telescope
LBTI	Large Binocular Telescope Interferometer
LGS	laser guide star
MCAO	multi-conjugated adaptive optics
MIR	mid-infrared
NGS	natural guide star
NIR	near-infrared
OPD	optical path difference
P-REx	Piston Reconstruction Experiment
POL	pseudo open loop
PSD	power spectral density
RMS	root-mean-square
RMSE	root-mean-square error

SCAO	single-conjugated adaptive optics
SH WFS	Shack-Hartmann wavefront sensor
SNR	signal-to-noise ratio
TFFH	Taylor's Frozen Flow Hypothesis
UT	Unit Telescope
VLT	Very Large Telescope
VLTI	Very Large Telescope Interferometer
WFS	wavefront sensor
YAO	Yorick Adaptive Optics simulation

Part I

SETTING THE STAGE

INTRODUCTION

1

With the second generation of instruments coming up to the Very Large Telescope Interferometer (VLTI) and the Large Binocular Telescope (LBT), the optical and near-infrared interferometry keeps improving. This progress in interferometry helps to explore new limits for ground-based observation with telescopes of the 8 m class. However, one of the main difficulties for ground-based interferometry is still the random and fast changing piston drift over the individual telescopes, introduced by the atmospheric turbulence. This problem of changing piston values is usually approached using fringe trackers, which measure the movement of the interferometric fringes. Despite the crucial importance of these systems, the principle of fringe tracking has some disadvantages concerning the sensitivity of the instrument. Due to this lack in sensitivity modern fringe tracking systems still tend to have instabilities and strong magnitude restrictions for the guide stars.

With this project, I want to develop and test an auxiliary method, which uses the real-time data from adaptive optics (AO) wavefront sensing, to reconstruct the atmospheric piston drift over a single telescope: the Piston Reconstruction Experiment (P-REx). When such a system works properly, a piston reconstruction at the individual telescopes can be used to improve the performance of the fringe tracker. Essentially the proposed algorithm will predict in which direction the fringe moves according to the data from the AO system. With this information the fringes can be kept stable over short timescales and the integration time of the fringe tracker can be extended. This would decrease the problems of fringe trackers and would ultimately improve the sensitivity of the interferometer. The improvement of the sensitivity comes from the increasing coherence time in comparison to the currently implemented approach of direct fringe tracking. This in turn allows for longer integration times at the science camera. Furthermore, it could increase the magnitude limit of fringe tracking guide stars, which would open the possibility of optical interferometry for an increasing number of science cases.

The scientific goal is therefore to increase the sensitivity of an AO supported optical interferometer, in order to observe larger, statistically relevant samples of rare objects, like massive young stars and active galactic nuclei (AGN). In addition, the goal is to reach new target classes like brown dwarfs and microquasars, currently out of reach for optical interferometry.

A key advantage of this method is the fact that no additional hardware is needed, if the interferometer is already equipped with a piston-neutral AO system, fast delay lines, and a fringe tracking system, as it is the case for the up-to-date optical interferometers, such as the VLTI and the LBT.

The Piston Reconstruction Experiment uses the time series of AO wavefront information, to reconstruct the atmospheric piston variation. The core of this algorithm, to get the

piston variation from AO wavefront information, is to derive the dominant wind speed and direction, using the frozen atmosphere approximation. Combining wind and atmospheric tip-tilt information then gives the piston drift. In a previous work by Pott et al. (2016), it has already been demonstrated that the concept works for multi-layer turbulence with uncorrelated wind speeds and turbulence between the layers. In their idealized simulations, the piston reconstruction delivered good results for an atmosphere with three layers of turbulence with different wind speeds and strengths. The simulation showed that this method can retrieve the wind speed and direction of the ground layer precisely. With my work, I expand their simulation to a realistic end-to-end model and ultimately to first tests on real data.

In the following work, I introduce the basic principles of atmospheric turbulence (chapter 2), adaptive optics (chapter 3), and optical interferometry (chapter 4), in order to set the ground for the actual concept. This eventually leads to the possible improvements for fringe trackers (section 4.3) and furthermore to the motivation and description of P-REx in chapter 5. The second part of this work (chapter 7 - 9) is dedicated to show the functionality of P-REx, as well as its limits in realistic simulations. In order to explore these limits I do a wide study of parameter ranges of the atmosphere and wavefront sensors to understand under which conditions the P-REx algorithm can work. The work is then concluded by applying the algorithms to real data from the LBT first light AO (FLAO) system (chapter 10 - 11). This leads to a final conclusion about the abilities of P-REx and an outlook to further possibilities in chapter 12.

ATMOSPHERIC TURBULENCE

2

In order to understand the problems that are addressed with this work, it is crucial to have a basic understanding of the effects of atmospheric turbulences on ground-based observation in the optical and near-infrared (NIR). Therefore, this chapter gives a short introduction on the effects of the atmosphere on astronomical observations and then focus especially on some simplifying assumptions such as Taylor's Frozen Flow Hypothesis (TFFH), which are important for the piston reconstruction concept. As the effect of atmospheric turbulences on astronomical observations is a very complex topic, this will only be a basic introduction. For more information see e.g. chapter 3 in Hardy (1998) or chapter 7 in Cassen et al. (2007)

2.1 THE ATMOSPHERE IN ASTRONOMICAL OBSERVATIONS

For astronomical observations with ground based telescopes, one has to deal with the effects of the earth's atmosphere. This means that one usually does not see a sharp image of an astronomical object, but rather several small bright spots, which are evolving rapidly. For a longer integration time (longer than a few milliseconds) this results in a smeared image of the objects with a typical diameter of around one arcsecond. An example of this effect can be seen in Figure 2.1. The full width at half maximum (FWHM) of the smeared out image from a point source is the so-called *seeing*, which size depends on the individual conditions. The seeing is a key parameter for the quality of an observational site, going down to excellent conditions with around 0.4 arcseconds seeing for example in the desert of Chile or on Hawaii.

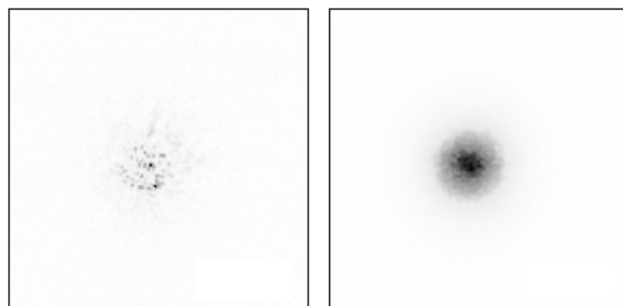


Figure 2.1: Image of a point source disturbed by the atmosphere, observed with a 1m ground-based telescope. Shown for a short exposure time of a few milliseconds (left) and for a long exposure (right). Source: <http://slittlefair.staff.shef.ac.uk/>

The reason for the smearing of the image is that the light wave from a distant object gets disturbed during its path through the atmosphere. This is due to the fact that the atmosphere is not homogeneous, but consists of small air parcels with slightly different temperatures and pressures. Changes in the temperature and pressure directly result in changes in the refractive index of air (see e.g. Cox and Pilachowski 2000):

$$n_{air}(P, T, \lambda) = 1 + 7.76 \cdot 10^{-5} \left(1 + 7.52 \cdot 10^{-3} \frac{1}{\lambda^2} \right) \frac{P}{T} \quad (2.1)$$

Due to turbulent movement in the atmosphere, the refractive index is constantly changing. Furthermore, the turbulence and wind motion depends on the height above the ground, as the turbulence scales with the air density which decreases exponentially with altitude. Therefore, it is usually strongest close to the surface. Due to this permanent change in the refractive index, some light rays from astronomical sources are bend differently than others. In terms of the wavefront, this means that a plane wavefront gets distorted during its path through the atmosphere as parts of it are more retarded in phase than others. This effect is only lightly dependent on the wavelength (at least in the optical and NIR regime), which means that it is more dominant for shorter wavelength, as the effects are larger in comparison to the wavelength.

2.2 TURBULENCE MODELS

In order to determine whether a flow is turbulent, one usually uses typical velocity v_0 and length scale L_0 of the flow and the viscosity ν of the fluid to calculate the Reynolds number: $Re = v_0 L_0 / \nu$. As the viscosity of air is $\nu \approx 1.5 \times 10^{-5} \text{ m}^2 \text{ s}^{-1}$ and the typical scales in the atmosphere are lengths on the order of tens of meters and velocities around 10 m s^{-1} , one gets a typical Reynolds number for atmospheric flows of around $Re \approx 1 \times 10^7$, which corresponds to a fully turbulent flow (Roddier 1981). Therefore, in order to give some predictions for the movement of the air in the atmosphere, it is necessary to use a turbulence model.

The most common turbulence model was introduced by Andrey Kolmogorov (Tatarskii 1961). The main idea of the Kolmogorov model is that the turbulent energy is added on a large scales (in case of the atmosphere, mostly due to solar heating), with large turbulence eddies dissipating into smaller ones. The energy is propagating from the large to the smaller eddies, until it eventually dissipates into heat. The scale for such a progress is given by two scale sizes, the outer scale L_0 (size of the largest eddies) and the inner scale l_0 (size of the smallest eddies).

The effects of the turbulences on the phase of the incoming wavefront Φ are described with a structure function $D_\Phi(r)$ (Tatarskii 1961):

$$D_\phi(r) = \left\langle |\Phi(r') - \Phi(r' + r)|^2 \right\rangle_{r'} \quad (2.2)$$

The structure function gives the intensities of the introduced phase fluctuations on scales of the size r . For the Kolmogorov turbulence one finds the following structure function (see e.g. Hardy 1998; Cassen et al. 2007):

$$D_\phi(r) = 2.91 \left(\frac{2\pi}{\lambda} \right)^2 r^{5/3} \sec \zeta \int dh C_N^2(h) \quad (2.3)$$

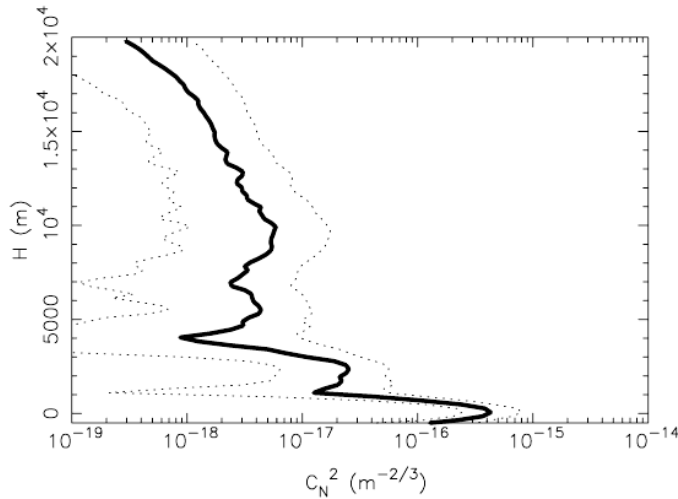


Figure 2.2: Example of a typical $C_N^2(h)$ profile, measured at the LBT in Arizona, by Masciadri et al. (2010).

This equation gives the phase fluctuations due to Kolmogorov turbulences from the whole atmosphere for an observation with the zenith angle ζ . The parameter $C_N^2(h)$ is the structure parameter for refractive index variations and gives basically the strength of the variation of the refractive index or the turbulence strength. $C_N^2(h)$ strongly depends on the height above the ground, as one usually finds a layer of very strong turbulence close to the surface and another strong layer at approximately 10 km above the ground, where strong winds are present. The vertical distribution of turbulence and the assumption of different layers is described in more detail in section 2.3, but for now an example of a $C_N^2(h)$ profile from the LBT can be seen in Figure 2.2.

Another very common way to describe the statistics of the turbulence is the power spectral density (PSD). This describes the distribution of power in different frequencies, or in this case, how much each spatial frequency $k = 2\pi/l$ contributes to the total wavefront distortion. The PSD in the Kolmogorov theory is given by:

$$\Phi(k) = 0.0365 C_N^2 k^{-5/3} \quad (2.4)$$

For a derivation of this equation see e.g. Cassen et al. (2007, p. 132). The power spectrum of the form $\Phi(k) \propto k^{-5/3}$ is typical for the Kolmogorov turbulence and is often used to verify the model (Figure 2.3). For a derivation in three dimensions one finds a similar power law with $\Phi(|\vec{k}|) \propto |\vec{k}|^{-11/3}$ (Noll 1976; Hardy 1998).

The power-law dependence in Equation 2.4 shows that the wavefront has a fractal structure. This means that the large scale perturbations from the atmosphere look like scaled up versions of smaller scale perturbations. From this one can also conclude, as directly visible from the power spectrum, that most of the power lies in the large scale perturbations.

However, the mentioned structure function and power law (Equation 2.3 and Equation 2.4) can only be used when the turbulence can be described by the Kolmogorov theory. This is the case between the outer scale L_0 and the inner scale l_0 . There is no constant value for the outer scale, but one usually expects values around few tens of meters (see e.g. Buscher et al.

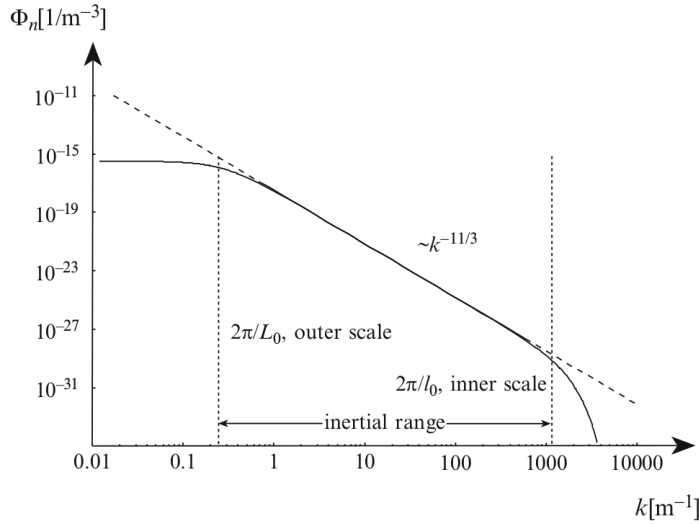


Figure 2.3: Comparison of a Kolmogorov spectrum (dotted line) and a van Karman spectrum (solid line). The outer scale is set to $L_0=22\text{m}$ and the inner scale to $l_0=5\text{mm}$. Adapted from Glindemann (2011).

1995; Conan et al. 2000; Conan et al. 2002). The lower scale is usually at values lower than 10 millimeters (Peters et al. 2008), which is so small that one usually can neglect the effects of the lower scale in astronomical aspects. As I am aiming for telescopes with a diameter of 8 meter, the outer scale is also not of great importance for this study, but will eventually become a very important parameter when dealing with the new class of Extremely Large Telescopes (ELTs) with a mirror diameter of 30 m or larger.

For scales larger than the outer scale, it is usually expected that the spectrum saturates, as the turbulence is uncorrelated in this regime. To describe this behavior, one uses a modification of the Kolmogorov spectrum, the von Karman spectrum (Buscher et al. 1995):

$$\Phi(|\vec{k}|) \propto (\kappa^2 + L_0^{-2})^{-11/6} \quad (2.5)$$

An example of such a spectrum is shown in Figure 2.3, which also includes the lower scale l_0 . The lower scale is neglected in Equation 2.5, as it has no importance for astronomical observations.

FRIED PARAMETER

A simple validation of the intensity of atmospheric turbulence is the Fried parameter r_0 , first introduced by Fried (1965). The Fried parameter is defined as the diameter of a circle within which the variance of the wavefront aberration, due to the passage of light through the atmosphere, is equal to 1 rad^2 (Noll 1976). Its complete mathematical definition is given by:

$$r_0 = \left[0.423 \left(\frac{2\pi}{\lambda} \right)^2 \sec \zeta \int dh C_N^2(h) \right]^{-3/5} \quad (2.6)$$

	Wavelength	Conditions		
		Very good	Medium	Bad
Seeing ["]	0.5 μm	0.45	0.85	1.2
r_0 [cm]	0.5 μm	23	12	9
	2.2 μm	136	72	51
D/r_0 []	0.5 μm	35	66	93
	2.2 μm	6	11	16

Table 2.1: Example values for seeing and the fried parameter. The conditions (good/medium/bad) are with respect to an excellent observing site, such as the VLTI.

This then reduces the phase structure function (Equation 2.3) to the following equation, which only depends on the Fried parameter:

$$D_\phi(r) = 6.88 \left(\frac{r}{r_0} \right)^{5/3} \quad (2.7)$$

Furthermore, the quotient of telescope diameter D and Fried parameter D/r_0 is often used as an indication of how strong the atmospheric disturbance of the wavefront is. If $D/r_0 < 1$ the observation is diffraction limited and the resolution of the telescope is given by the usual Rayleigh criterion:

$$\Theta \approx 1.22 \frac{\lambda}{D} \quad (2.8)$$

However, if $D/r_0 > 1$ the resolution is not limited by the telescope size, but by the atmospheric turbulence. In the so called seeing limited case one gets a resolution of:

$$\Theta \propto \frac{\lambda}{r_0} \quad (2.9)$$

In this case a larger size of the telescope does not improve the resolution, as it is limited by the atmosphere. This is the usual case for modern telescopes, as typical values for r_0 at good seeing are usually around 10 to 20 cm. Therefore one has to use adaptive optics systems to get a resolution in the diffraction limited area. This is discussed in more detail in chapter 3.

As one can directly see from Equation 2.6, the Fried parameter depends on the wavelength as $r_0 \propto \lambda^{6/5}$. Due to this wavefront dependency, the values for r_0 in this work are, if not stated otherwise, always given at 0.5 μm. The Fried parameter increases with larger wavelength and it is easier to get diffraction limited telescope performance at larger wavelength. The same applies for the case of the piston reconstruction mechanisms that are addressed in this work: the effects of the atmosphere will be smaller at larger wavelength. In order to take this into account I will study two wavefront regimes: the V-Band in the optical (0.5 μm) and the K-Band in the NIR (2.2 μm). Typical values of the Fried parameter in these two cases for different seeing conditions are shown in Table 2.1.

2.3 TAYLOR'S FROZEN FLOW HYPOTHESIS

The atmosphere is as a large highly turbulent medium very complex and difficult to model. Therefore one tries to find approximations, in order to reduce the complexity. One of the most popular approximations and an essential assumption for this work is Taylor's Frozen Flow Hypothesis (TFFH) introduced by Taylor (1938). The frozen flow hypothesis states that one can describe the complete atmosphere as a composition of several different layers. Each of these layers of atmosphere stays spatially stable on short time scales and is only moved by the wind velocity. This results in a translation of the phase aberration across the telescope pupil. Each of these layers can be described by the Kolmogorov turbulence model and the total measured turbulence is the superposition of all these layers. TFFH introduces a measurement for the temporal behavior of the atmosphere with the time constant τ_0 :

$$\tau_0 = \frac{r_0}{v} \quad (2.10)$$

with the wind velocity v . For typical wind velocities of 10 m s^{-1} and a r_0 of 20 cm , this equation gives typical values for τ_0 of 20 ms . As for r_0 this is the time by which the wavefront aberration is equal to 1 rad^2 and τ_0 has the same wavefront dependency as r_0 : $\tau_0 \propto \lambda^{6/5}$.

The importance of TFFH for this work is based on two different points: Firstly, AO simulations such as Yorick Adaptive Optics simulation (YAO) are usually using TFFH to compute the atmospheric effects (see chapter 6) and secondly, the whole concept that is discussed here is based on the assumption that TFFH is valid for a short timescale (see chapter 5). Therefore, the validity of TFFH is very important for this work.

In the following, I separately look at the two central assumptions of the frozen flow hypothesis (multilayer and translation by wind) and highlight the according research of the recent years, in order to get an overview of the adequacy of TFFH.

MULTILAYER ATMOSPHERE

By looking at typical atmosphere profiles (such as Figure 2.2), one can see that there are direct hints to an atmosphere composition with different layers. The usual assumption is that there is one very dominant ground layer, which contains a high fraction of the atmosphere. The turbulence strength in the different layers of the turbulence has been studied from various authors for the most important telescope sites around the world. Most of the results are more or less consistent with each other, with some variance due to the different atmospheric conditions around the world.

The main conclusion from the atmosphere studies is that the atmosphere can be divided into three general layers: the ground layer, directly above the ground with a height of around 1.5 km , one layer above (the medium layer) until a height of approximately 5 km , and then the troposphere or high layer from 5 to 16 km (see e.g. Andersen et al. 2006; Avila et al. 2004). This classification comes naturally, when one looks at a turbulence profile as the one in Figure 2.2, as there are three dominant peaks for these three layers. The main characteristics of these three layers are that the ground layer is the most dominant one. Depending on the site and the atmospheric conditions, the ground layer is expected to

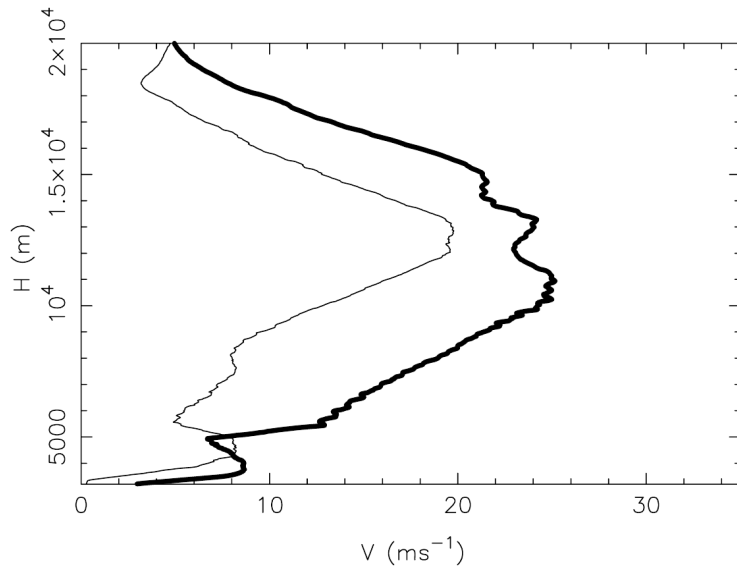


Figure 2.4: Example for a wind speed profile, measured at the LBT in Arizona, by Masciadri et al. (2010). The bold line is from measurements in winter and the thin line from measurements in summer.

contribute between 50 and 70 percent to the total turbulence. This has been shown for the LBT (Egner et al. 2006; Masciadri et al. 2010) and for the Gemini-South telescope (Tokovinin and Travouillon 2006) and is also the usual approach for simulating the atmosphere above the VLTI (Clénet et al. 2010). The ground layer usually has wind speeds around 10 km s^{-1} .

The medium layer is less prominent with around 20 % of the turbulence and slightly lower wind speeds of around 5 to 10 km s^{-1} . The remaining turbulence lies in the high layer where very high wind speeds can be present with values well higher than 20 km s^{-1} (Avila et al. 2004; Egner et al. 2006). A typical wind speed distribution from the LBT is shown in Figure 2.4. There is still atmospheric turbulence above this layer, but the importance is so small that it can usually be neglected.

While there are plenty of studies of the wind speed in the different layers, there is only few information about the actual wind direction. The actual direction of the movement is usually not of great importance. However, for this study it is quite crucial to know if the different layers are moving into a similar direction or if there is random contribution. From the few available studies, the most important one was done by Avila et al. (2006) at the San Pedro Martir in Mexico. They found that in general the wind direction varies very little with the altitude. In a few nights of their observations, there was a large variation of wind direction above 10 km , but in general the wind direction stayed within approximately 60 degrees and showed no systematic behavior with increasing altitude. These findings agree with older results from Schöck and Spillar (1998) and Gentry et al. (2000).

The three layer system works well to understand the ongoings in the atmosphere, but is not sufficient as input for atmospheric simulations. Therefore, one usually splits up the three main layers into several different layers to better simulate the complexity of the atmosphere. For this work I built up a multilayer atmosphere which agrees to all the findings above and

Layer	#	Altitude [m]	Fraction [%]	Wind speed [ms ⁻¹]	Wind direction [°]
Ground	1	0	45	10	0
	2	400	13	12	5
	3	1000	11	10	-5
Medium	4	1800	9	8	-10
	5	2500	6	6	-15
	6	5000	5	10	-5
High	7	8000	4	20	15
	8	11000	4	25	25
	9	15000	3	15	30

Table 2.2: Composition of a simulated multilayer atmosphere as it is used throughout this work.

in which I tried to combine the results from the LBT (Masciadri et al. 2010) and the usual approach for the VLT (Clénet et al. 2010). The parameters of this atmosphere are shown in Table 2.2 and if not stated differently, this is the atmosphere used in the later simulations.

WIND TRANSLATION

The second part of TFFH states that the atmosphere layers stay temporally stable and are moved by the wind. This has been subject to great debate. There have been different studies in order to verify the frozen flow theory and identify the amount of random fluctuations in the atmosphere. These random fluctuations are called boiling and are the second important aspect in the temporal evolution of the atmosphere, next to the translation due to wind. The problematics of boiling are discussed in the section below.

The most common approach to test the importance of frozen flow is to use cross correlation and deconvolution techniques on the data from one or several wavefront sensors (WFSs) (Schöck and Spillar 2000; Guesalaga et al. 2014, see e.g.). With the cross correlation, one is able to detect the motion of layers as a moving peak in the cross correlation image (see Figure 2.6). With a further deconvolution of the cross correlation, with the auto correlation of the first image, one can then calculate the fraction of frozen flow driven turbulence. This leads to a peak in the deconvolution image, whose intensity stays temporally constant at a value of one, when TFFH is the only source of temporal evolution. If other effects, such as boiling, play a role, the intensity of the deconvolution peak decreases. The results of this cross correlation and deconvolution by Schöck and Spillar (2000) are shown in Figure 2.5. From this Figure one can directly see that TFFH accounts for 80 % of the temporal development for about 20 ms. Schöck and Spillar (2000) conclude that accurate wavefront predictions are possible for time scales in the order of 10 ms and that the accuracy slowly decreases for longer timescales. Guesalaga et al. (2014) came to similar results with the same technique, adding that the decay rate of the frozen flow correlation increases linearly with increasing wind velocities.

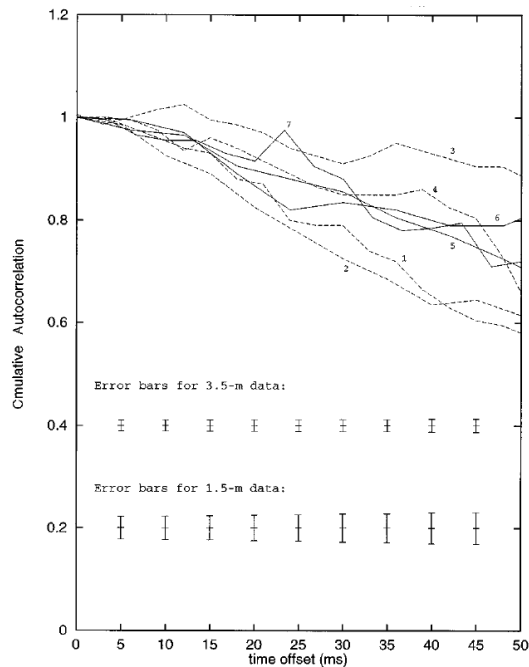


Figure 2.5: Evolution of the maximum value of the deconvolution peak with time for different measurements from Schöck and Spillar (2000).

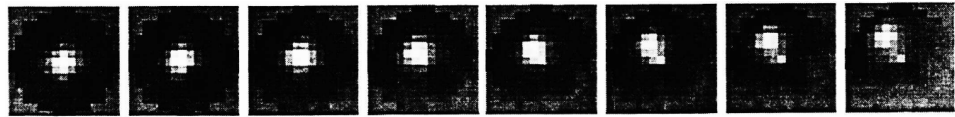


Figure 2.6: Cross correlation with increasing time difference, showing a translation of the atmosphere. From Saint-Jacques (1998).

A similar study was done by Saint-Jacques (1998) and Saint-Jacques and Baldwin (2000) with focus on the coherence time of the atmosphere. Similar to Schöck and Spillar (2000), they found out that the coherence peak decreases with time and reaches values as low as 30 % of its initial value after 100 ms. This is slightly worse than the previously mentioned results, but the range is similar. Saint-Jacques and Baldwin (2000) further pointed out that for the temporal evolution of the turbulence, boiling plays an important role. This is especially the case for longer timescales, which also fits to the previous results.

A different approach was taken by Gendron and Léna (1996), Poyneer et al. (2009), and Cortés et al. (2013) by using a Fourier analysis of the WFS slope measurements. With this method one can determine the temporal structure of the turbulence in the power spectrum of the measurement. In general their results agree with the previous studies, but Poyneer et al. (2009) also investigated the stability of the velocity vector for each layer. They found to much longer timescales of several minutes or even hours for the deconvolution peak of single layer. This shows that TFFH is valid over longer timescales for individual layers, but

only for short timescales for the whole atmosphere. It also agrees with findings by Avila et al. (2006) that the wind profiles stay comparably stable over whole nights.

In conclusion, basically all performed studies came to the result that TFFH is valid over small timescales (Bharmal 2015), with slightly varying values for this timescale. From these studies, I conclude that TFFH is reasonably good as a first approach as long as we work on timescales below 20 ms.

BOILING

Taylor's Frozen Flow Hypothesis (TFFH) is the usual approach for describing the temporal evolution of turbulence in the atmosphere. However, as mentioned before, a large fraction of the temporal evolution is not caused by frozen flow, but by a random change in the atmosphere. This effect is normally referred to as boiling. A full derivation of the effects from boiling can be found in Saint-Jacques (1998). For the purpose of this work it is sufficient to know that boiling is a chaotic dynamical evolution due to the turbulence in the atmosphere. Inside a fully turbulent medium all sizes of eddies are present and the energy is dissipated, which changes the spatial configuration over time.

The visible turbulence for an observer is then the superposition of the translation of the different layers and the boiling in each of the layers. There have been different studies concerning the boiling, for example Berdja and Borgnino (2007) did research on modeling a turbulent atmosphere by including boiling. Also, Assémat et al. (2006) developed a technique to build phase screens with included effects due to boiling. However, to really get a realistic atmosphere which includes the effects of boiling is not easily possible, as the actual strength and the power spectrum of boiling are not very clear. Furthermore, the intensity of boiling can change strongly, depending on the actual site and conditions. This problem increases as the boiling is not the same for all layers, as there is for example additional dome boiling induced by the warm telescope environment into the ground layer. There is also the problem that adaptive optics simulations, such as YAO, take several atmospheric layers as input and use TFFH to create the complete atmospheric disturbance.

One could, in principle, try to build phase screens with boiling effects. However, the results would always be very dependent on the input parameters of the phase screens. Therefore, I decided to take a different approach. In the second part of this work (chapter 7 - 9) I completely neglect boiling and assume a perfect frozen flow for the simulations, knowing that the results will be less and less realistic for timescale significantly longer than a few 100 ms. Nevertheless such simulation show realistic short term behavior, and qualify to specify the general system requirements to implement P-REx, such as for example the averaging timescales or the WFS sampling. In the final part (chapter 10 - 11) I transfer the previous findings onto real atmospheric data from the LBT, which then of course include all atmospheric effects and can give a hint onto the validity of my simulation results for real data.

ADAPTIVE OPTICS

3

In optical ground-based observations, one uses adaptive optics in order to overcome the effects of the atmosphere and to reach the diffraction limit of the telescope. Therefore, at large optical interferometers, each individual telescope is usually equipped with an adaptive optics system. Additionally, the piston reconstruction system uses the data from adaptive optics systems for determining the relevant parameters of the atmosphere. In order to get an understanding for such data, this chapter explains the main principles of adaptive optics and presents the most common types of adaptive optics systems. For a more complete overview of adaptive optics in astronomy see e.g. Hardy (1998), Davies and Kasper (2012), and Tyson (2015).

3.1 BASICS OF ADAPTIVE OPTICS

In section 2.1, the effects of the atmosphere for astronomical observations in the optical and NIR are presented. As mentioned the main point is that the atmosphere is responsible for a blurring of the image. This can be avoided by very short integration times (which is usually not helpful), or by the use of adaptive optics (AO) systems.

The idea of AO in simple words is to detect the disturbance in the incoming light, which is introduced by the atmosphere, and correct it. The basic principle for the most simple and also most common AO system is shown in Figure 3.1: The incoming wavefront is not flat, but perturbed by the atmosphere. A wavefront sensor (WFS) is used to measure the perturbation of the wavefront. From this measurement one calculates an appropriate correction and applies this correction to the deformable mirror (DM). This feedback loop has to be very fast, in order to keep up with the temporal perturbations of the atmosphere and is usually carried out several hundred times per second. In order to get a good measurement for the WFS, it does not observe the science object, but a separate guide star which should be comparably bright and pointlike.

The described system with one WFS, one DM, and a natural guide star (NGS) is the simplest version of an AO system and is called single-conjugated adaptive optics (SCAO). Despite its simplicity it is still widely used in modern telescopes. In order to improve the performance of the AO system one now tries to work with more complex systems. This includes one or multiple artificial laser guide star (LGS), multiple WFSs and DMs, or a correction for a certain layer of the atmosphere (e.g. ground-layer AO systems or multilayer systems, see section 3.4).

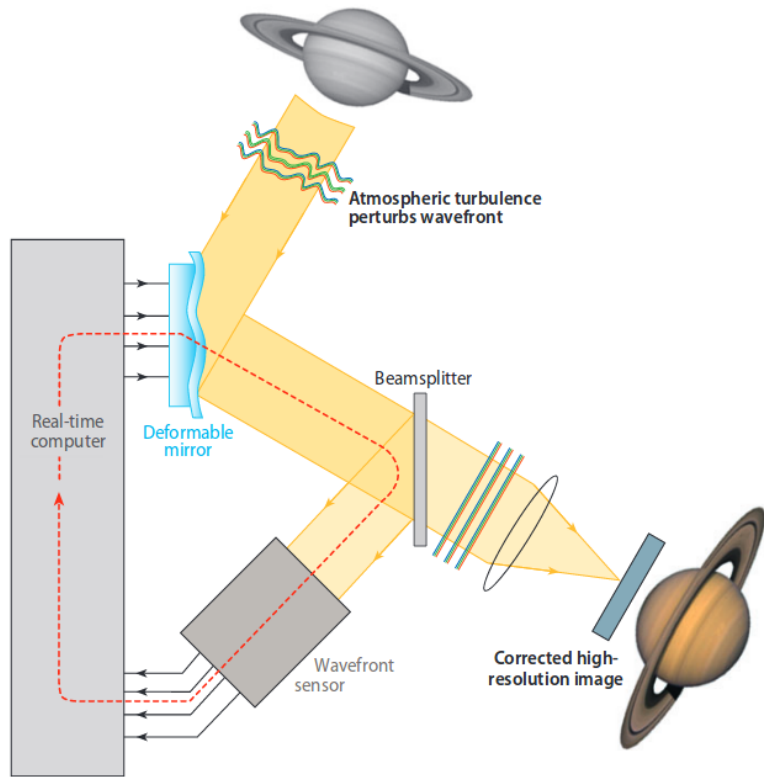


Figure 3.1: Sketch of a simple AO system, from Davies and Kasper (2012)

3.2 WAVEFRONT SENSOR

One of the key components of an AO system is the wavefront sensor (WFS) which measures the distortion of the incoming wavefront. In astronomy this is a slightly more complicated task than in usual optics, as the incoming light is incoherent. Additionally, the detectors of WFS have to be very efficient and fast in order to work in a high frequency loop on faint guide stars. There are several approaches for such a sensor and in the following I will present the three most common types of WFS. The different wavefront sensors have different advantages concerning, for example, noise and sensitivity, which was particularly investigated by Guyon (2005). There are also other sensors which are rarely used, but I focus here and also in my later simulations on the three most common types.

SHACK-HARTMANN SENSOR

The Shack-Hartmann wavefront sensor (SH WFS) is the most widespread WFS, as it follows a comparably simple concept: The image of the pupil is projected onto an array of equal lenses. The detector of the SH WFS lies in the focal plane of these lenses and measures an array of individual spots from each lenslet. For a plane wave each of these spots is exactly

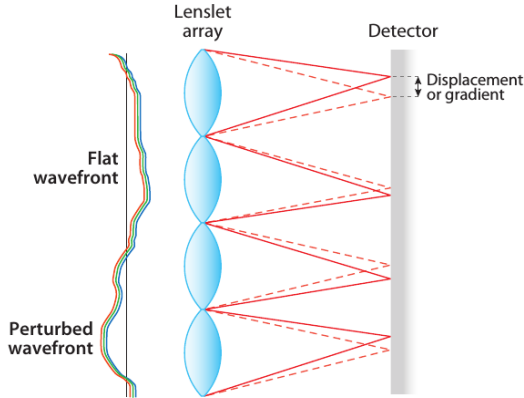


Figure 3.2: Principle of a Shack-Hartmann wavefront sensor (SH WFS), showed here for four lenslets of a larger array (from Davies and Kasper (2012)).

in the optical axis of its lenslet. When the incoming wavefront is distorted, the spots are displaced from their original positions (see Figure 3.2). These displacements into the x and y direction are orthogonal to the average of the local wavefront slopes in x and y direction over one lenslet. A SH WFS therefore directly measures the gradient of the wavefront over individual subapertures. From this measurements one can reconstruct the original wavefront up to a constant factor, which is usually not important for imaging.

PYRAMID SENSOR

The pyramid WFS (Ragazzoni 1996) consists of a transparent pyramidal prism which is placed into the focal plane so that the light is split up into four individual images (Figure 3.3). The pyramid is then modulated either by physically moving the pyramid itself, or by dynamically controlling the incoming beam (for example with a tip-tilt mirror). From the difference in intensity distribution in the different images, integrated over several modulation circles, one can directly measure the wavefront slopes in the pupil (Esposito and Riccardi 2001). The measurement of the pyramid sensor is therefore the same as for a Shack-Hartmann sensor. However, the pyramid sensor has the advantage that one can adapt the sensitivity by changing the modulation frequency or the binning on the detector. This comes at the cost of moving parts, which reduces the robustness of the sensor, and the fact that nonlinearities can occur for large wavefront aberrations or for large modulation amplitudes (Akondi et al. 2013).

CURVATURE SENSOR

The curvature sensor first introduced by Roddier and Roddier (1988) does not measure the gradient of the wavefront, but the second derivative, the so called curvature. In order to do so, a curvature sensor has two detector arrays, one slightly before and one slightly

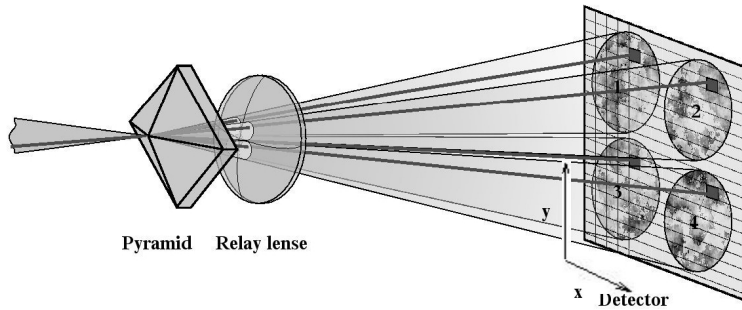


Figure 3.3: Principle of a Pyramid WFS, which shows how the incoming light hits the pyramidal prism and is then visible as four images on the detector (from <http://inspirehep.net>).

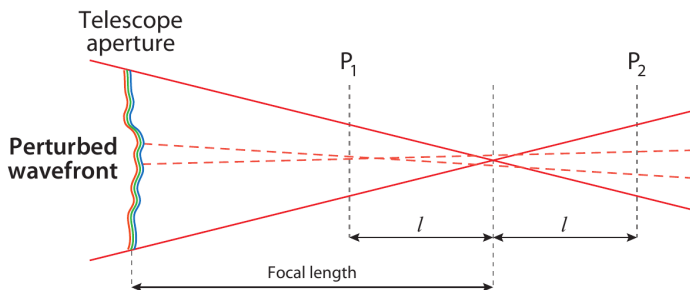


Figure 3.4: Principle of a curvature WFS, with the perturbed wavefront reaching the two detectors at P_1 and P_2 . The distance of the detectors from the focal plane is given by l . This figure is adapted from Davies and Kasper (2012).

after the focal plane. A local wavefront curvature causes differences in the intensity of the detector, as the light is focused slightly more onto the detector in front of the focus (positive curvature) or on the one behind the focus (negative curvature), as shown in Figure 3.4. The curvature is then proportional to the difference in intensity:

$$C \propto \frac{I_1 - I_2}{I_1 + I_2} \quad (3.1)$$

The curvature sensor is also a comparably simple concept and has major advantages if it is coupled with a bimorph DM. One downside, however, is that there is no possibility to measure the tip and tilt of the wavefront, which means that an additional sensor is needed to compensate for this.

3.3 DEFORMABLE MIRROR

The deformable mirror (DM) is the main element for correcting the aberrations introduced by the atmosphere. The usual approach for a DM is an array of actuators, which are connected to a thin optical surface. Under expansion of the actuators, the surface deforms and can be adapted to the measured wavefront aberration. The requirements of a DM are very specific for the actual system, as for example the number of actuators and their available stroke directly scale with the diameter of the telescope: a larger telescope needs more actuators, which can compensate a larger perturbation. Other key parameters of the DM are the spacing of the actuators and the response time, which have to be adapted to the corresponding τ_0 and r_0 at the telescope site. The actual requirements of the DM also depend on the used AO system (for example SCAO or multi-conjugated adaptive optics (MCAO)). As the analysis of this work is mainly done with data from the WFS, a further insight into DM technologies is not of importance for this study. An overview of the different techniques can be found in Davies and Kasper (2012) or Tyson (2015, chapter 6), and the necessary requirements for DMs in Madec (2012).

WAVEFRONT RECONSTRUCTION

In an AO system, the signal from the WFS has to be converted into voltages for each individual DM actuator. This conversion is shown in Figure 3.1 as a simple gray box. There are several possibilities for the conversion from the WFS signal to DM voltages. The probably most intuitive way would be to reconstruct the original phasefront from the WFS signal and then apply this model with reduced spacing and a gain factor to the DM. However, as the wavefront reconstruction is computational expensive and the correction has to run in real time at high frequencies, this is usually not done.

The more common way is to create a control matrix (CM) which directly translates the WFS measurement into DM voltages. This is done by first measuring an interaction matrix (IM) (or also called poke matrix (Tyson 2015)). The IM is recorded by moving every single DM actuator by a certain voltage α and measuring the response of the WFS \vec{b}_i . This is usually not done by a single measurement, but by averaging over several measurements with positive and negative movements of each actuator. By doing this for each of the n actuators the IM can then be constructed by just writing the measured vectors in an array:

$$\text{IM} = \left[\frac{\vec{b}_1}{\alpha} \frac{\vec{b}_2}{\alpha} \dots \frac{\vec{b}_n}{\alpha} \right] \quad (3.2)$$

This matrix translates the DM voltage into WFS measurements and it is used in later parts of this work for this purpose. However, for an AO system one needs the opposite response from WFS slopes to DM voltages. This is represented by the CM, which is the inverse of the IM. The inverse of the IM can usually not be directly calculated, as the matrix is nonsquare. Therefore, one has to use methods like a Gaussian reconstructor, or the least square method to calculate the actual CM. With this matrix one can then convert the WFS measurement S into DM voltages V :

$$\vec{V} = \text{CM} \cdot \vec{S} \quad (3.3)$$

Of course the measurement of the IM is in reality more complex as one has to account for noise sources and eventually a more complex AO system. However, the basic principle stays the same. For a more general overview of this topic see Tyson (2015, chapter 7).

3.4 COMPLEX AO SYSTEMS

Apart from the simple SCAO system described earlier, there are several other possible designs for an AO system. From these designs, I shortly want to present the two most common ones, which are also used for later simulations. Both of these systems are layer conjugated AO systems, which means that they are capable of detecting turbulence from one or more distinct atmospheric layers. Such a layer conjugated system could be used to build up a layer oriented P-REx algorithm, which would potentially increase the general performance of the piston drift reconstruction as TFFH is valid over much longer timescales for a single layer than for the whole atmosphere (see Poyneer et al. 2009).

GROUND LAYER ADAPTIVE OPTICS

The principle of a ground layer adaptive optics (GLAO) system is shown in the left image of Figure 3.5. The system consists of only one DM, but several WFSs, which are sensing different guide stars distributed over the field of view. Such a system is designed to only correct the contributions of the ground layer turbulence. This is achieved by observing guide stars over a comparably large field of view and by averaging the signal of all used WFSs. This average is then used as an input for the DM. The idea behind this is that all WFSs measure the same turbulence in the ground layer, but due to large separation of guide stars they get different signal from the higher turbulence layers. In the average of the signal, this high layer turbulences are only represented as noise and the signal from the ground layer dominates. The result of the GLAO system is usually not as good as for other AO systems. However, one gets a very large field of view which is uniformly corrected. While a usual SCAO system only has a corrected field of view of a few arc seconds, this can be up to several arc minutes for a GLAO system (Rabien et al. 2010). GLAO was first shown to work with MAD at the Very Large Telescope (VLT) (Marchetti et al. 2008), and an example for a currently used system is the ARGOS system at LBT (Rabien et al. 2010).

MULTI CONJUGATED ADAPTIVE OPTICS

A multi-conjugated adaptive optics (MCAO) system is similar to the previously discussed GLAO system, but it uses in addition to the multiple WFSs also two different DMs (see Figure 3.5 right). One of the DMs is used in the same way as in the GLAO system, in order to correct ground layer turbulence. This DM is therefore conjugated to the ground layer. The second DM is conjugated to the high layer, in order to correct for the turbulence from the upper atmospheric layers. In comparison to a SCAO system, this also gets a larger

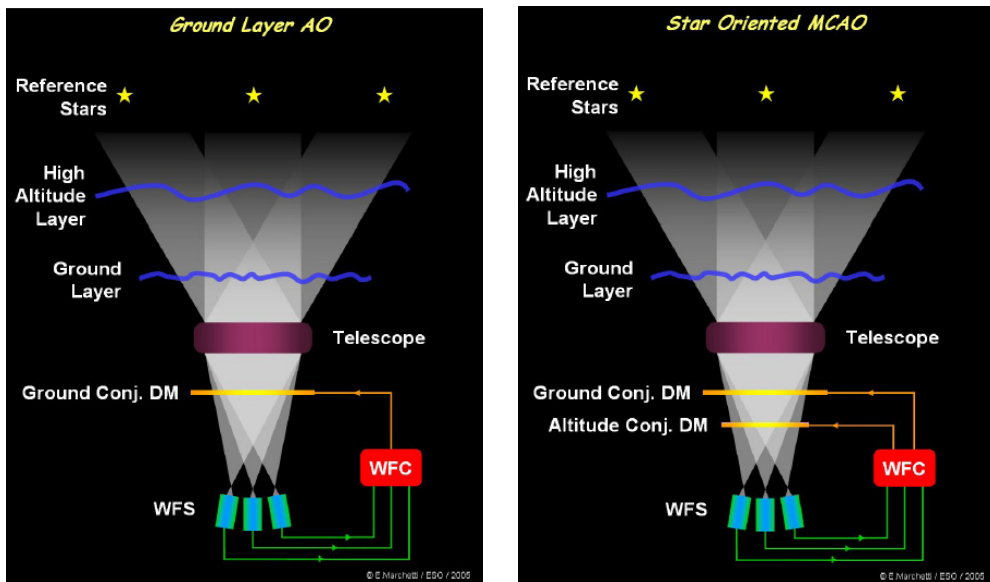


Figure 3.5: Schematic representation of a GLAO (left) and a MCAO system (right). Taken from https://www.eso.org/sci/facilities/develop/ao/ao_modes/.html.

corrected field of view. The corrected field is not as big as for a GLAO system, but the correction results are better.

MCAO was also first shown to work with MAD at the VLT and was then implemented at the Gemini South telescope (Rigaut et al. 2014). With LINC-NIRVANA there is also a MCAO system currently getting installed at the LBT (Herbst et al. 2012).

3.5 AO SYSTEMS AT LBT & VLTI

In order to get an understanding of the possible AO systems which are available for a piston reconstruction, Table 3.1 summarizes all systems that are usable at the VLTI and LBT and their most important parameters. As the piston drift reconstruction will either work with data from the WFS or data converted into WFS space, only the parameters of the WFS are of relevance here. More information on the systems can be found in the particular sources given in Table 3.1. This is not a full list of systems at the telescopes, especially at the VLT there are several other AO systems available (the ESO homepage offers a full list of systems¹). Only the listed systems are usable for the VLTI. For the VLTI, systems for both, the unit telescopes as well as for the smaller auxiliary telescopes², are included, as both can be used for interferometry. For the LBT, there is currently only one system available in the interferometric mode, the Large Binocular Telescope Interferometer (LBTI). This system employs a SCAO system called FLAO. LINC-NIRVANA instead will use as MCAO system

¹VLT AO systems <https://www.eso.org/sci/facilities/develop/ao/sys.html>, visited on 07.06.2017

²The VLTI Auxiliary Telescopes <https://www.eso.org/sci/facilities/paranal/telescopes/vlti/at.html>, visited on 07.06.2017

Telescope	D m	AO system	WFS-type	# WFS elements/D	λ_{AO} μm
VLT-UT ^a	8.2	MACAO ^c	Curvature	10	0.5
		CIAO ^d	SH	9	2.2
VLT-AT ^b	1.8	NAOMI ^e	SH	4	1.65
LBT	8.4	FLAO ^f	Pyramid	≤ 30	0.5

^a Unit Telescope (UT)^b Auxiliary Telescopes (AT)^c Arsenault et al. (2003)^d Kendrew et al. (2012)^e Gonté et al. (2016)^f Esposito et al. (2012)

Table 3.1: Basic properties of current AO systems at VLTI and LBT. The number of WFS elements per telescope diameter indicates the number of separate measurements along one diameter (e.g. number of lenslets for a SH WFS). For the pyramid sensor, the given number is the best possible value, as the binning can be changed to smaller values.

an optical combination of several pyramid sensors per corrected layer. LINC-NIRVANA can also be operated in SCAO mode, then similar to the FLAO system of the LBTI.

OPTICAL INTERFEROMETRY

4

In order to understand the utility of a piston reconstruction system, one has to be familiar with the problems that the atmosphere causes in optical and near-infrared (NIR) interferometry. Therefore, I give a short introduction of interferometry in general and then focus on the use of interferometry in the optical and its main complications. This will finally lead to the fringe tracker and the limits of current fringe tracking systems in section 4.3, which are of great importance for this work, as these are the limits I want to tackle with the piston reconstruction system.

Apart from that, it is not necessary for the scope of this work to get a deep understanding of all the aspects of optical interferometry. I will therefore only focus on the aspects which are important for the understanding of this work. For a more complete overview of (optical) interferometry see e.g. Monnier (2003), Glindemann (2011), and Buscher (2015)

4.1 BASIC THEORY

In classical ground based observations, the achievable resolution is limited by the diameter of the used telescope. Starting with the Michelson stellar interferometer in the early years of the 20th century, astronomers tried to combine the signal from several telescopes in order to work as one big telescope. Interferometry has been of great success in the last years, especially in radio astronomy. This led to the construction of the Atacama Large Millimeter Array (ALMA), which combines the signal of up to 73 telescopes. Besides the importance of atmospheric effects, the principle of interferometry is the same for all wavelengths. Therefore, I start this chapter by explaining the theoretical principle of interferometry in general, and then move on to the specific problem of interferometry in the optical and the NIR later. For a full introduction of radio interferometry see Rohlfs and Wilson (1996) and Haniff (2007).

DOUBLE-SLIT EXPERIMENT

The principle of interferometry is closely related to the double-slit experiment by Thomas Young from the year 1802: If coherent light from a point source passes two slits, an interference pattern will occur. This effect was originally used to prove the wave nature of light, as the interference pattern is due to two electromagnetic waves, propagating from the two slits and reaching the screen with different relative path lengths. These different

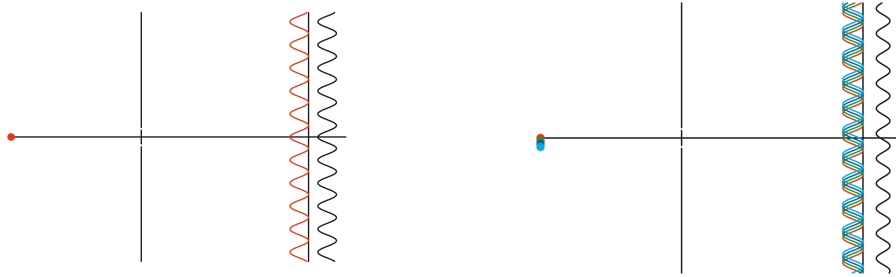


Figure 4.1: Interference pattern (colored) and visibility (black) for a double-slit experiment. The pattern is shown for a point source (left) and for an expanded source (right). Image from Jackson (2008).

path lengths then lead to constructive or destructive interference for the different positions along the screen. The intensity distribution for a single point source is given by:

$$I \propto (1 + \cos(k\alpha B)) \quad (4.1)$$

where α is the angle between the straight line from the two slits and the observed point at the screen. k is the wavenumber, and B the separation of the slits.

However, the exact shape of the interference pattern depends on the light source. A coherent point source, for example, produces a very sharp interference pattern with clear maximums and minimums. But if one expands the size of the source or uses an incoherent source, the interference pattern gets blurred, as shown in Figure 4.1. An important value in characterizing the pattern is the visibility V . It is defined with the highest and lowest intensity values in the interference pattern, I_{max} and I_{min} :

$$V = \frac{I_{max} - I_{min}}{I_{max} + I_{min}} \quad (4.2)$$

One finds that the intensity distribution of the source and the visibility as a function of the slit separation are correlated with a Fourier transformation. The so called Van Cittert-Zernike theorem relates the fringe contrast of an interferometer (or the double-slit experiment) to the Fourier transformation of the image brightness distribution. For a full derivation of this theorem see e.g. Glindemann (2011) or Thompson et al. (2017, pp. 767).

With two simple assumptions, the Van Cittert-Zernike theorem can be expressed in mathematical terms. Firstly one needs quasi monochromatic light, which means that the bandwidth of the incoming light has to be much smaller than its frequency ($\Delta\nu \ll \nu$). Secondly, the target emits light only on a very small region on the sky such that the spherical coordinates $(\vec{\Omega} + \delta\vec{\Omega})$ can be interpreted as Cartesian coordinates $(\vec{x}' + \delta\vec{x}')$. Both assumptions are usually true for astronomical observations. One can then write the interferometer response of a source in the source plane Σ as the frequency dependent complex visibility $V(\vec{x})$, given by the Fourier transformation of the brightness distribution $I_\nu(\vec{x}')$. Vectors in the plane of observation are unprimed ($\vec{x} = (x, y)$), while vectors in the source plane are primed

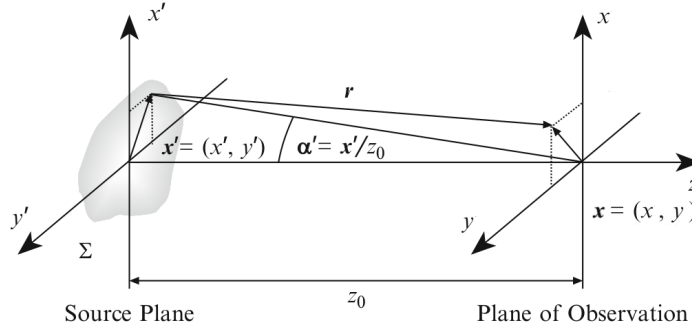


Figure 4.2: Geometry of light propagation for the Van Cittert-Zernike theorem

(($\vec{x}' = (x', y')$). For the nomenclature see Figure 4.2. The theorem is then given by the following equation:

$$|V(\vec{x})|e^{-i\phi_V} = \frac{\int \int dx' dy' I_\nu(\vec{x}') e^{-ik\vec{x} \cdot \vec{x}'}}{\int \int dx' dy' I_\nu(\vec{x}')} \quad (4.3)$$

While \vec{x}' gives the position of the source, \vec{x} is the baseline vector between two telescopes (or the two slits) projected on the plane of the source. In astronomical interferometry, this vector is usually given in units of the wavelength and called the (u,v) vector. This means that it is possible to reproduce the structure and brightness of the source by looking at the interference pattern. In more detail, one uses the Fourier transformation of the visibility to recreate the brightness distribution of the source.

TWO TELESCOPE INTERFEROMETER

So far the motivation for interferometry and its possibilities have been very theoretical. Therefore, I want to use this section to adapt the ideas to a two telescope interferometer and motivate the result from Equation 4.3.

The idea of the two slit experiment can be transformed into a two element interferometer as shown in Figure 4.3. The two slits are replaced by two telescopes and instead of using a screen, the two signals are combined electronically. When an electromagnetic wave reaches the interferometer, the first antenna gets the signal $Ee^{i\omega t}$. As the signal reaches the second antenna with a phase delay due to the optical path difference (OPD), the signal is then $Ee^{i\omega t} e^{ik\vec{B} \cdot \vec{s}}$. The signals are then put together with the help of a correlator. $Ee^{i\omega t}$ is just a plane wavefront, which is assumed to be constant over the observation time for a certain point \vec{x}' of the observed source. This means that the correlated signal at the interferometer gives the response $R = I(\vec{x}') e^{ik\vec{B} \cdot \vec{s}}$ with $I(\vec{x}')$ the source intensity at a certain point \vec{x}' . To get the response of the total source, one has to integrate over the whole source.

$$R = \int d\vec{x}' I(\vec{x}') \exp [ik\vec{B} \cdot (\vec{s} + \vec{x}')] = \exp [ik\vec{B} \cdot \vec{s}] \int d\vec{x}' I(\vec{x}') \exp [ik\vec{B} \cdot \vec{x}'] \quad (4.4)$$

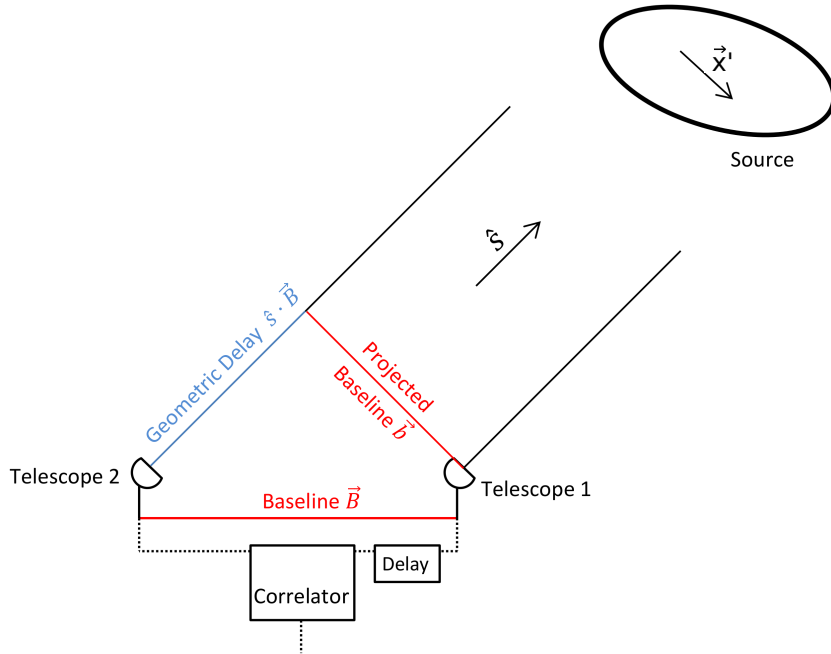


Figure 4.3: Schematic presentation of an interferometer with two telescopes observing a source \vec{x}' .

Here, I use the projected baseline vector \vec{b} to be parallel with \vec{x}' and therefore $\vec{B} \cdot \vec{x}' = \vec{b} \cdot \vec{x}'$ holds. The prefactor of the integral is the phase delay due to the path difference, which can be removed with the help of an electronic delay. The integral is then the visibility function of the intensity distribution $I(\vec{x}')$:

$$V(\vec{b}) = \int d\vec{x}' I(\vec{x}') \exp [ik\vec{b} \cdot \vec{x}'] \quad (4.5)$$

The last step is then to transform the coordinates in Equation 4.5 into the uv-plane. This plane is the one which contains the projected baseline vector \vec{b} . The uv-plane can be imagined as the plane of observation as seen from a fixed point in the source plane. The major advantage is then, that with the rotation of the earth, the plane stays fixed. But for every measurement the projected baseline is at a slightly different place in the plane, as it rotates with the earth. That means that the rotation of the earth automatically allows different measurements in the uv-plane.

For the transformation of the coordinates, it is important that $I(\vec{x}')$ lies in the sky plane Σ . In this coordinate system \vec{b} is defined as: $\vec{b} = \frac{2\pi}{k}(ux' + vy')$. The prefactor is necessary, as u and v are measured in units of wavelengths. This then leads to the following conclusion:

$$\vec{b} \cdot \vec{x}' = \frac{2\pi}{k}(ux' + vy') \Rightarrow V(u, v) = \int \int dx' dy' I(\vec{x}') \exp [i2\pi(ux' + vy')] \quad (4.6)$$

Except for the correct normalization, this equation is equal to the result from Equation 4.3, with the baseline vector now given in the uv-plane.

It follows that the visibility function is a two-dimensional Fourier transformation of the position in the sky, weighted with the intensity at this position. This shows the principle of interferometry in a more direct way: One measures the visibility and uses the inverse Fourier transformation to get the image of the sky, the so called sky brightness distribution (Haniff 2007). However, this is still simplified as a two element interferometer is usually not sufficient and other aspects, such as a finite bandwidth and aberrations, have been neglected. But the main properties remain the same and can also be used for a telescope array by measuring each possible baseline simultaneously.

ADVANTAGES AND DISADVANTAGES OF INTERFEROMETRY

The main advantage of interferometry clearly is the better angular resolution. For a single telescope, the resolution is defined with:

$$\Theta \approx 1.22 \cdot \frac{\lambda}{D} \quad (4.7)$$

where D is the diameter of the telescope (Monnier 2003).

For the resolution of an interferometer one has to go back to Equation 4.1. For a fringe pattern of a single point source, given by $I \propto (1 + \cos(k\alpha B))$, the angular distance between two fringes is given by $\alpha = \lambda/2B$. One can now approximate the resolution limit with the angle at which a second point source has to be, in order to exactly cancel out the interference pattern. This is given by:

$$\Theta = \frac{\lambda}{2 \cdot B} \quad (4.8)$$

With the difference, that B in this case is the length of the longest baseline, which is usually much larger than the telescope diameter (Monnier 2003).

However, with the increased resolution, there are also some disadvantages of interferometry. As one usually only measures the visibility, one has to use different reduction and imaging algorithms to get an actual image (Monnier 2003; Glindemann 2011). Furthermore, as the Fourier transformation adds an inverse behavior to distance, interferometric observations tend to filter out large scale structure (Thompson et al. 2017). This is due to the limit of the shortest baselines one can create, usually given by the telescope diameter. There are more complications which one has to consider, as for example the finite size of the telescopes, but as this would go beyond the scope of this work, I am not dealing with these complications here and assume a perfectly working interferometer. For more information on this see e.g. Jackson (2008).

4.2 OPTICAL INTERFEROMETRY

So far everything said about interferometry was independent of the wavelength. However, when one uses an interferometer in the optical or NIR, one encounters some complications in comparison to the traditional radio interferometers. Due to the much shorter wavelengths

the error for measuring interferometric fringes has to be much smaller. This requires first of all a much higher precision in all the optical elements of an interferometer. While this can theoretically be overcome with improving building techniques for the telescopes, one has to deal with another complication, which is usually not of importance for radio astronomy: the influence of the atmosphere. Additional to the larger error budget, radio interferometry is usually done in wavelengths where the atmosphere only has little effect on the incoming radiation (Rohlfs and Wilson 1996). The assumption that the atmosphere has little effect on the observation does not apply for interferometry in the optical and NIR, as discussed in chapter 2. For a single telescope the effects of the atmosphere can be reduced by adaptive optics. However, as the common WFSs work on the first or second derivative of the wavefront, they cannot determine the mean phase change due to atmosphere (see chapter 3). This change in the average phase is also referred to as change in atmospheric piston.

For a single telescope the piston is usually not of relevance, but for an interferometer the relative phase of the light at the two telescopes is an important parameter. A random change in the piston difference, due to the atmosphere, introduces a jitter in the optical path difference (OPD) between the two telescopes, as I show in the following.

Another complication in optical interferometry comes from the possible observational techniques. Interferometers in the radio regime use a heterodyne detection, which means that the incoming signal is compared to an artificial signal from a so-called local oscillator, which has a very similar frequency to the observed signal. The local oscillator has to have a precisely known and very stable frequency. By comparing the incoming light with the signal from the local oscillator, one can directly determine and save the phase and amplitude of the incoming light. This has the main advantage that one can create the interferometric fringes after the actual observation. However, at optical and NIR wavelengths a heterodyne detection is not possible, mainly due the fact that there are no appropriate sources for a local oscillator at shorter wavelengths. Therefore, the detection has to be done in a homodyne mode and the fringes have to be created in real time during the observation (Glindemann 2011). This is one of the main reasons why optical interferometers have to use fringe tracking systems, in order to create fringes in real time.

ATMOSPHERIC EFFECTS ON INTERFEROMETRY

While atmospheric turbulence decreases the resolution of a single telescope (see Equation 2.9), the effect for an interferometer is different. The atmosphere introduces a phase difference between the two used telescopes which results in a lower fringe contrast (or a lower visibility). This ultimately decreases the sensitivity of the interferometer (Buscher 2015, pp. 53-54).

The effect of the atmosphere can be best seen for an interferometer whose individual telescopes are not affected by the atmosphere. This means that either the diameters of the telescopes are smaller than r_0 , or the atmospheric effects are corrected by an AO system. However, the baseline of the interferometer is usually larger than r_0 , which means that the interferometer is affected by the atmosphere. The difference in phase at the two telescopes

$(\phi_1 - \phi_2)$, introduced by the atmosphere, can than be evaluated with Equation 2.7. As a parameter for the phase offset one usually uses the root-mean-square (RMS) value:

$$\sigma_\phi = \sqrt{\langle(\phi_1 - \phi_2)^2\rangle} = \sqrt{D_\phi(B)} \quad (4.9)$$

For a typical configuration in the optical ($\lambda=0.5\text{ }\mu\text{m}$) with a baseline of 10 m and a r_0 of 20 cm, this equation gives an RMS value of approximately 70 radians, which corresponds to an OPD of 5 μm or 10 times the wavelength. Such a big phase difference between the two telescopes will erase all the information from the interferometric fringes. This result is not the whole picture, as also the outer scale and the finite size of the individual telescopes play a role in the value of the fringe motion (Glindemann 2011, pp. 205-206). However, the conclusion stays the same: The atmospheric piston differences between the two telescopes have to be corrected, otherwise the measurement of the visibility will be meaningless. This correction is done with a fringe tracker, which I discuss in the following section.

There are some possibilities to avoid this problem. This can be for example done by measuring observables which are not affected by the atmosphere, such as the visibility modulus. Another possibility is to take measurements where the atmospheric effects are divided out as it is done for the closure phase. However, as this is not part of this work more information can be found in the literature, for example in Monnier (2003).

4.3 FRINGE TRACKER

The fringe tracker has a similar function for the interferometer as the AO system for a single telescope: it reduces the effects of the atmospheric turbulence by stabilizing the fringe motion. This is done by measuring the temporal variations of the piston mode and correcting for this value with a delay line. The fringe motion should then be reduced to a small jitter which allows to integrate over a longer time to observe the science target. In principle there are two different kind of delays: the phase delay and the group delay. A fringe tracker has to compensate both of them, in order to ensure good observations.

PRINCIPLE OF FRINGE TRACKING

The main principle of a fringe tracker is to combine the signal of the telescopes pairwise and to determine the maximum fringe contrast in the interferogram. By scanning the fringe pattern rapidly and correcting the fringe motion after each scan with a delay line, the OPD can be stabilized. However, there are several complications in doing this measurement. One of the main points is that the finite spectral bandwidth introduces a degeneration, as multiple fringes are visible in the interferogram. This can be avoided by limiting the fringe pattern with the use of a temporal (as used for FINITO, Gai et al. 2004) or a spatial modulation (used for GRAVITY Choquet et al. 2010). A spatial modulation offers a higher signal-to-noise ratio (SNR). However, it introduces additional noise sources which makes the two systems comparable. For a full description of the methods and the derivation of the different fringe pattern, see chapter 6 in Glindemann (2011).

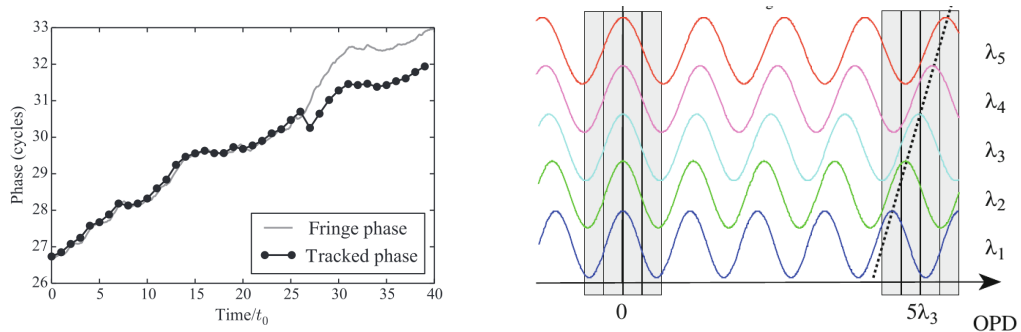


Figure 4.4: Left: Example of a simulated phase jump due to phase tracking (Buscher 2015). Right: A fringe package distributed into five spectral channels. The black dotted line shows the measured phase difference in each channel (Glindemann 2011).

One problem of the so far introduced tracking is that it only tracks the phase delay. This means that the fringes are stabilized, but there can still be a group delay of a multiple of the wavelength. This comes due to the fact, that the atmospheric piston difference is likely to be several times 360° (as indicated by Equation 4.9). As there is no possibility to distinguish between different fringes in the phase tracking, the final measurement is ambiguous to a multiple of 360° . With this technique alone it is therefore very likely to get phase jumps of 360° , even when the fringes are stabilized (an example for this is shown in the left image of Figure 4.4). This can happen for example for short flux-drops or longer integration times (Buscher 2015). The phase jumps become a problem when the science observation is done at a different wavelength than the tracking, as the jumps are then not equal to one wavelength and introduce a fringe shift. Furthermore, several jumps can introduce a random walk like behavior, which ultimately leads to large differences in the real and measured OPD. Another reason for fringe jumps can be a strong atmospheric dispersion, for example due to the so called water vapor seeing. That is varying amount of water vapor above the two telescopes, which creates significant random fluctuations in phase (Meisner et al. 2012). These jumps also have to be detected and corrected by the fringe tracking system, as they are not independent of the wavelength.

In order to avoid these jumps, it is important to find the actual path difference, indicated by the white-light fringe. This is done by group delay tracking. For this method the light is distributed into several spectroscopic channels and from the different responses one can get the information of the distance between the scanned fringe and the white-light fringe. When one measures the fringes with no OPD, the phase of each measurement is the same. For an OPD of several wavelengths the phases in each spectroscopic channel are different (see right image of Figure 4.4). From the differential phase of the different channels the position of the white-light fringe can be calculated and the according path difference then corrected by the delay line (Glindemann 2011, p. 298). As both delays, the phase and the group-delay, have to be corrected, the two tracking methods are usually combined within a fringe tracker (for GRAVITY as an example see Choquet et al. 2010).

FRINGE TRACKER AT LBT & VLTI

There are currently three fringe tracker systems which are operational or planned at the VLTI and LBT. The oldest system is the FINITO fringe tracker which is operational since the end of 2007 at the VLTI (Le Bouquin et al. 2008). A later analysis by Mérand et al. (2012) showed an optimal performance for low wind speeds with an RMS of 50 to 150 nm. However, for higher wind speeds this value increases up to a RMS larger than 700 nm for some of the UT pairs. In this study the limiting magnitude for FINITO was found to be 5.5 magnitudes in the H-band.

The second fringe tracker at the VLTI is the GRAVITY fringe tracker (Choquet et al. 2010). GRAVITY is a second generation instrument for the VLTI which currently produces its first results (GRAVITY Collaboration 2017). The internal fringe tracker is supposed to deliver a maximum in residual fringe motion of 300 nm and has a magnitude limit of 10 magnitudes in the H-band.

Another system which was developed for the VLTI but canceled in 2014, is the PRIMA fringe sensor unit (FSU) (Sahlmann et al. 2009; Woillez et al. 2014). Although this system was only used for a short time in combination with MIDI (see e.g. Müller et al. 2014), I later show some results from the testing period.

For the LBT there are two possible fringe trackers for the future. The current possibility is the Large Binocular Telescope Interferometer (LBTI) instrument (Hinz et al. 2016) which obtained its first fringe-tracked observations in 2013 (Defrère et al. 2014). The second possibility for the future is the LINC-NIRVANA instrument which arrived at the LBT in 2016 and is currently in the commissioning phase. When at full functionality, LINC-NIRVANA will also include a fringe tracking system (Bertram et al. 2006; Straubmeier et al. 2006).

LIMITS OF FRINGE TRACKERS

Without a fringe tracker it is not possible to directly measure the visibility from an optical interferometer. Despite the importance of the system there are still some struggles with the current designs.

One of the main problems is that, in order to follow the piston fluctuations from the atmosphere, the fringe tracker has to run in a comparably high frequency. Starting from a simple transfer function, Glindemann (2011, p. 295) showed that a scan rate of 250 Hz is necessary to reduce the residual fringe motion to a few hundred nanometers. In principle an even higher frequency would decrease the jitter, as the fringe motion between the measurements would be lower. However, for shorter measurement times less light from the guide star is available and noise effects increase, which leads to a worse fringe measurement. Therefore, for each system there is an optimum exposure time, in order to get the best SNR possible with the best fringe motion sampling. This is done by balancing the noise effects with the under sampling of the fringe motion. In order to achieve this, one needs a comparably bright guide star to measure the OPD from the atmosphere. For the GRAVITY fringe tracker for example, which is currently the most advanced system, the guide star

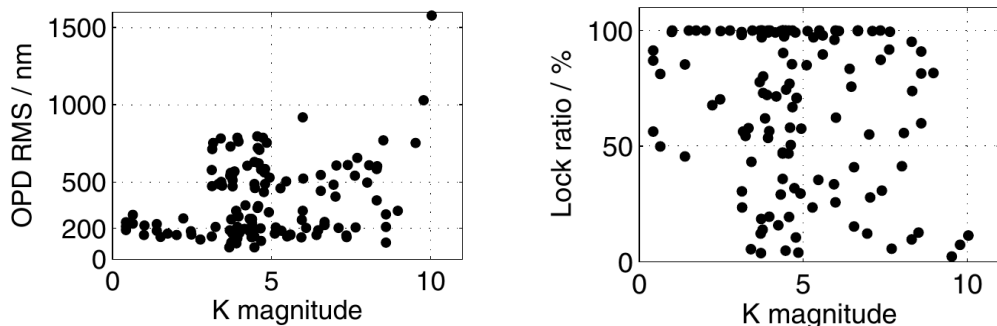


Figure 4.5: Performance of the PRIMA fringe tracker as a function of K-Band magnitude shown with the OPD SNR (left) and the lock ratio (right), which is the fraction of time over one minute in which the tracker works properly. Adapted from Sahlmann et al. (2009).

has to have at least a magnitude of 10 in the K-Band (Choquet et al. 2010)³. For FINITO, the older fringe tracker at VLTI, the source has to be even brighter⁴ (see also section 4.3). These values fit with the result from Glindemann (2011, p. 296) from a comparison between the photon noise and the variance from fringe motion. Similar results have been obtained by Sahlmann et al. (2009) during testing of the PRIMA fringe sensor unit for VLTI, where the RMS of the fringe sensor strongly increases towards fainter targets (see Figure 4.5).

In conclusion, this means that for science targets fainter than $m_K=10$, one has to observe them in a dual feed mode with a separate guide star. However, in dual feed mode one can only observe a target if a sufficient bright guide star is close to it. Due to the properties of the interferometers such a guide star has to be comparably close to the target (for example between 0.4" and than 2" for GRAVITY).

However, there are some additional problems that can occur at fringe trackers which are mainly stability problems due to flux dropouts, phase jumps, or instrumental vibrations. Flux dropouts occur when the flux at the telescope is too low to acquire enough signal for the fringe tracking. This can either be due to atmospheric effects, such as scintillation or strong turbulences, or due to mechanical effects, such as vibrations as propagating tip-tilt errors (Le Bouquin et al. 2008; Choquet et al. 2010). There are some solutions for overcoming flux dropouts from mechanical effects (see e.g. Pfuhl et al. 2010). But in order to reduce the effects of atmospheric flux dropouts, one would either need a predictive system (Menu et al. 2012), or one has to increase the SNR on the fringe tracker, in order to avoid the dropouts in the first place.

IMPROVING THE FRINGE TRACKER MEASUREMENTS

In order to tackle the problems of faint guide stars and flux dropouts, the most simple approach would be to increase the SNR of the fringe tracker measurement. This could be

³Gravity Instrument Description, <http://www.eso.org/sci/facilities/paranal/instruments/gravity/inst.html>, visited on 06.06.2017

⁴VLTI User Manual, <https://www.eso.org/sci/facilities/paranal/instruments/gravity/doc.html>, visited on 06.06.2017

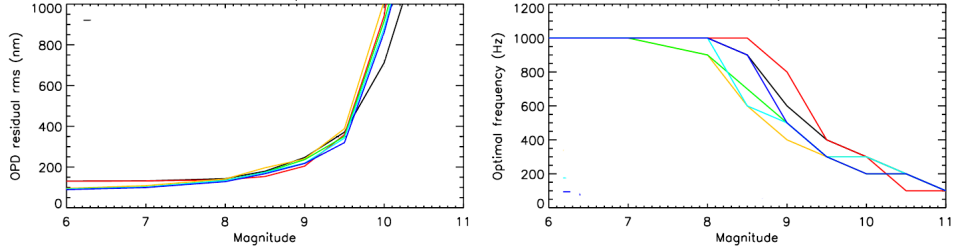


Figure 4.6: OPD as a function of magnitude (left) and optimal frequency as a function of magnitude (right) from simulations similar to the GRAVITY fringe tracker. The different colors show different fringe tracking models from Choquet et al. (2014).

achieved by increasing the exposure time of the fringe tracker measurement. A longer exposure time would increase the signal, as more photons could be captured from a faint object. It would further raise the SNR, as the noise is mainly due to photon noise, readout noise and internal vibrations. The possible improvement of the SNR was also shown in simulations by Choquet et al. (2014). They calculated the optimal fringe tracker frequency and especially for faint stars a considerably shorter frequency than the usual used several hundred Hertz would lead to an increasing SNR (see Figure 4.6).

But as mentioned earlier this is usually not possible as the OPD variation would increase and one would under sample the piston evolution. A very simple way of looking at this is by considering the atmospheric coherence time. For an exposure time longer than the atmospheric coherence time, the fringe contrast decreases and the visibility is reduced. In analogy to the Fried parameter the coherence time is defined as the time difference when the RMS phase fluctuations at a single point have a value of 1 rad (Saint-Jacques and Baldwin 2000). The approximation for this is usually given by:

$$\tau_0 = 0.3 \frac{r_0}{v} \quad (4.10)$$

For a typical wind velocity of 10 m s^{-1} and a r_0 of 0.7 m, which corresponds to good seeing in the NIR, this gives a coherence time of 20 ms (Glindemann 2011).

A more exact way to approach this is by taking a closer look at the evolution of turbulence over two telescopes. This can be done by considering a more accurate version of Equation 4.9, in which now the two telescopes are represented by two delta functions. The convolution with the phase evolution then gives the differential phase between them:

$$\Delta\phi(\vec{r}) = \phi(\vec{r}) * (\delta(\vec{r} - \vec{B}/2) - \delta(\vec{r} + \vec{B}/2)) \quad (4.11)$$

By computing the square of the Fourier transformation of this equation and using Equation 2.7, one then gets the power spectrum of the OPD fluctuations:

$$\Phi(\vec{k}) = \frac{\lambda^2}{\pi^2} 0.0229 r_0^{-5/3} |\vec{k}|^{-11/3} \sin^2(\pi \vec{B} \cdot \vec{k}) \quad (4.12)$$

One can now assume TFFH and integrate this power spectrum along the wind velocity. From this the OPD variations can be estimated by convolving the result with a rectangular

filter function in time and the computing the variance over the used time. One then arrives at the following function:

$$\sigma_{OPD} = 0.19\lambda \left(\frac{\bar{v}}{r_0}\right)^{5/6} \cdot T^{5/6} \quad (4.13)$$

where T is the integration time and \bar{v} the mean wind velocity (for a full derivation of this function see Tango and Twiss (1980) and Glindeemann (2011)). This result clearly shows that the RMS of the OPD increases with exposure time. For typical values, such as a wind velocity of 10 m s^{-1} and a r_0 of 0.7 m at $2.2 \mu\text{m}$, one already gets an OPD RMS of 640 nm for 100 ms . As this value is already higher than the usual goal of a fringe tracker (e.g. 300 nm for GRAVITY), this shows that decreasing the fringe tracker frequency in order to get a better SNR is not possible without compensating for the piston evolution on short timescales.

PISTON RECONSTRUCTION

5

With this final chapter of the thematic part I now introduce the main topic of this work. In the previous chapter the problems of the current fringe tracking systems have been pointed out. In order to overcome this problems, I introduce a new technique to reconstruct the evolution of the atmospheric piston over a single telescope. This piston reconstruction technique can increase the exposure time of a fringe tracker and with that increase the sensitivity of optical interferometers.

For this purpose I present two different methods for the piston reconstruction. Both of them are based on a validity of Taylor's Frozen Flow Hypothesis (TFFH) over short time scales and depend on a reliable measurement of the dominant wind velocity in the atmosphere. In the following I present both methods and point out their advantages and disadvantages.

5.1 MOTIVATION

The goal of this work is to develop and test an algorithm which can reproduce the piston evolution over a telescope for short timescales. The main reasons why such a system could be helpful are described in section 4.3: fringe trackers tend to have a poor performance for faint targets or guide stars. Especially for such faint sources instability issues, such as flux dropouts, occur at the fringe tracker. Both problems are caused by a poor SNR of the fringe tracker measurement. This is mainly due to the fact that the exposure time of the fringe tracker has to be as short as possible in order to follow the fast OPD variations (see Equation 4.13).

The approach in this work is therefore to develop a system which can compensate the OPD variation on short timescales (below one second). If it is possible to keep the interferometric fringes stable over such a timescale, it would be possible to significantly increase the exposure time of the fringe tracker. This would reduce the stability problems and make the fringe tracking more efficient. More importantly, it would increase the magnitude limit for guide stars and would therefore make a lot of scientific objects available to optical interferometry which are currently not observable, as they are too faint and there is no appropriate guide star close to them.

Therefore, the piston reconstruction system could significantly improve the performance of optical interferometers by running the usual fringe tracker at lower frequencies and combining it with a high frequency system, in order to stabilize the fringes over short timescales. However, even with a perfectly working piston reconstruction, the fringe tracker would not become redundant, as one still needs the actual fringe position to start the piston drift reconstruction. The reason behind this is that one cannot measure the absolute piston, but only the piston variations. The idea is therefore to eventually combine

the fringe tracker with the piston reconstruction system in a nested loop. With such a combination, the requirements of a fringe tracker would decrease, which would make the whole system more reliable and make optical interferometry available for faint objects. Another main advantage of the piston reconstruction system that is presented here is that it works with the data from the AO system. As all the eight meter class telescopes are equipped with an AO system, there is no need for additional hardware at the telescope, which makes this system feasible with comparably small effort. A full overview of the use of the piston drift reconstruction as well as the advantages and possible complications follows at the end of this chapter.

ASSUMPTIONS

To model the performance of the piston reconstruction, I need to make a few assumptions on the atmosphere, which have been discussed in chapter 2.

The first main assumption for the used atmospheres in this work is that the atmosphere is composed of several layers, each layer with a spectrum of atmospheric turbulences following the Kolmogorov spectrum. The total measured turbulence is the superposition of all of these layers. The ground layer is the dominant one and is responsible for around 65% of the whole turbulence.

The second assumption is that Taylor's Frozen Flow Hypothesis (TFFH) (section 2.3) is true for the relevant timescale, which can be up to 20 ms. This is the maximum timescale for one iteration of the piston drift reconstruction in order to not be influenced by boiling. However, one can use longer timescales for the wind detection, as a further result from the different atmosphere studies is that the wind velocity and direction are constant over much longer timescales. This shows that the temporal restriction comes from the boiling itself, not from the wind measurement.

5.2 P-REX

For the actual calculation of the piston drift above the telescope, I try two different approaches. The first one, in the following called the *P-REx wavefront algorithm*, is the complete calculation using the reconstructed wavefronts from the WFS. The second possibility is something like a first order approximation of the full P-REx algorithm. It does not use the full wavefront information, but calculates the piston directly from the measured Tip and Tilt values. Therefore, it will be referred to as the *P-REx Tip-Tilt algorithm*. Both ideas are schematically shown in Figure 5.1. In the following two sections, I present both ideas and outline the advantages and disadvantages of both concepts.

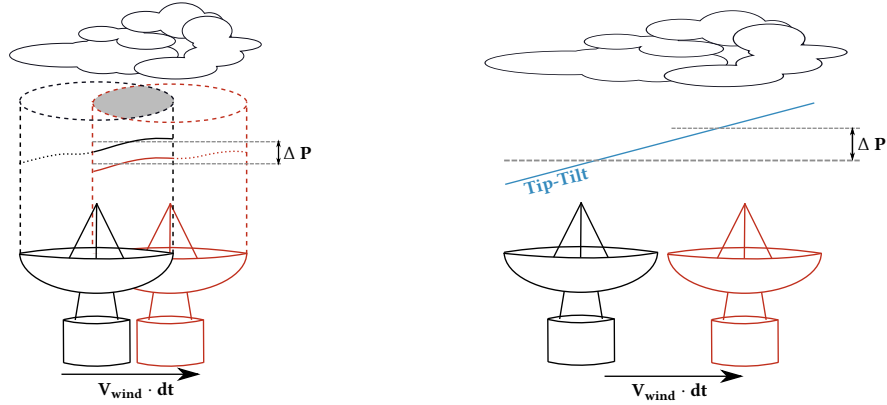


Figure 5.1: Schematic representation of the two P-REX concepts: the complete P-REX concept with the usage of the whole wavefront (left) and the Tip-Tilt approximation of the piston reconstruction (right).

THE P-REX WAVEFRONT CONCEPT

The concept of piston reconstruction presented here, is based on a few individual steps, which were introduced by Pott et al. (2016) and are explained in the following.

In a realistic AO system, a feedback control loop is usually applied. Therefore, one does not get the full phase information from the WFS, but only the residual phase. For the piston reconstruction one needs the full wavefront information, which can be achieved by a pseudo open loop (POL), using the shape of the DM and the WFS data. The POL data is calculated with the following formula: (see e.g. Guesalaga et al. 2014)

$$S_i^{pol} = S_i^{res} + IM \cdot V_{i-1} \quad (5.1)$$

In this formula S_i^{pol} is the POL data at a discrete time i in units of the WFS (e.g. slopes for a SH sensor). S_i^{res} is the measurement of the WFS and V the voltages applied to the DM, which is converted into WFS units with the IM (see section 3.3).

However, for this approach it is necessary to use the actual wavefront and not the data in WFS units. Therefore one has to use a wavefront reconstruction to calculate the POL wavefront (ϕ). With these wavefront data, one can then calculate the piston-free wavefront $\hat{\phi}_1$ and $\hat{\phi}_2$ of two adjacent phases:

$$\hat{\phi}_1(x, y) = \phi_1(x, y) - P_1 \quad \hat{\phi}_2(x, y) = \phi_2(x, y) - P_2 \quad (5.2)$$

with the real wavefront $\phi_i(x, y)$ and the piston P_i . The piston is simply the mean of the wavefront. The value we want to know from the analysis is the piston variation between these two wavefronts:

$$\Delta P = P_2 - P_1 \quad (5.3)$$

However, from the AO data one only gets the the piston-free wavefronts $\hat{\phi}_1$ and $\hat{\phi}_2$ and the piston variation is therefore unknown.

The first step to reconstruct the piston is to get the shift between the two wavefronts. With the TFFH, this shift corresponds to a spatial displacement due to the wind velocity times

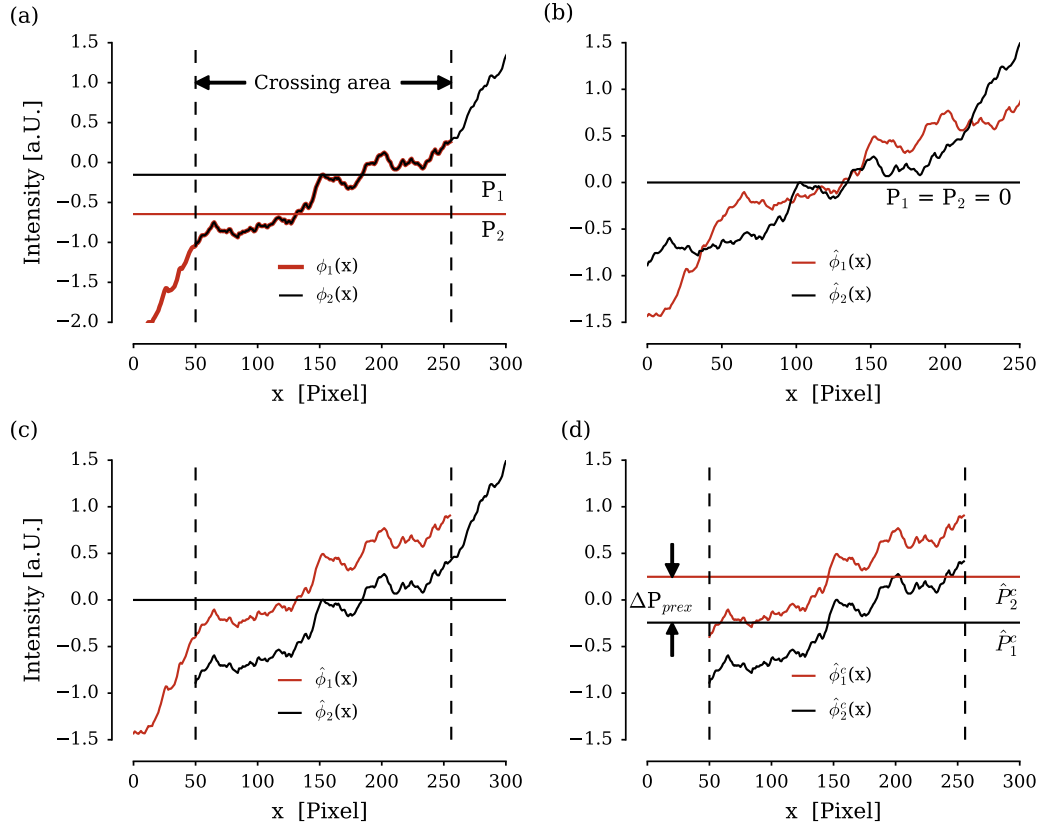


Figure 5.2: Schematic representation of the P-REx concept in 1D. (a) Initial 1D-wavefront of two frames with a small time difference resulting from the atmosphere. The wavefront in the crossing area is the same for both parts. (b) Wavefront as measured by the AO system with the mean values (piston) set to zero and not corrected for the wind shift. (c) Same as in (b), but with the correct spatial shift, determined with a cross correlation. (d) Only the wavefront in the overlapping region with the corresponding mean values. The difference between them is the searched parameter.

the time difference. At this point I only assume a single turbulence layer. This is not correct, but as the major part of the turbulence comes from the ground layer, we can assume that we will measure the wind velocity from this ground layer. Therefore, from here on I will refer to the wind velocity as the wind velocity of the ground layer. All the other atmospheric parameters (such as piston, tip, and tilt) will always be derived from the whole atmosphere. In order to determine this shift between the wavefronts, I use the approach of a normalized cross correlation, which has been proven to be reliable (Reddy and Chatterji 1996; Pott et al. 2016). This is discussed in detail in chapter 7.

The two phase maps have a common crossing area at which the phase and the piston of both maps are identical. With the wind speed, determined by the cross correlation, one can calculate this crossing area in which the wavefront of both measurements, and therefore also the piston, is theoretically identical. In the data, however, the global piston is set to zero for both wavefronts, which leads to different mean piston values in the crossing area (see Figure 5.2). For the two wavefronts in the crossing area one measures the phases $\hat{\phi}_1^c(x, y)$ and $\hat{\phi}_2^c(x, y)$:

$$\hat{\phi}_i^c = \hat{\phi}_i[\text{crossing area}] \quad (5.4)$$

In contrast to the piston free wavefronts ($\hat{\phi}_i$), the wavefronts of the crossing area ($\hat{\phi}_i^c$) have a non-zero piston (lower right image in Figure 5.2):

$$P_1^c = \langle \hat{\phi}_1^c(x, y) \rangle \quad P_2^c = \langle \hat{\phi}_2^c(x, y) \rangle \quad (5.5)$$

By measuring these mean values of the wavefronts in the crossing area, one finally gets:

$$\begin{aligned} \Delta P_{P-REx} &= P_2^c - P_1^c = \langle \hat{\phi}_2^c(x, y) \rangle - \langle \hat{\phi}_1^c(x, y) \rangle \\ &= \langle \phi_2^c(x, y) + P_2 \rangle - \langle \phi_1^c(x, y) + P_1 \rangle \end{aligned} \quad (5.6)$$

By considering the fact that in the crossing area the two real wavefronts (not piston reduced) are identical ($\phi_1^c(x, y) = \phi_2^c(x, y)$), one finally gets:

$$\begin{aligned} \Delta P_{P-REx} &= \langle \phi_2^c(x, y) - P_2 \rangle - \langle \phi_1^c(x, y) - P_1 \rangle \\ &= \langle -P_2 \rangle - \langle -P_1 \rangle = -P_2 + P_1 \\ &= -\Delta P \end{aligned} \quad (5.7)$$

This is the desired conclusion, which shows that one can use the piston of the crossing area to determine the differential piston of two wavefronts. For a schematic representation of the complete concept see Figure 5.2.

The concept is mathematically easy and works perfectly under idealized conditions (i.e. no noise, perfect TFFH). However, this concept also has its downsides. In real AO systems there is not always a calculation of the actual wavefront. One usually rather uses an IM, which directly translates the WFS slope measurements to DM voltages. For the P-REx calculation, there is no need to reconstruct the wavefront for the wind measurement, as one can calculate the wind vector directly from the WFS signal (see chapter 7). For the calculation of the differential piston however, this concept needs the reconstructed wavefront. This means an additional computation burden and makes the algorithm comparably slow.

THE P-REX TIP-TILT CONCEPT

The second concept is very similar to the previous one, it does however not need a reconstructed wavefront. The only information we need for this concept is the wind vector and the tip and tilt values of the wavefront. The idea here is that the first orders of the Kolmogorov spectrum have the biggest amplitudes (Hardy 1998) and therefore have the largest influence on the piston. The approximation for this concept is, that one has to assume that only the tip and the tilt values ($\vec{T}\vec{T}$) are relevant. With this approximation one can calculate the piston variation with the following equation:

$$\begin{aligned}\Delta P &= \vec{T}\vec{T} \cdot \Delta s = \vec{T}\vec{T} \cdot \vec{v}_{wind} \cdot \Delta t \\ &= [\text{tip} \cdot v_x + \text{tilt} \cdot v_y] \cdot \Delta t\end{aligned}\tag{5.8}$$

Δs is the displacement vector of the wavefront (see Figure 5.1), \vec{v} is the wind vector, and Δt is the time over which the piston variation is measured. The tip is the first derivation of the wavefront in x direction and the tilt in y direction. All parameters are again taken from the POL wavefronts, as defined in Equation 5.1, in order to get the full atmospheric information.

This calculation is, as mentioned, only an approximation, assuming that all the modes after tip and tilt can be neglected. The idea behind this is that a local piston drift is the derivative of the phase, which is given by the tip and the tilt. Another way of looking at the dominant role of tip and tilt is by looking at the power spectrum of atmospheric turbulences. There the first modes, namely tip and tilt, are the most dominant ones. Therefore the tip-tilt approximation seems to be a valid assumption. How good it really is has to be shown in tests and simulations.

This second concept carries one obvious performance advantage: all the information one needs is (usually) directly given by the AO system. For a system with a SH or a pyramid sensor for example, the tip and tilt are given by the mean of the measured x- and y-slopes, which by definition represent a derivation of the wavefront (section 3.2). In this case there is no need for an additional wavefront reconstruction. This is not directly obvious for a curvature sensor, as it does not measure the tip and tilt values. However, curvature systems are usually also equipped with a tip-tilt measurement and a tip-tilt DM, which delivers the necessary information. Therefore, one only has to calculate the POL data from the WFS and the DM (see Equation 5.1). From this POL data, the shift and the tip and tilt values can be derived and no further reconstruction of the wavefronts is needed. This saves computational resources and makes the concept faster than the P-REx reconstruction algorithm. Therefore, this second concept is probably the more promising one, especially due to a faster algorithm. In the next part, I describe the end-to-end simulations used for this thesis and test the simulated performance of both variants of the P-REx algorithm under realistic conditions.

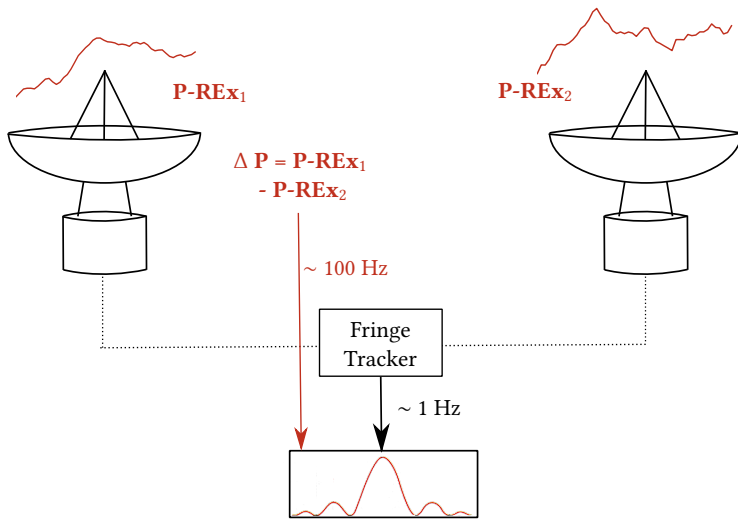


Figure 5.3: Sketch for the use of P-REx with a fringe tracker system. The red parts in the drawing are the additional measurements due to the P-REx implementation.

THE USE OF P-REX

In the following tests I mainly focus on the results of a piston reconstruction for a single telescope. This is possible as the piston measurement at an interferometer has to be done for each individual telescope and has then to be applied to the baselines of an interferometer. However, one should keep in mind how the system can finally be used.

The idea for the use of P-REx at an interferometer is as follows: The prerequisite is a stable fringe position at the beginning of the measurement. This is one of the reasons why P-REx cannot work without a fringe tracker. From the situation of visible fringes, the piston evolution can then be measured over each of the both telescopes. By calculating the difference between these two measurements one gets the differential piston movement between the two telescopes. This differential piston has then to be compensated by the existing delay lines in order to lock the stable fringes. The correction has to be done as often as possible, at least with a frequency of 100 Hz, in order to keep the fringe position locked. As the piston reconstruction is not error free, an error will add up during the time one uses P-REx to stabilize the fringe position. To reduce this error one again needs a working fringe tracker. The idea is therefore to run the fringe tracker over longer timescales than usual. A frequency of the order of a few Hertz should be enough to do away the increasing error from P-REx. With this system, the combination of the usual fringe tracker at low frequency and P-REx at high frequency, one can then stabilize the fringes. The best frequency for the fringe tracker in this system is an important factor for the use and has to be figured out later. However, the focus of this work is to determine the usability of the piston reconstruction in principle. Figure 5.3 shows the set up for a combination of P-REx and a fringe tracker.

The main advantage of the here proposed piston reconstruction is that it uses solely the data from the AO system and is therefore more photon-efficient. The AO system sits directly

at the telescope and does not suffer from photon losses such as the fringe tracker. This photon losses can be for example due to long delay lines or additional reflections in the light path. Furthermore, especially the *P-REx Tip-Tilt algorithm* is conceptually very easy and requires no long calculation. Especially when the wind measurement is decoupled from the actual piston reconstruction, it could run at higher frequencies than an usual fringe tracker, which would directly increase the sensitivity of the interferometer. Another important point for P-REx is that all the hardware it requires, such as the AO system and delay lines, are already available at the relevant telescopes. This shows that an implementation of the system at the telescope can be done relatively easy and requires no big expenses.

However, there are also some effects that could limit the usability of the system. First of all, there is the problem of atmospheric effects such as boiling and multilayer movements. The consequences of these effects are discussed in later parts of this work. Another problem could be additional piston changes that are not detected by the system. These changes could occur for example due to vibrations in the light path between the telescopes. Such effects especially play a role for long baselines, where the piston reconstruction could otherwise be very helpful. An approach to correct such effects can be a laser metrology system as it is used for GRAVITY (Lippa et al. 2016). However, not every interferometric instrument offers such a system.

In conclusion, there are several effects that have to be considered in order to make a prediction for the usability of P-REx. This work shows the first steps in this direction by analyzing the atmospheric effects and the general performance of a piston reconstruction over a single telescope. Further work will have to show how additional effects from the interferometer can be compensated.

Part II

WORKING WITH SIMULATIONS

YORICK ADAPTIVE OPTICS

6

In this part, I work with data generated by simulations of different adaptive optics systems. In order to generate the necessary data, I use the Yorick Adaptive Optics simulation (YAO). There are currently several possible AO simulations available, but YAO is one of the most frequently used tools for this purpose and should, therefore, work stable and deliver reliable results. Before starting with the data analysis in the next chapter, I shortly explain the main properties and the use of YAO.

Throughout this work I use simulated adaptive optics data to test and validate the proposed techniques. These data were produced using the Yorick Adaptive Optics simulation (YAO), an end-to-end Monte Carlo simulation software developed by Francois Rigaut (Rigaut and Van Dam 2013). For my work I used the version 5.7.0 with own changes, mostly necessary to get the required data as a result of the simulation.

YAO is a powerful simulation tool which includes all currently common types of wavefront sensors and deformable mirrors. It therefore allows to simulate a wide variety of different AO systems with realistic noise and error contributions. Apart from that, further advantages of YAO are that it is comparably fast (due to critical components coded in C and included with yorick) and it is used and improved for more than 15 years now, which makes it comparably bug free and up-to-date with current requirements for AO systems. In the past, YAO was for example used to model the Multi-conjugate Adaptive optics Demonstrator (MAD) (Marchetti et al. 2008) and the Gemini Multi-Conjugate Adaptive Optics System (GeMS) on the 8m Gemini South telescope (Rigaut et al. 2014).

THE USE OF YAO

The main part of an individual YAO run is the parameter file, which lists the main parameters of the simulated AO system. All important elements of a system (e.g. telescope, number and type of WFSs, different DMs,...) are dimensioned in this file. A simulation run by YAO then consists of four steps:

- **Reading:** In the first stage the parameter file is read. The simulation reads in all the input parameters and checks for invalid or missing settings, in order to prevent a failing simulation.
- **Initialization:** This stage prepares all the necessary parameters, calculates the relevant matrices, like the IM and CM, and loads the input files like the atmospheric phase screens. After finishing this part, all the preparations for a closed-loop simulation are ready.

- **Loop:** This part executes the actual simulation and simulates all the elements of an AO system. For every step in the total number of iterations, the WFS measurement is calculated for a specific part of the atmosphere, and then applied to the DM. After this step, the residual wavefront is calculated by using the atmospheric phase screen, the DM positions, and the effect of the telescope optics. This wavefront is then fed into the WFS, for the next iteration. If required different parameters can be shown after each loop.

YAO can either be used in interactive mode, where the point spread function (PSF) of the target star and different other parameters are continuously monitored, or in a terminal based mode, where the results of the simulation are saved into a diagnose file. YAO usually only saves relevant parameters, in order to show the performance of the simulated AO system. As more data from the simulation are required for the following analyses, I modified the original YAO script to get these outputs. This includes for example each individual WFS and DM measurement (for an overview see Figure 8.1) The modified script can be found on my github profile⁵. Some of the most important YAO parameter files I used for my simulations are presented in Appendix C.

Although this was only a very short introduction into YAO, it becomes clear that YAO is a very powerful tool to simulate the behavior of AO systems under different conditions. Therefore, it is very suitable for testing new methods, such as the Piston Reconstruction Experiment (P-REx), on several different AO systems. More information and the full capabilities of the tool can be found on the YAO homepage⁶.

⁵Github Profile of Felix Widmann, <http://www.github.com/widmannf>, visited on 02.04.2017

⁶YAO homepage, <http://frigaut.github.io/yao/>, visited on 02.04.2017

WIND VECTOR DETERMINATION

7

The first step for the piston reconstruction is the determination of the dominant wind vector. This has to be done as accurate as possible, as a wrong or inaccurate wind vector will directly lead to wrong results for the differential piston. In a realistic system one will always have several wind vectors from different atmospheric layers. However, for the sake of simplicity, I start with an one layer system with a constant wind vector and move then on to multilayer systems at the end of the section. This section also shows that it is possible to determine the wind vector directly from WFS measurements.

I want to make a general comment, before I start with this second part of my work. The following parts are heavily based on developing software for the different tasks and problems of the piston reconstruction. As the software itself is in general not of great interest for the reader, I explain my approach in the following sections and only add the corresponding code in a few cases, when the code itself represents a result of my work (see Appendix B). I refer readers who are interested in the whole software to my GitHub profile where the whole code is available as a Python module: <https://github.com/widmannf>.

7.1 NORMALIZED CROSS CORRELATION

As known from signal processing, one can find the displacement between two signals by calculating the cross correlation of them (Jähne 2005). This is also the usual approach when one wants to know the displacement between two measured wavefronts (see e.g. Schöck and Spillar 2000). For this reason I use a normalized cross correlation to measure the shift of two images. The usual normalized cross correlation between an image f and a template t is defined by:

$$T_{f,t}(\Delta x, \Delta y) = \frac{1}{N(\Delta x, \Delta y)} \sum_{x,y} \frac{(f(x, y) - \bar{f}) \cdot (t(x + \Delta x, y + \Delta y) - \bar{t})}{\sigma_f \cdot \sigma_t} \quad (7.1)$$

where \bar{f} and \bar{t} are the averages over the whole images and σ is the corresponding standard deviation. N is the so-called overlapping factor, which is equivalent to the number of overlapping pixels for each individual point of the cross correlation (Schöck and Spillar 1998). This factor compensates the effect that one has a different number of overlapping pixels for each position $(\Delta x, \Delta y)$ in the cross correlation. In my case, N can be calculated for each point by doing the auto correlation of the pupil image, an array which is in size identical with f and t , but only filled with ones. Other sources have introduced a more sophisticated overlap factor (see e.g. Guesalaga et al. 2014), but this is not necessary here,

as I am not dealing with additional effects which can occur in real atmospheric images, such as shadows from mirror mounts or traces of laser guide stars. The approach to use a normalized cross correlation in order to calculate a shift of the atmosphere, is very common and was used for example by Schöck and Spillar (2000). Other sources (e.g Wilson 2002; Guesalaga et al. 2014) used the same approach but directly with the measured slopes from SH sensors, which I discuss later.

As the cross correlation calculates the sum of two two-dimensional arrays, it is comparably slow. There are several approaches to decrease the computational effort of the normalized cross correlation (see e.g. Lewis 1995b; Briechle and Hanebeck 2001), but the easiest one is to use the relation that the cross correlation is equal to the inverse Fourier transformation of the cross spectrum (Jenkins and Watts 1968; Scargle 1989; Lewis 1995a). Therefore, the normalized cross correlation can be redefined as:

$$T_{f,t}(\Delta x, \Delta y) = \frac{1}{N(\Delta x, \Delta y) \sigma_f \sigma_t} \mathcal{F}^{-1} [\mathcal{F}(f(x, y) - \bar{f}) \cdot \mathcal{F}^*(t(x, y) - \bar{t})] \quad (7.2)$$

where \mathcal{F} is the Fourier transformation and the rest of the notation is identical to Equation 7.1. N is then as before calculated from the pupil image:

$$N(\Delta x, \Delta y) = \mathcal{F}^{-1} [|\mathcal{F}(\text{pupil}(x, y))|^2] \quad (7.3)$$

with $\text{pupil}(x, y)$ equals 1 inside the pupil and 0 otherwise (see e.g. Saint-Jacques 1998).

Figure 7.1 shows the cross correlation for the example of two images, which are shifted by 20 pixels relative to each other. The cross correlations are calculated with both methods, Equation 7.1 and Equation 7.2. The results from both calculations are identical, but the second approach uses a fast Fourier transformation (FFT) for the calculation, which decreases the required computation time from several seconds per cross correlation down to a few milliseconds. Therefore, I from now on always use Equation 7.2 for the normalized cross correlation.

In order to test the cross correlation without any additional effects, I take a large phase screen which was generated by YAO and cut out circular parts. By cutting out areas with a shift of one pixel relative to each other, I generate a very simple time series of a moving wavefront. The time series then has a wind velocity of one pixel per time step. The resulting images are normalized in the same way as proposed by Schöck and Spillar (2000) and are then used as the input for the cross correlation tests. By doing this, one gets a realistic model of a moving atmospheric layer without disturbing noise.

First tests of the cross correlation approach already showed good results in reproducing the shift between two images of a phase screen. However, the results are often slightly wrong, with an error in the detected shift of two or three pixels (for an example see Figure 7.3). This error is due to the fact that the pixel value of one pixel is not completely uncorrelated with the values of its neighbors, as the phase screen was created according to the Kolmogorov spectrum. The correlation between the pixels leads to an additional signal in the cross correlation and to a slight shift of the peak. This effect can be avoided by different approaches. The most intuitive one is not to use the image itself, but to look at the first or second derivative. In order to do this, I use a Laplace filter which is described in the following.

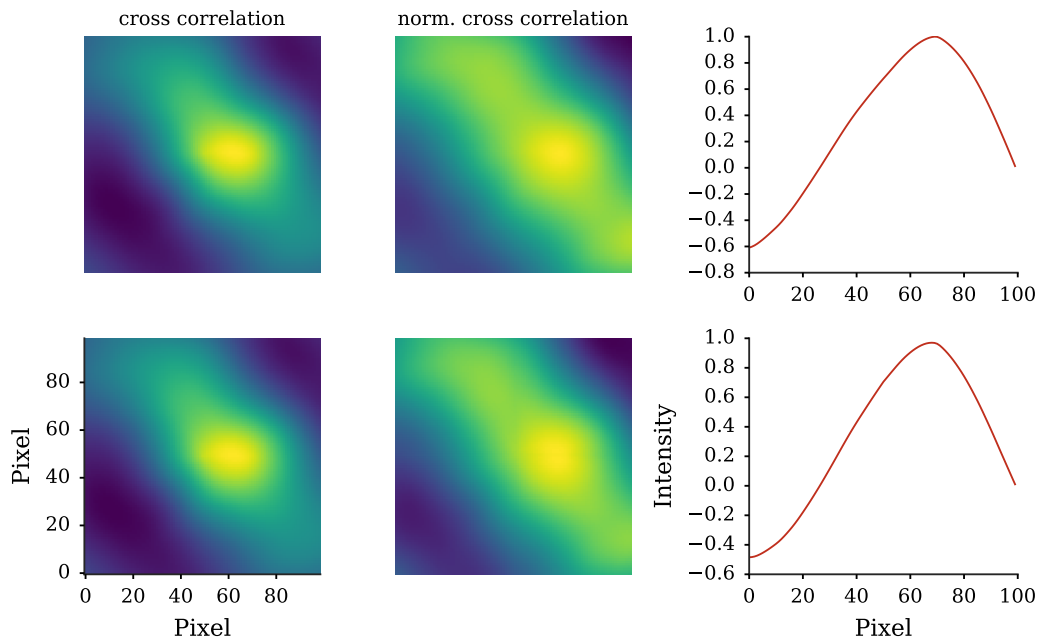


Figure 7.1: A comparison of the cross correlation with summation (upper images) and Fourier transformation (lower images). The used image and kernel are shifted by 20 pixels. The left images show the cross correlation without the normalization factor, which adds an additional signal in the middle of the image. The middle images show the normalized cross correlation and the right images show a cut through the normalized cross correlation at $y = 50$. In the middle and the right image the shift of approximately 20 pixels is clearly visible.

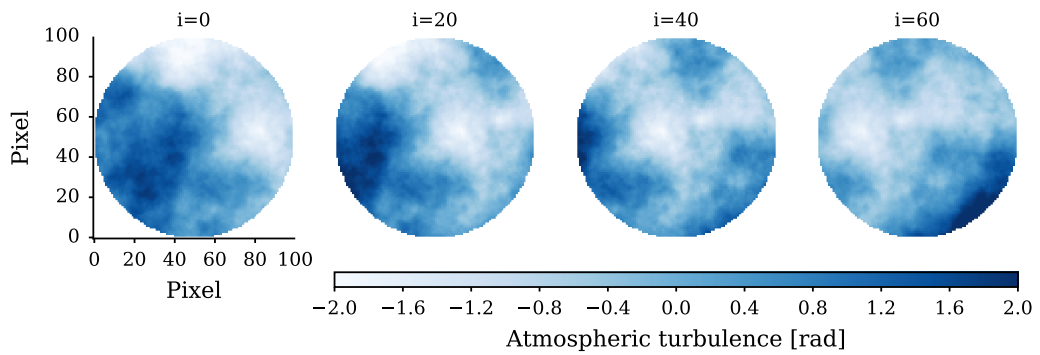


Figure 7.2: Example of a simulated atmospheric time series from a YAO phase screen. The individual images have a shift of 20 pixels to each other, which corresponds to a wind velocity of one pixel per time step.

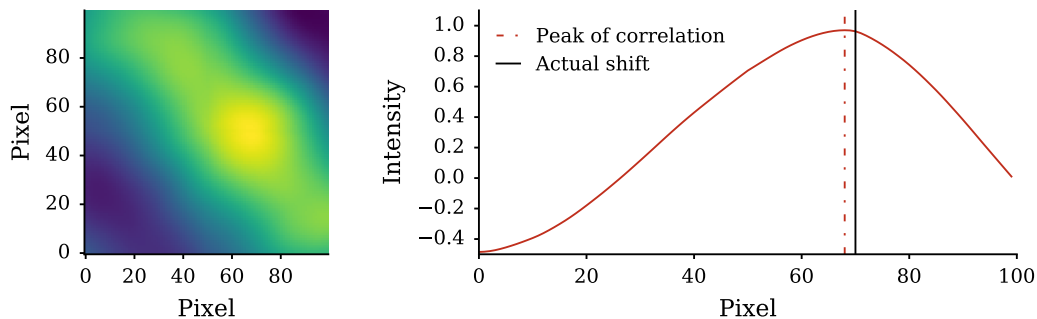


Figure 7.3: Example of a normalized cross correlation of two test images. The two used images are shifted by 20 pixels with respect to each other. The left plot shows the complete cross correlation and the right plot is a cut in x direction at $y = 50$. The dashed vertical line shows the peak of the correlation where it actually is and the solid line where it is supposed to be.

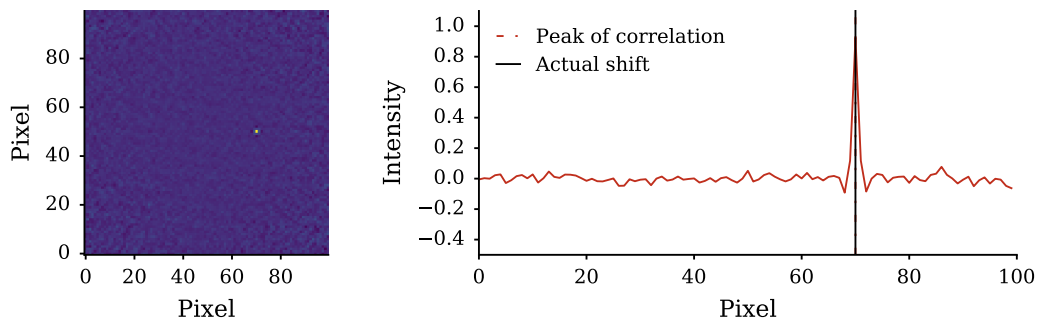


Figure 7.4: Same principle as in Figure 7.3, but with the use of Laplace filters before calculating the normalized cross correlation.

LAPLACE FILTER

To increase the sharpness of the cross correlation one can use different edge detection techniques. These techniques aim to identify points in the image, where the brightness changes rapidly. This can for example be done by using a filter which simulates the first (e.g. Sobel filter) or the second derivative of the image (Laplace filter). For the case of the undisturbed images I get the best results with the second derivative in form of a Laplace filter. There are a few different possibilities for the Laplace filter, but the most common one is the following (Jähne 2005):

$$L = \begin{bmatrix} 0 & 1 & 0 \\ 1 & -4 & 1 \\ 0 & 1 & 0 \end{bmatrix} \quad (7.4)$$

The filter is applied to the image by a simple convolution of the image and the filter. For the normalized cross correlation the results significantly increased by applying this Laplace filter to the two images before computing the cross correlation. An example for this is

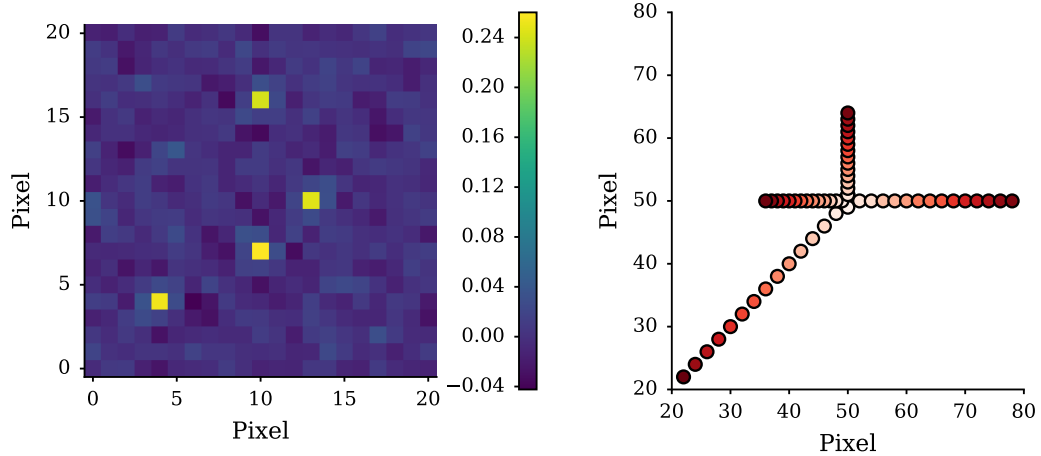


Figure 7.5: Cross correlation of an atmosphere with 4 layers moving with $(2,0)$, $(0,1)$, $(-1,0)$, and $(-2,-2)$ pixels per time step in (x,y) direction. The left image shows one individual cross correlation with a shift of 3 time steps and the right image shows the position of the peaks for 45 time steps. The color coding represents the time with evolving time from white ($t=0$) to dark red ($t=45$).

shown in Figure 7.4. Especially by comparing with Figure 7.3, the improvement gets very clear.

MULTILAYER

Obviously, a one layer atmosphere is a rather unrealistic assumption and the question is whether the cross correlation can detect the shift from a superposition of different atmospheric layers. To test this, I apply the same approach as before with cutting out individual frames from one large phase map. By doing this with different movements into different directions and then adding the frames for each time step, one achieves the effect of an evolving multilayer phase. Using a Laplace filter and the normalized cross correlation as before, the peaks of the different movements were clearly visible in the cross correlation image as shown in the left image of Figure 7.5. In order to detect the different peaks one can fit a two-dimensional Gaussian to the most prominent peak and subtract it. By repeating this to the residual image, all the peaks can be detected, down to a reasonable threshold.

Of course I have only used completely noise-free data here, such that the quality of the multilayer detection will definitely decrease for realistic data. However, with this test one can see that the algorithms work as expected without introducing additional effects. Later tests have to show how good the peak detection works on realistic data.

DETECT SUB-PIXEL SHIFTS

So far I only shifted the phase screens with an integer number of pixels per time step. However, in reality it is crucial that the wind speed can also be detected from shifts which are smaller than one pixel or are not exactly a full number of pixels. The first approach to get the exact shift is to fit a two-dimensional Gaussian to the data. An example for this can be seen in the right image of Figure 7.6. This approach works very good and is pretty solid for different kinds of datasets. The downsides of such a fit are, that the calculation is comparably slow and the fit parameters have to be adapted for each individual case in order to get a really good result.

Roopashree et al. (2013) did an analysis on the peak detection, with special focus on the extraction of the wind speed from the slopes of a SH WFS (see section 7.2). They came to the conclusion that a “3-point Parabolic Interpolant” is the best solution to get the exact shift. In my test, however, this method tends to overestimate the wind speed, which is also mentioned by Roopashree et al. (2013). The reason for the inaccuracy is that the interpolation tends to get imprecise for small shifts. Therefore I finally use their second method, the “3-point Gaussian Interpolant”, as it gives quite good results in our test and is significantly faster than a complete two-dimensional Gaussian fit. The “3-point Gaussian Interpolant” fits a one-dimensional gauss to three pixels, which are the pixel with the maximum value and its two neighbors. By doing this for x and y direction, one can determine the exact peak position.

One point to mention here is that both methods require at least one additional pixel around the one with the position of the maximum in the cross correlation. This means that one needs at least 3x3 (for small shifts) or 4x4 (for larger shifts) pixels in the measurement in order to detect the wind direction. This becomes especially important with focus on the use of WFS slope data in the next section. For the code of wind detection, including the normalized cross correlation and the Gaussian fit see section B.1.

7.2 WIND VECTOR FROM WFS MEASUREMENTS

In reality it is rather inconvenient to use the wavefront itself, as it is not measured from the AO system and has to be reconstructed. This adds additional computational burden and noise, which reduces the performance of the system. Also, a reconstruction is usually not done in the AO system, as the wavefront correction is applied to the DM with the help of an interaction matrix (see section 3.3). Therefore, it is a better solution to directly work on the WFS data to determine the dominant wind vector. At this point, I limit my tests to the most common types of WFS data. These are the slope measurements one gets from a SH WFS or from a pyramid WFS. Another possibility would be to use the curvature data from a curvature WFS. The curvature sensor is already not that common, it is, however, used in the MACAO system at the VLT I which is the reason why I show that the principle also works for this type of WFS. For further analysis, I then focus on slope data.

In principle, one can directly apply the normalized cross correlation to the 2D representation of the WFS data to get the wind velocity. For slope data this is a frequently used technique which was used for example by Schöck and Spillar (1998), Schöck and Spillar (2000), Wilson

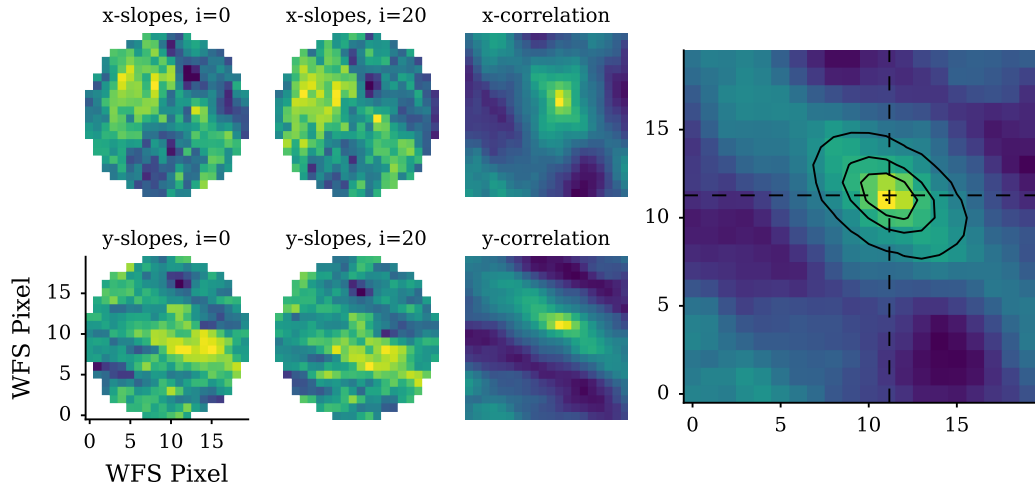


Figure 7.6: Example for the wind vector detection directly from SH WFS slopes. The images in the left two columns show the input slopes (x-slopes on top, y slopes on bottom), with the corresponding normalized cross correlation next to them. The right image then is the average of the two cross correlations with a 2D Gaussian fit to determine the wind velocity. The determined wind velocity is 9.8 m/s at 44°, which is very close to the theoretical value (10 m/s at 45°).

(2002), and Guesalaga et al. (2014). The approach is the same as for the cross correlation with the phase screens, except that one applies the correlation individually for the x and y slopes and calculates the average of the two results. Before doing the cross correlation, one has to do some preprocessing of the data. As the wind velocity is contained in each individual cross correlation with a fixed time difference one can take the average over several cross correlations to reduce the noise and the error of the final measurement. For the simulations I usually used datasets of 20 ms as this is the time scale where one expects TFFH to dominate the turbulence evolution. However, it would also be possible to take longer datasets for the wind measurements and only apply the piston reconstruction to shorter times, as the wind is supposed to be stable over longer time scales. This could be done with a moving average and may be a possibility for real data to further decrease the noise.

For one dataset, one then has to subtract the mean value of the x and y slopes, which is the tip and the tilt of the measurement. The tip and tilt have the most power of all modes and would dominate the cross correlation if they are not subtracted. However, the cross correlation is working better on lower modes and therefore the result increases for tip and tilt reduced data. Furthermore, one has to subtract the time average of each individual pixel over the whole dataset. This is necessary, as static features in the telescope, such as a bias on individual pixels for example from a slightly deformed mirror, would lead to a permanent peak at the zero point of the cross correlation (Schöck and Spillar 1998; Saint-Jacques and Baldwin 2000).

After these preprocessing steps of the slopes, one can apply the normalized cross correlation as given in Equation 7.2. This is done for the x and y slopes individually and the average of

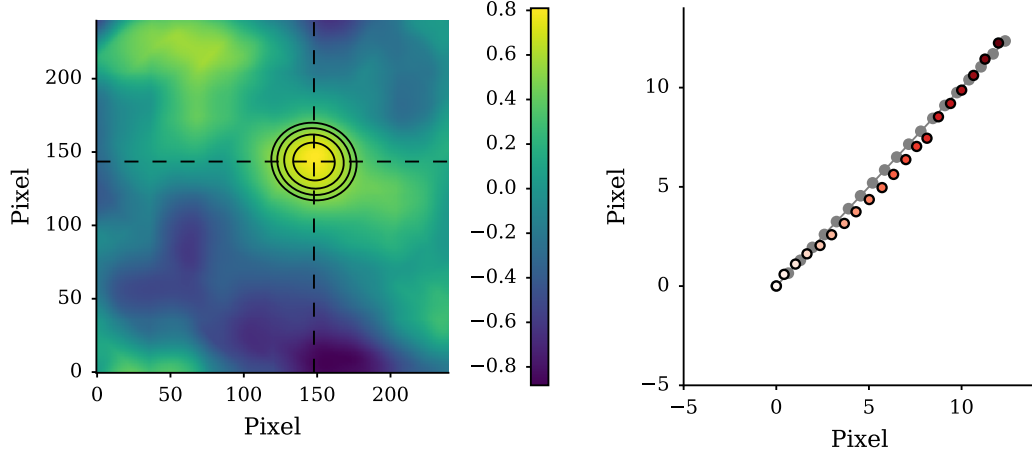


Figure 7.7: Wind detection from a curvature WFS. The left image shows the cross correlation of two time steps with a separation of 15 ms. The peak is detected by fitting a 2D Gaussian (black circles). In the right image the position of the peaks is shown for 20 time steps. The color coding represents the time, with evolving time from white ($t=0$) to dark red ($t=20$). The gray points show the corresponding theoretical values.

the two results is calculated. The peak can then be detected with the sub pixel detection as given in section 7.1. After this, the wind velocity in one direction is calculated with the following formula:

$$v_x = \text{shift}_x \cdot \frac{D}{\#l} \cdot \frac{f}{\#s} \quad (7.5)$$

with the number of lenslets $\#l$, the telescope diameter D and the number of time steps $\#s$ at the used frequency f . This calculation is only valid under the assumption that the wind is in the ground layer. If not, one also has to account for the telescope beam. An example for this procedure is shown in Figure 7.6. The results are reasonably close to the theoretical wind vector for slope data.

CURVATURE DATA

As mentioned earlier, the wind detection also works for data from a curvature WFS. The procedure is the same as for the slope data: The time average of every curvature measurement has to be subtracted and the curvature data has to be mapped to a two-dimensional representation for each time step. From this data, one can then get the wind vector with the same normalized cross correlation as before. As the curvature sensor measures the second derivative of the wavefront, using this data is in principle very similar to the application of a Laplace filter to the actual wavefront. An example for this is shown in Figure 7.7. The results are not as accurate as for the slope data. This could probably be improved by adapting the parameters of the cross correlation and the fit to the curvature data. However, Figure 7.7 shows that the wind measurement from curvature data is possible and already delivers results that are close to the theoretical value. In the following, I only work with

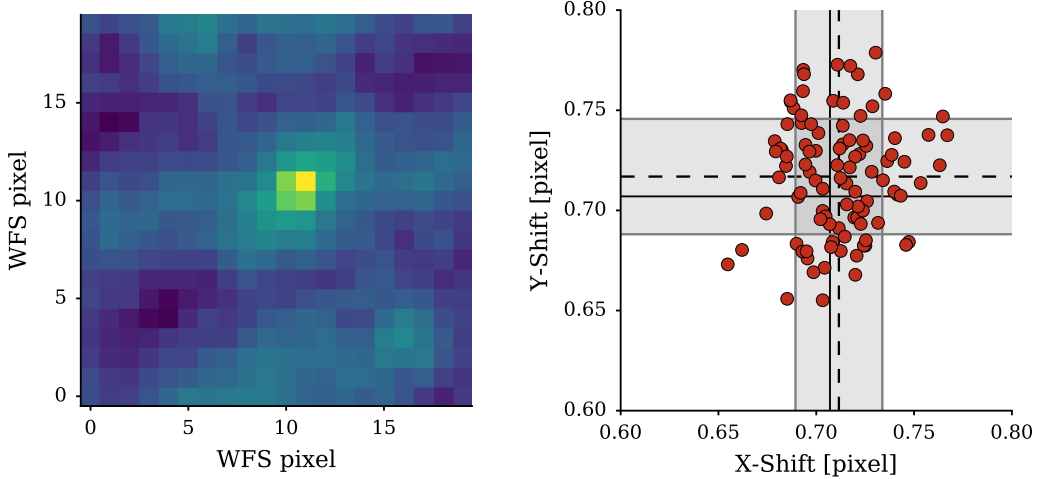


Figure 7.8: Wind measurements for a larger data set. Left: one individual cross correlation. Right: the peak for 100 measurements (red dots). The solid line shows the theoretical value and the dashed line shows the mean of the measurements with the standard deviation in grey.

Shack-Hartmann and pyramid WFS data and therefore I will leave the curvature analysis at that.

ERROR ESTIMATION

There are several possible error sources in these data. Of course there is an uncertainty in the slope measurement which depends on the used WFS, as the pixel spacing of the subapertures and the centroid detection of the spots can vary. Additionally, there is also a certain read-out noise and other noise sources from the detector. However, this is most likely not the dominant error of the wind measurement (Schöck and Spillar 2000). There are more prominent error sources due to the given data and the cross correlation. The main source of error is the very low spatial sampling of the WFS data (Schöck and Spillar 1998). This directly leads to an error in the determination of the wind vector, as the peak position in the cross correlation can only be detected with a certain accuracy. As the finite sampling is not a classical error source and the calculation involves some very nonlinear parts, namely the FFT and the Gaussian fit, a classical error propagation analysis is not helpful here. I rather decided to use statistics and the Gaussian fit to estimate the uncertainty. For an individual cross correlation as shown in Figure 7.6, the uncertainty of the peak position measurement is around a tenth of a pixel. The fitted Gaussian has a FWHM of usually slightly larger than one pixel.

Furthermore, I use a larger dataset to calculate the wind vector for 100 individual measurements at stable wind velocity (see Figure 7.8). In the figure, one can see that the measurement is pretty stable with a standard deviation of 0.06 pixel for a fairly usual setup ($D=8\text{m}$, 20 lenslets per diameter, $v=10\text{m/s}$, $\Delta t=20\text{ms}$). This leads to a relative error in the

peak position and therefore also in the wind velocity of 10%. One can also see from this figure that the error can further be decreased by averaging the wind over a larger time scale.

However, this is only the uncertainty of the measurement for a single layer of the atmosphere. If one takes into account all the involved atmospheric effects such as boiling and a multilayer atmosphere, one will come to larger errors in the measurement. As especially the boiling is very hard to predict, it is difficult to make an appropriate prediction for the error of the measurement here. As mentioned earlier, I try to estimate the limiting effect of boiling by applying the method to real data in the last part of this work.

FIRST RESULTS

8

In this chapter, I show the first results of the piston reconstruction with simulated data. For this purpose I start with comparing the two possible algorithms for a very simple AO system. I then test the algorithm for different set-ups, as they are in use at the VLTI and LBT, in order to see, which AO systems are usable for P-REx. All the simulations in this chapter are done with a single layer atmosphere. A multilayer analysis follows in the next chapter.

8.1 COMPARING THE TWO ALGORITHMS

In order to get the necessary data from the simulations, I created a work flow from the YAO simulation, which is shown in Figure 8.1: The inputs for the simulations are the atmospheric phase screen and a parameter file (.par file), which lists the properties of the simulated telescope and AO system. For the calculation of the theoretical piston, I directly save the screen, which YAO sends to the WFS. These data are used to get the theoretical piston and the tip and tilt values, in order to analyze the results of the P-REx algorithms. In the same way the slope data from the WFS and the voltages from the DM are saved. With these data one can reconstruct the POL data, as shown in Equation 5.1. From POL slopes one can measure the wind velocity and extract the tip and tilt values. In case of the *P-Rex wavefront algorithm* a further step is necessary. As in this case the actual wavefront is needed, a reconstructor is used to calculate the POL phase from the slope data. The reconstructor converts the measured WFS slopes into Zernike modes and then builds the wavefront as a summation of the Zernike images. The reconstruction with Zernike polynomials is a typical approach for wavefront reconstruction. For more information on both, the Zernike polynomials and the reconstructor see Appendix A.

With this work flow, I gather all the data I need for the piston reconstruction: the wind velocity is determined by a cross correlation of the POL slopes (as discussed in chapter 7) and can then be used to calculate the differential piston, either with the overlapping area from the phase screens (*P-Rex wavefront algorithm*) or with the tip and tilt values from the slopes (*P-Rex Tip-Tilt algorithm*).

The first step in the analysis is now to determine the principal performance of the two algorithms. For these first tests I use a rather good, well-resolving AO system, with a 20x20 SH WFS. By doing this I ensure that the results are not limited by the properties of the system, as for example the number of actuators. The main properties of the used AO system are listed in Table 8.1.

At this point it is necessary to quantify the performance of the piston reconstruction by each algorithm. In order to do so, I extract the actual piston value from the used phase

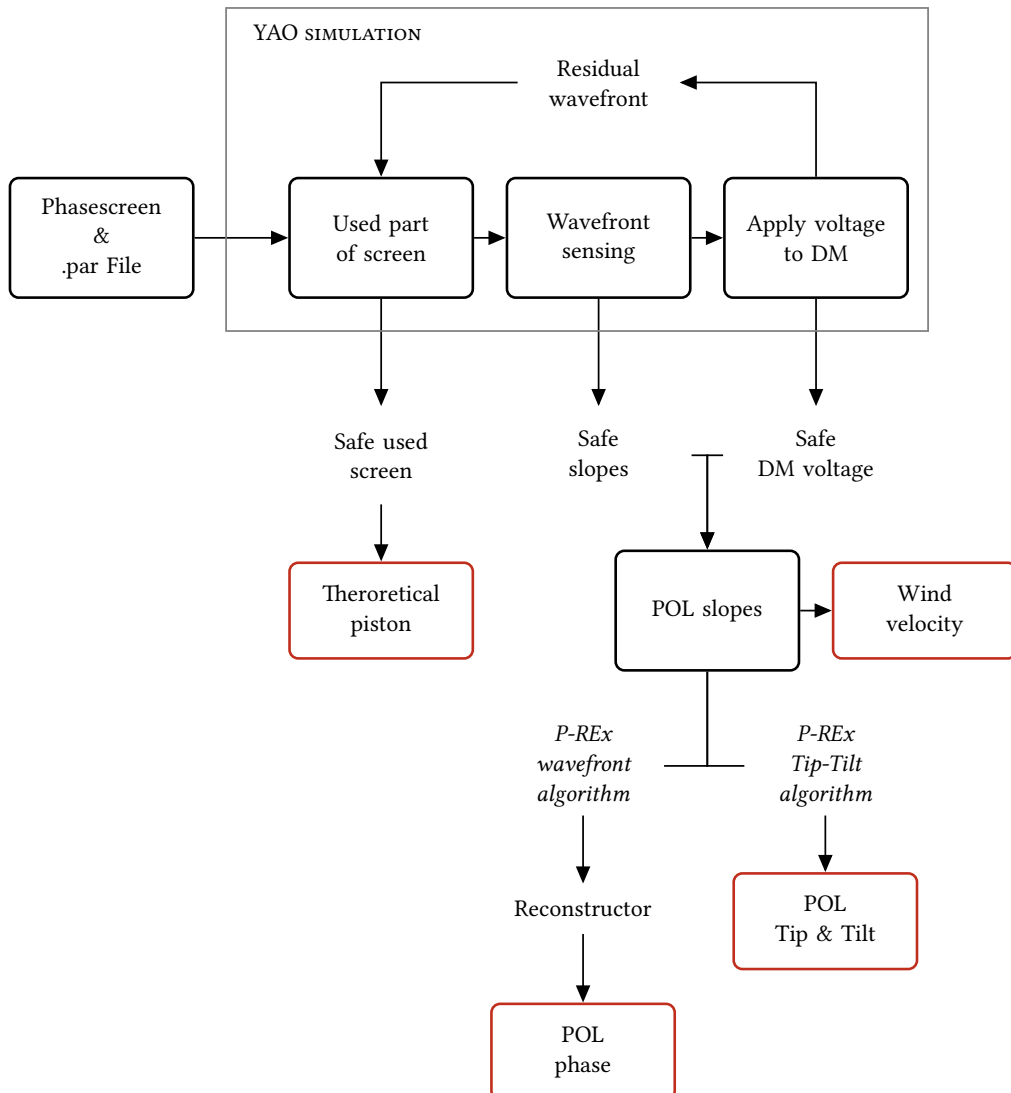


Figure 8.1: Typical workflow of a YAO simulation, to get all the necessary data for the P-REx algorithm. The calculations in the grey box are done by the YAO simulation, while arrows in/out of the box indicate in and output data. The red boxes show the data required for the P-REx test, which are the wind velocity and the tip-tilt values for the *P-Rex Tip-Tilt algorithm* and the wind velocity and the POL slopes for the *P-Rex wavefront algorithm*. In both cases the theoretical values are calculated from the used phase screens.

Keyword	Value
Telescope diameter	8 m
D/r ₀	40
Wind velocity	20 m s ⁻¹
Wavelength	650 nm
Guide star luminosity	-5 mag
WFS type	Shack Hartmann
Number of WFS lenslets	20 x 20
Number of DM actuators	20 x 20
Frequency	500 Hz

Table 8.1: Properties of the AO system for general tests.

screens (see Figure 8.1) and subtract the initial value, as both algorithms only detect the shift in piston and not the actual piston values:

$$P_{\text{theo}}(t) = P_{\text{screen}}(t) - P_{\text{screen}}(0) \quad (8.1)$$

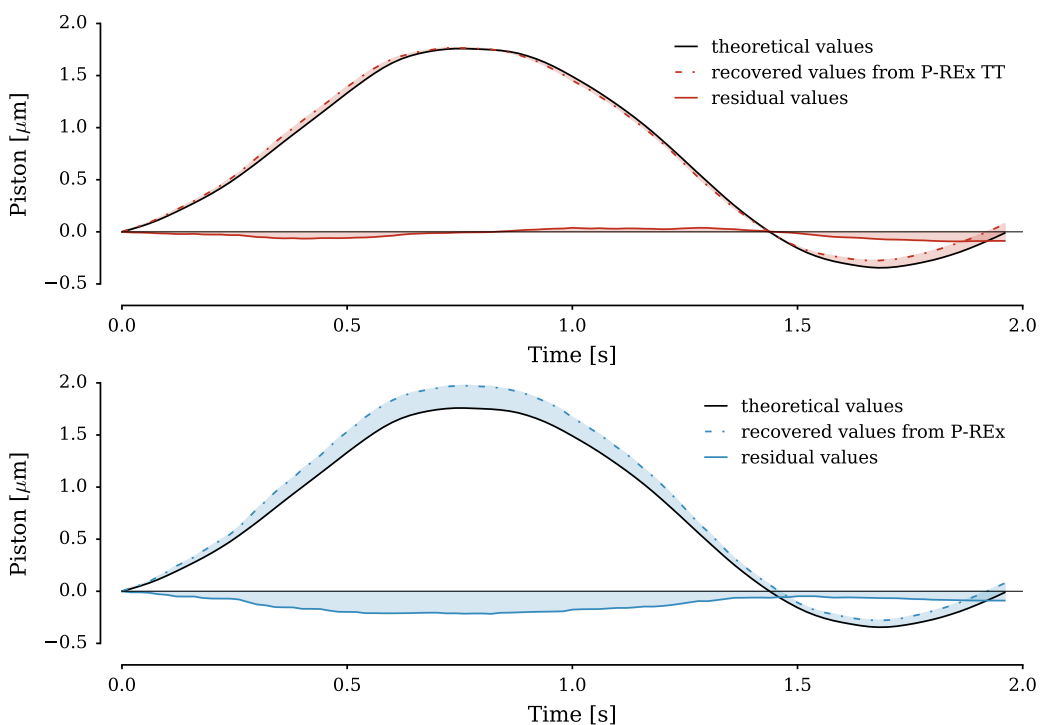
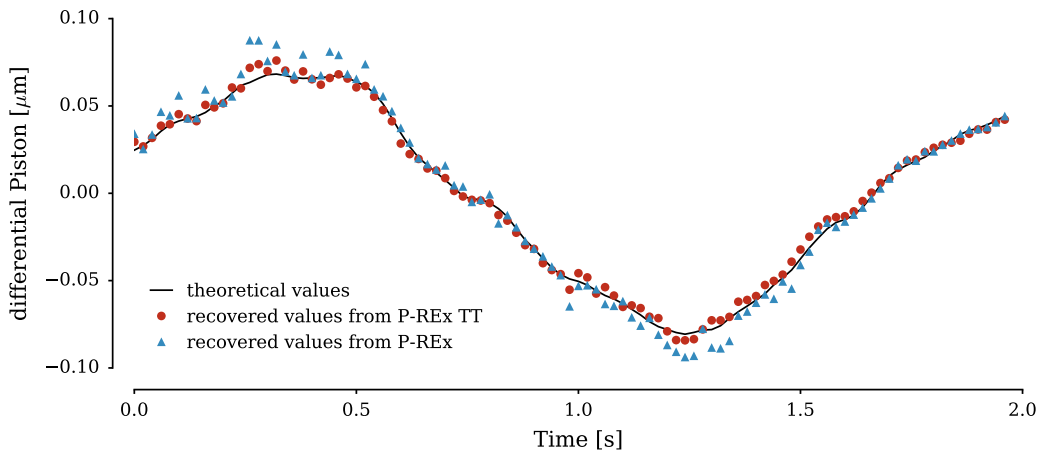
With the data from an AO system as given in Table 8.1, I now show the first tests of the *P-Rex algorithm* and the *P-Rex Tip-Tilt algorithm*, which both give the differential piston over the time as an output. The theoretical differential piston can be calculated by just subtracting the piston of the previous time step from the current one. An example of how the differential piston for the two algorithms looks like is shown in Figure 8.2. One can directly see that the recovered differential piston from the P-REx algorithms fits quite well to the theoretical values, although the *P-Rex Tip-Tilt algorithm* seems to work slightly better than the *P-Rex wavefront algorithm*. In order to better quantify these first results, the calculated differential piston is then used to reconstruct the actual piston over two seconds. This is done by simply adding up all the differential piston values:

$$P_{\text{P-REx}}(T) = \sum_{i=0}^T dP_{\text{P-REx}}(t = i) \quad (8.2)$$

This reconstructed piston can directly be compared with the theoretical piston from Equation 8.1. An example for the reconstructed piston from the two algorithm is given in Figure 8.3, which uses the same data as Figure 8.2. These first results clearly show that the piston evolution can be recovered by both of the two algorithms.

For the further discussion it is helpful to set up a value in order to quantify the quality of the result from the piston reconstruction. To do so, I calculate the root-mean-square of the difference between the reconstruction and the theoretical value. This is from now on declared as the root-mean-square error (RMSE):

$$\text{RMSE} = \sqrt{\frac{1}{n} \sum_{t=1}^n [P_{\text{theo}}(t) - P_{\text{P-REx}}(t)]^2} \quad (8.3)$$



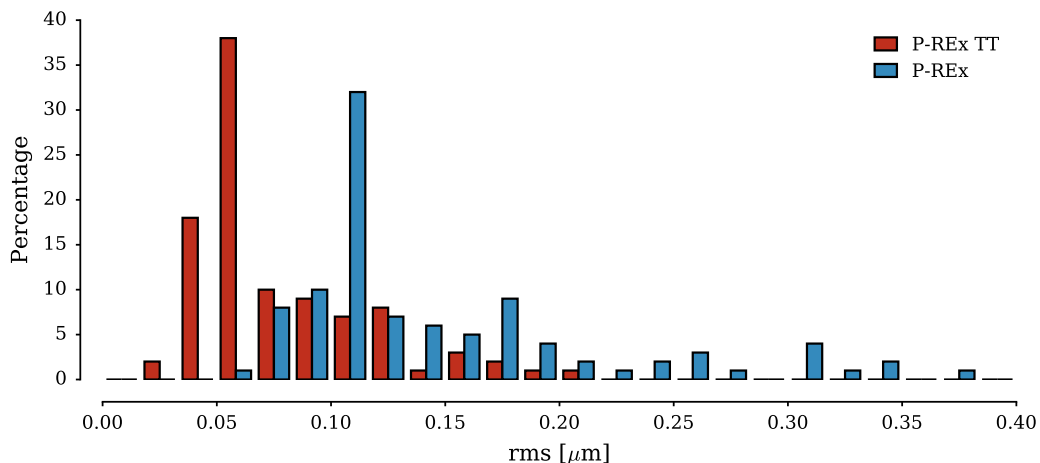


Figure 8.4: Histogram of the error of 100 runs of the P-REx wavefront (blue) and the P-REx Tip-Tilt algorithms. Each run was done with a different phase screen and a random wind direction.

This is somehow an arbitrary definition for the error of the measurement, as the piston values from the reconstruction are calculated by the summation of the differential piston. This means that every error of the reconstruction also gets summed up, which will ultimately lead to an increasing error. The RMSE therefore increases with increasing time. In order to still get uniform results, I always take the RMSE from a reconstruction over two seconds. This is the timespan over which I expect the algorithm to work and an upper limit for the time over which it should give good results, in order to work in combination with a low frequency fringe tracking system. Therefore, the error definition is chosen in order to match the requirements of such a system.

The results of the piston reconstruction slightly depend on the actual used atmosphere for the simulation, as well as on the wind direction. In order to quantify the quality of the two algorithms, I ran both algorithms for 100 times with the same AO system but with a different phase screen for each run and a random wind direction. The wind velocity was set to 20 m s^{-1} , which is a little higher than expected for the ground layer. By choosing this value, one ensures that the shift is large enough to be detected. However, for the assumption of a perfectly valid TFFH this does not limit the generality as a smaller wind shift could be detected up to the same accuracy with a higher average time. The individual RMSE from these 100 runs are shown in a histogram in Figure 8.4. From the histogram one can directly conclude that both algorithms deliver pretty good results in the most cases and that both algorithms are comparable. But the P-REx wavefront algorithm seems to deliver worse results, which is also visible in Figure 8.2 and Figure 8.3. This is on first sight surprising, as the tip tilt algorithm is only an approximation and the full wavefront algorithm should therefore be the more accurate method. However, the larger error comes from the reconstruction of the wavefront. The reconstructed wavefront is based on a modal approach with Zernike polynomials in which each individual wavefront is the summation of 100 Zernike modes (see Appendix A). An example for such a Zernike reconstruction is shown in Figure 8.5. From this figure one can conclude that the reconstruction does

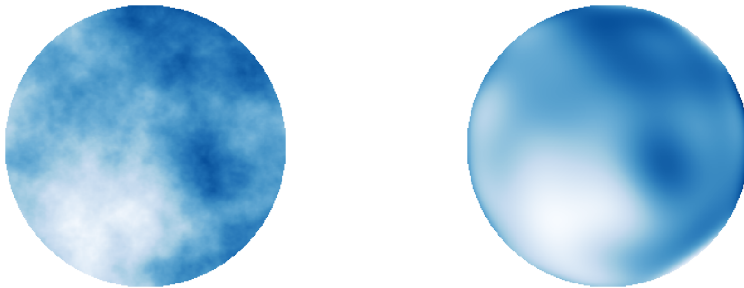


Figure 8.5: Example of the wavefront reconstruction with Zernike Polynomials. The real wavefront is shown in the left image and the reconstructed one in the right.

only represent the wavefront to a certain degree, as especially the smaller scale structure is mostly lost in the reconstruction. This could be improved by a higher number of modes, but that would heavily increase the computation time. One could also use another reconstructor, which would probably improve the result (Dai 1996; Wang et al. 2011). However, the quality of the reconstruction will probably be even worse in a real case, as I have used a full circular aperture so far. In reality one would have to deal with additional effects such as the shadows from spiders and the secondary mirror, which would slow down the reconstruction and decrease the quality. Taking this into account and the fact that the *P-REx Tip-Tilt algorithm* delivers very good result and additionally has advantages in computation time, I will not further focus on possible improvements in the reconstruction, but focus on the tip tilt method.

As mentioned earlier, the *P-REx Tip-Tilt algorithm* has some advantages concerning the necessary computational time over the *P-REx wavefront algorithm*. The tests showed that the Tip-Tilt algorithm is about 10 times faster, which is mainly due to the very slow reconstruction of the wavefront. This could definitely be improved, as I have not put any effort into reducing the computation time. However, as the tip-tilt algorithm gives better results, this is not necessary. Therefore, from here on I stick to the *P-REx Tip-Tilt algorithm* and do all the further work with this faster and more accurate concept.

8.2 ERROR CONSIDERATIONS

For the previous tests an AO system was used, which is working very good in order to test the algorithm under ideal conditions. However, there are several aspects which could possibly decrease the quality of the piston reconstruction. For example the number of WFS lenslets and DM actuators was set to a comparably high value, in order to get a good spatial sampling. But there are a lot of AO systems with a much lower sampling. Other properties which could possibly play a role are the brightness of the guide star, the amount of turbulence in the atmosphere, usually represented by the value of D/r_0 , the wind speed, or the used time average. In the following, I present how the results of the reconstruction change when one varies these parameters.

	optical 0.5 μm	NIR 2.0 μm	MIR 10.0 μm
2λ	0.71 μm	2.83 μm	14.1 μm
$\lambda/4$	0.08 μm	0.35 μm	1.77 μm
$\lambda/10$	0.04 μm	0.14 μm	0.70 μm

Table 8.2: Uncertainty ranges for the piston reconstruction in different wavelengths.

One parameter which has no direct importance on the piston reconstruction is the wavelength. Simulations have shown that the piston reconstruction stays exactly the same for different wavelengths. However, the actual used wavelength has a large impact on the interpretation of the results. This is due to the fact that the piston and with that the difference between the reconstruction and the actual value is given in μm . However, the fringe contrast in an optical interferometer relies on the difference in phases between the two combined light beams and can be expressed in wavelengths. The change in fringe contrast due to the piston difference between the two telescopes is therefore not independent of the wavelength (see chapter 3). This means, in other words, that for smaller wavelengths the piston error has to be smaller than for larger wavelengths, as it can only be a fraction of the used wavelength. However, one has to remark at this point that the here used wavelength is the scientific wavelength at which the observation is done. This science wavelength does not have to be the same as the AO wavelength, as the AO sensing and the observation can be done at different wavelengths. Therefore, the P-REx limits have to be applied to the science wavelength, although the data is taken at the AO wavelength.

In Table 8.2 three different error regimes for three different wavelengths (optical, near-infrared (NIR), and mid-infrared (MIR)) are summarized. The three error regimes are twice the wavelength below which the fringes become visible, a quarter of the wavelength where one starts to see stable fringes and a tenth of the wavelength where the fringe contrast stays perfectly stable. As these regimes apply for the combined signal from two telescopes, there is an additional factor of $\sqrt{2}$, as the piston reconstruction is analyzed for one single telescope here.

However, it is not very helpful to have nine different cases to analyze. In order to avoid this, the error budget can be summarized in four general cases:

- $\Delta P < 0.05 \mu\text{m}$: Piston reconstruction works for all wavelengths
- $\Delta P \approx 0.12 \mu\text{m}$: works very good in the infrared and fairly well in the optical
- $\Delta P \approx 0.4 \mu\text{m}$: works very good in the MIR, not usable in the optical
- $\Delta P > 2.0 \mu\text{m}$: could still work for MIR, not usable for shorter wavelengths

With this scale one can now determine the performance of the P-REx algorithm under different conditions. This will again be applied on the RMSE over two seconds, as this is the time range where the algorithm should be able to work alone, without the additional

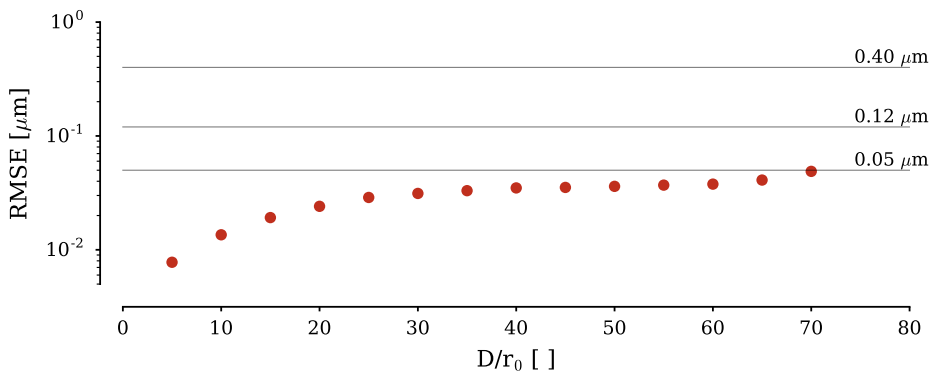


Figure 8.6: Dependency of the piston reconstruction on the atmospheric turbulence, given as D/r_0 . The gray lines show the error ranges defined in the text.

fringe tracker. However, I mostly use only the first three cases, as a piston difference larger than $2\text{ }\mu\text{m}$ over two seconds basically means that the reconstruction is not usable.

In the following I discuss the performance for different systems. This will first be by just varying certain parameters and then afterwards by applying the results to actual existing AO systems. All the simulations here are still under the assumption of a single layer atmosphere, as the more realistic multilayer atmosphere is discussed in the next section. The parameters of the AO system that are not varying are the ones given in Table 8.1.

ATMOSPHERE

The first test has the goal to see how the results of the piston reconstruction depend on the amount of turbulence in the atmosphere. In order to test this, I vary the Fried parameter in the simulation, ranging from 1.6 m ($D/r_0 = 5$) to 10 cm ($D/r_0 = 80$). The results are shown in Figure 8.6. The main behavior, visible in the figure, is that the results decrease with increasing D/r_0 , or decreasing r_0 . This is the expected result and can be explained by the fact that YAO uses the same phase screen for all simulations and just multiplies it with a weighting factor, in order to match the strength of the turbulence with the used r_0 . As the Fried parameter is defined as the diameter of a circle within which the variance of the wavefront aberration is equal to 1 rad^2 (see section 2.2), the atmosphere can be adapted to a different r_0 by a constant factor.

Therefore, the simulations used for Figure 8.6 only differ in a weighting factor for the turbulence: a larger r_0 means lower turbulence and a smaller r_0 means higher turbulence. With this in mind, one can see that for example a small error in the wind measurement introduces a larger error for a small r_0 and results in a larger overall RMSE. The increasing RMSE with larger turbulence is therefore expected, since the phase residuals for more turbulent phase screens with a fixed wind speed are larger. What one can still take from this is that P-REx delivers good results in the expected turbulence range for good and medium seeing (D/r_0 between 30 and 70, see 2.1). Nevertheless, these results are nearly

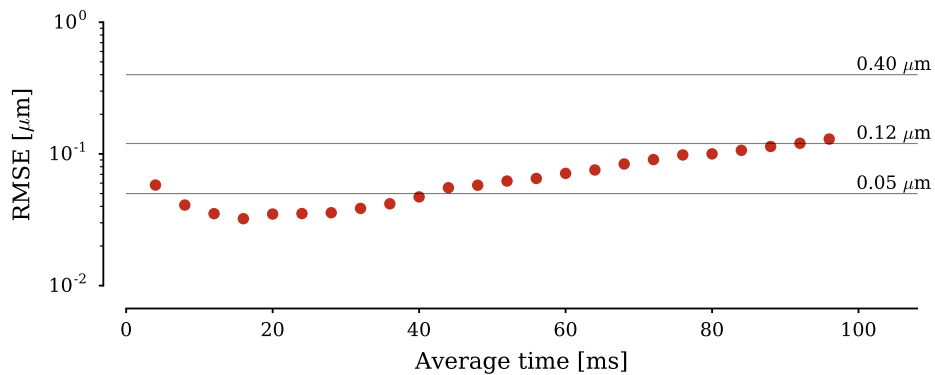


Figure 8.7: Dependency of piston reconstruction on the time over which the average of the cross correlation is taken. The gray lines indicate the three error regimes as discussed in the text.

independent of the strength of the turbulence. The actual D/r_0 at the telescope should therefore not be a critical factor for P-REx.

WIND SPEED & TIME AVERAGE

In order to find the correct parameters for the piston reconstruction, it is important to find the ideal average time for the wind measurement. Figure 8.7 shows the result of the piston reconstruction for a varying average time. There are two different trends in the figure: For very short time scales, the atmosphere shift due to the wind is so small that it is barely detectable with the cross correlation technique. Therefore, the values increase with increasing average time. However, for larger average time, the piston movement gets under sampled as the average time is larger than the timescales of the piston evolution. For real data, the error for larger average times is probably even larger as boiling effects get more important. From Figure 8.7 it is visible that there is an ideal average time where the piston evolution is sampled well and the wind detection works good. For the wind velocity of 20 m s^{-1} this value lies around 20 ms.

However, for smaller wind velocities the average time for the wind measurement has to be increased, in order to clearly detect the shift of the atmosphere. As this would most likely include a bad sampling for the piston evolution, the solution can be to measure the wind velocity over a longer time with a moving average and use a higher sampling for the piston reconstruction.

A moving average takes the average over the last N measurements:

$$\bar{v}_{\text{MA}}(t) = \frac{1}{N} \sum_{i=0}^{N-1} v(t-i) \quad (8.4)$$

In this case $v(t)$ is the wind velocity at a certain measurement point t. For the piston reconstruction, the moving average is used in a special way: The wind measurement is

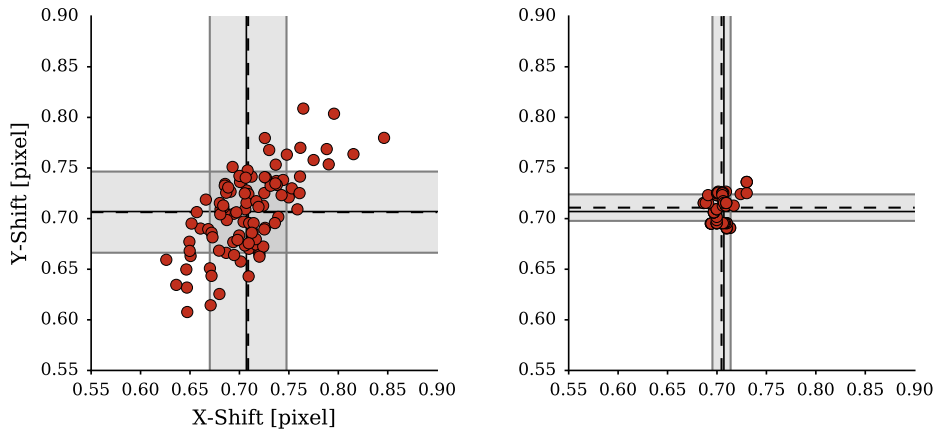


Figure 8.8: Comparison of the wind determination with the usual average (left) and a moving average (right). The usual average is taken over 20 ms and the moving average over 0.5 s. The solid lines show the theoretical values and the dotted lines show the mean of the measurements with the standard deviation in grey.

still taken at the sampling which is also used for the piston reconstruction. This is usually 20 ms. These measurements are then taken for the moving average. Figure 8.8 shows an example for a wind velocity measurement with and without moving average. In this case the moving average is used over 25 measurements of 20 ms each, which makes it an effective average over 0.5 s. The figure clearly shows that this method can significantly improve the wind measurement. Furthermore, it is given from the theory that the wind vector should be stable over such timescales. The best way for P-REx would therefore be to calculate the moving average to detect the wind velocity and to use these values to apply the piston reconstruction with a frequency of around 100 Hz. In order to stay consistent, I stick with the usual wind vector determination for now and use the moving average in the next chapter for the realistic atmosphere and AO systems.

GUIDE STAR MAGNITUDES

Another important parameter is the brightness of the used guide star. The question behind this is whether P-REx has higher requirements on this value than the AO system. The results from the simulations with changing guide star magnitudes are shown in Figure 8.9. What becomes very clear is that the piston reconstruction works very stable for a decreasing guide star luminosity, as long as the AO system is working properly. As soon as the luminosity decreases so much that the performance AO system suffers, the piston reconstruction fails too. The performance of the AO system is shown in the figure by the strehl values. The behavior of the piston reconstruction is understandable as it depends on the WFS measurements and if they contain an increasing error, the piston reconstruction will do so too. The important point here is that P-REx is limited by the AO systems, which means that one does not have to add new requirements to the measurement: As long as the AO system works properly, P-REx does so too.

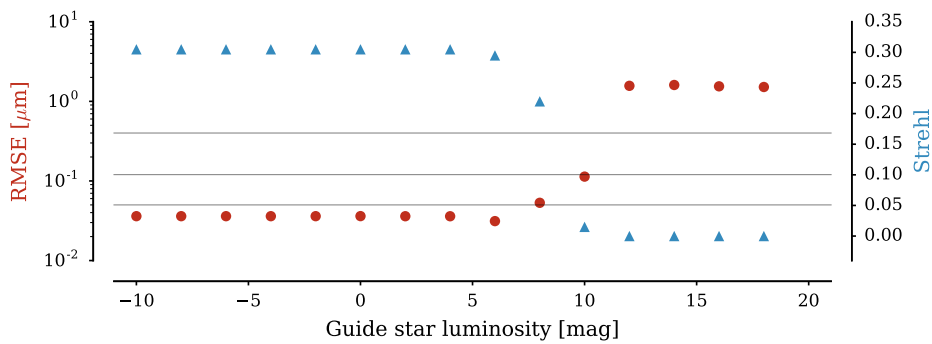


Figure 8.9: Dependency of the piston reconstruction on the guide star luminosity. The red dots show the RMSE for each luminosity (left axis) and the blue triangles show the corresponding strehl of the AO system (right axis). The gray lines indicate the three error regimes as discussed in the text.

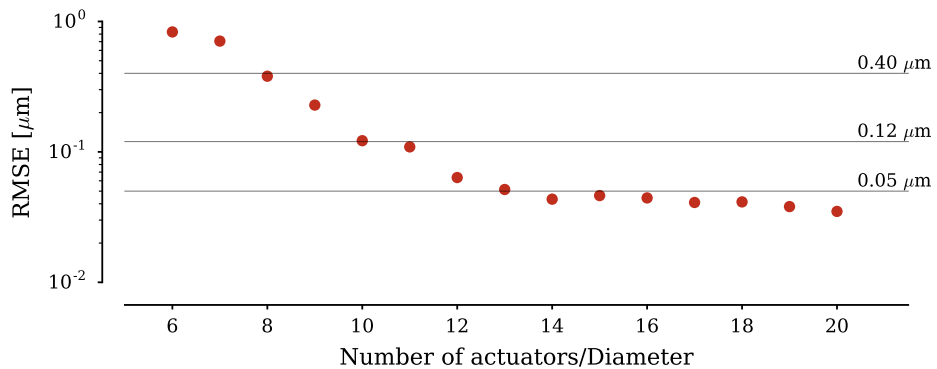


Figure 8.10: Dependency of the piston reconstruction on the spatial sampling. The plot shows the RMSE dependent on the number of WFS measurements in one telescope diameter. The gray lines indicate the three error regimes as discussed in the text.

The simulations for Figure 8.9 were done with a natural guide star, but the result is the same for the use of laser guide stars.

Spatial Sampling

In principle, one has to consider the spatial sampling of the WFS, as well as of the DM. However, as I am only working with the data in the WFS domain, I only consider the spatial sampling of the WFS. As long as the sampling of the DM and the WFS are similar, which is usually the case, this approach induces no additional error.

The spatial sampling of the WFS has two different effects on the results of the P-REx algorithm. The first one is simply that a higher number of sensors allow a more accurate measurement of the wind velocity. This is also based on the result that the error of the

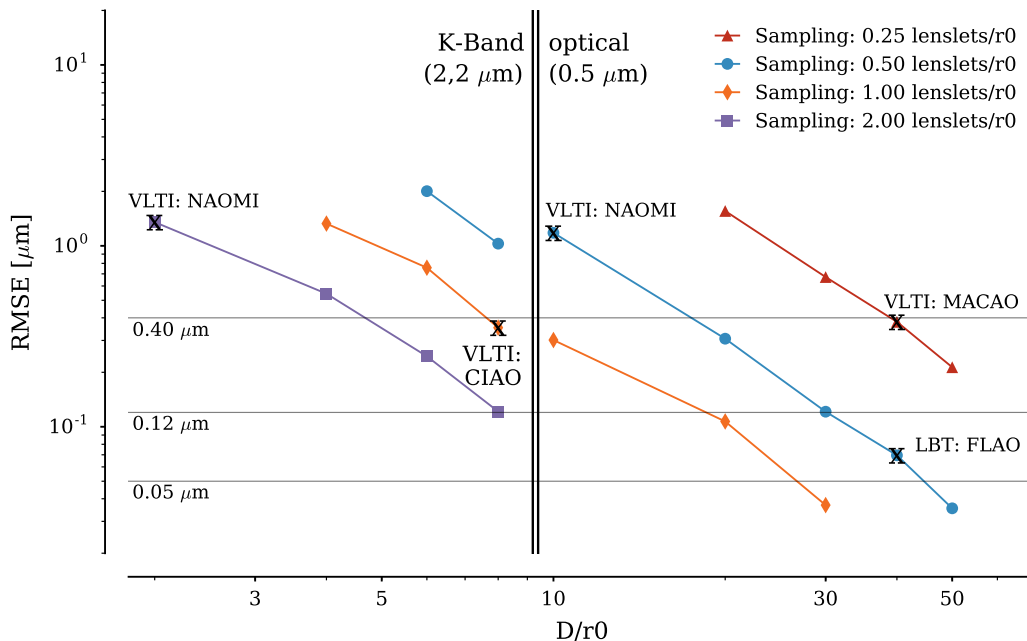


Figure 8.11: P-REx performance for a varying D/r_0 and different samplings of the WFS. The plot shows results in the K-Band (left part) and in the optical (right part). The different samplings per r_0 are shown in different colors, as indicated in the legend. The gray lines are the same error regimes as before.

wind detection scales with the size of the WFS lenslets (section 7.2). The second effect is that the strength of the turbulence scales with r_0 . Therefore, one could also test how good the WFS sampling per r_0 has to be for a working system. But as both effects tend into the same direction (more measurements mean a better result), it is at this point not really important which effect dominates. This is however only the case as long as the sampling is not unreasonable high. A very high sampling per r_0 would not increase the performance, as the wavefront aberrations would be oversampled. This should not be a problem, as the AO systems are always dimensioned with respect to the r_0 at the telescope site and therefore a reasonable sampling is assured.

Figure 8.10 shows the expected behavior: With an increasing number of measurements per diameter the error of the piston reconstruction decreases. From a value of ten WFS measurements in the telescope diameter (meaning a 10×10 WFS), the values show that a piston reconstruction can be usable. This means that the AO systems at the VLTI UTs and at the LBT (CIAO/MACAO at the VLTI and FLAO at the LBT, see Table 3.1) are possible candidates for the piston reconstruction with P-REx. Especially the LBT FLAO should deliver good results, as the pyramid sensor has a WFS resolution of 30×30 measurements in the highest binning mode.

PERFORMANCE FOR EXISTING SCAO SYSTEMS

With the previous findings one can test the results of the piston reconstruction for simulations of different set-ups of AO systems. This is done in order to test which of the existing AO systems (see Table 3.1) is usable for P-REx. The results are shown in Figure 8.11, where the error of the piston reconstruction is shown as a function of D/r_0 . For the plot a good seeing of $0.5''$ was used, which corresponds to a value for r_0 of 20 cm in the optical and 1 m in the K-Band. The NAOMI system from VLTI is shown in both wavelengths, as it works at a wavelength of $1.65\text{ }\mu\text{m}$, which puts it in between the shown wavelengths. All the results in this plot are the average from three runs with different phase screens, in order to avoid an influence of a specific phase screen.

The very first result from this plot is that P-REx is not able to deliver good results for the 2 m telescopes (ATs) of the VLTI. The results are only in the order of $1\text{ }\mu\text{m}$. This is mainly due to the very low sampling of the NAOMI WFS, which use an array of 4×4 lenses. As discussed earlier, this is barely enough to detect the atmospheric motion and therefore the results from the wind velocity measurement have a large error. In the near future, NAOMI will be the best AO system for the ATs and with this system P-REx cannot be considered usable. Due to this I now focus on the 8 m class telescopes.

For the UTs at the VLTI there are currently two AO systems with a similar sampling of 9 and 10 WFS measurements in one telescope diameter. This is the CIAO system in the NIR with a 9×9 SH WFS and the MACAO system with a 60 element curvature WFS. Both systems deliver P-REx results in the order of $0.3\text{ }\mu\text{m}$. These results are therefore in the regime where P-REx is usable in the NIR and works very well in the MIR. The last available system is the FLAO system at the LBT. With a maximum sampling of 30×30 for the pyramid sensor, this system has the best preconditions for the use of P-REx, which is also shown in the simulation. With RMSE values of around $0.06\text{ }\mu\text{m}$, P-REx should work very well in the NIR and should also deliver good results in the optical. The LBT FLAO point in Figure 8.11 is furthermore only for a medium binning of 20×20 . The RMSE decreases significantly for the maximum binning of 30×30 .

Up to here, the simulations show no critical elements for the piston reconstruction. The key results till now are the following:

- As long as the AO system delivers good results, the AO data are good for P-REx.
- In terms of atmospheric conditions (wind velocity, r_0), P-REx simulations show good results for all reasonable conditions.
- As the sampling of the AO system at the 2 m VLTI ATs is very low, P-REx should work best for telescopes of the 8 m class.
- The most promising system is the LBT FLAO, as it offers the highest WFS sampling.

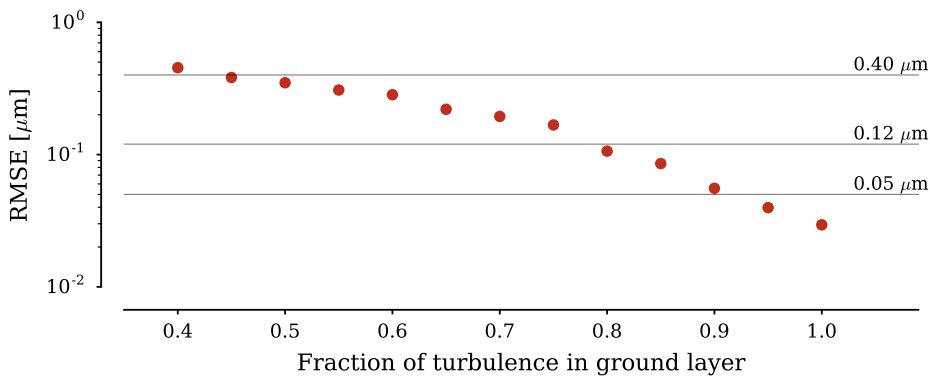


Figure 8.12: Dependency of the piston reconstruction on the fraction of turbulence in the ground layer. The gray lines show the same error regimes as before.

8.3 SINGLE AND MULTILAYER ATMOSPHERE

The one main feature that I have neglected until now is the multilayer movement of the atmosphere. Figure 8.12 shows the development of the RMSE with an increasing fraction of turbulence in the ground layer. The fraction of the turbulence which is not in the ground layer is in two higher layers at 2 km and 4 km height, which are moving with the same speed as the ground layer, but with an angle of plus and minus twenty degrees with respect to the ground layer. What one can directly see is that the error of P-REx is increasing with a decreasing fraction of turbulence in the ground layer. This is expected, as the correlation only detects the wind peak of the dominant ground layer and the upper layers act as an additional source of noise.

However, it is hard to quantify the impact of the multilayer atmosphere from such a simulation. For now I conclude that a multilayer simulation increases the error in the piston reconstruction. A better conclusion follows in the next chapter from simulations with a realistic multilayer atmosphere.

This last chapter of the simulations part focuses on two different things. Firstly, I now test the results from P-REx for a realistic multilayer atmosphere. Secondly, the performance of the piston reconstruction is shown not only for a single-conjugated, but also for a ground layer AO system. This is introduced in this part, as the simulation of a multilayer atmosphere make it possible to detect the separate layers with layer-oriented AO systems. This chapter ends with an outlook on the use of P-REx for a multi-conjugated AO system and a short conclusion of the results from the simulations.

9.1 SINGLE-CONJUGATED ADAPTIVE OPTICS

For the first simulations a SCAO system with a realistic multilayer atmosphere is used. The parameters of this atmosphere are the ones that are outlined in section 2.3 and are summarized in Table 2.2. The used atmosphere consists of nine different layers which group together into three main layers. The first one is the dominant ground layer (0 to 1 km altitude), which contains around 65 % of the turbulence. The other two layers are the medium layer (1 to 5 km altitude) with slow wind speeds and the high layer (5 to 15 km altitude) with fast jet-stream winds. For the simulations the AO system from Table 8.1 is used again. It produced good results for all the previous tests and is, except for the type of WFS, very similar to the FLAO system at LBT.

The results of the piston reconstruction from the multilayer simulation are shown in Figure 9.1. In this case, the figure does not show the reconstructed piston as before, but the differential piston as one gets it from the calculation before the summation from Equation 8.2. The differential piston is the actual result from P-REx and by using it here, it is easier to compare the different systems. The multilayer atmosphere effects the results of P-REx in two different ways: Firstly, it reduces the accuracy of the wind velocity measurement. This becomes clear by looking at the measured values. The wind velocity from the multilayer simulation is $(9.28 \pm 1.59) \text{ m s}^{-1}$, while the theoretical wind velocity of the ground layer is 10 m s^{-1} . A single layer atmosphere with the same phase screen as used for the ground layer gives a wind velocity of $(9.42 \pm 0.82) \text{ m s}^{-1}$. This shows that the error of the multilayer wind measurement is twice as big as the error of the single layer measurement. This is simply due to the other layers that act as an additional noise source in the cross correlation. In principle, it is possible to detect different layers, as discussed in chapter 7. However, for this to work one needs a big separation of the different cross correlation peaks. This could be possible, for example when two dominant layers move in the opposite direction. For the atmosphere used here, with nine layers moving in similar direction, a multilayer detection is not possible.

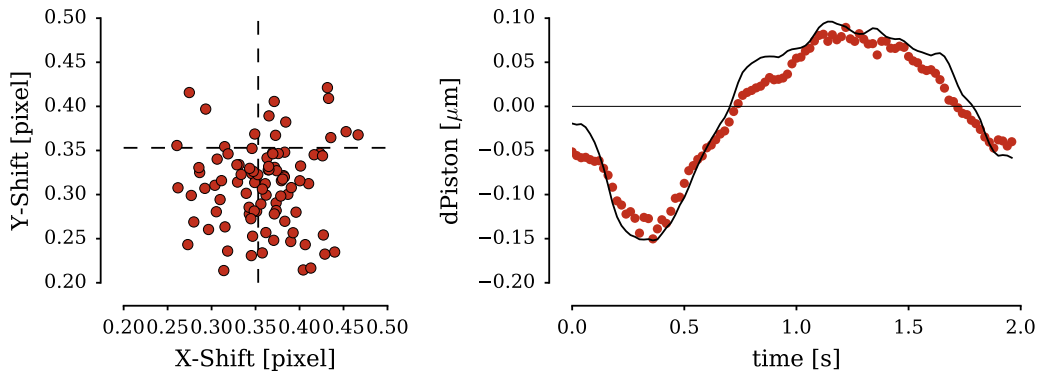


Figure 9.1: P-REx performance for a SCAO system with a multilayer atmosphere. The left image shows the detected wind speeds as red dots, with the theoretical speed of the ground layer shown by the dashed cross. The right image shows the reconstructed differential piston as red dots with the theoretical values as a black line. The RMSE from this simulation is $0.506 \mu\text{m}$ (see Table 9.1).

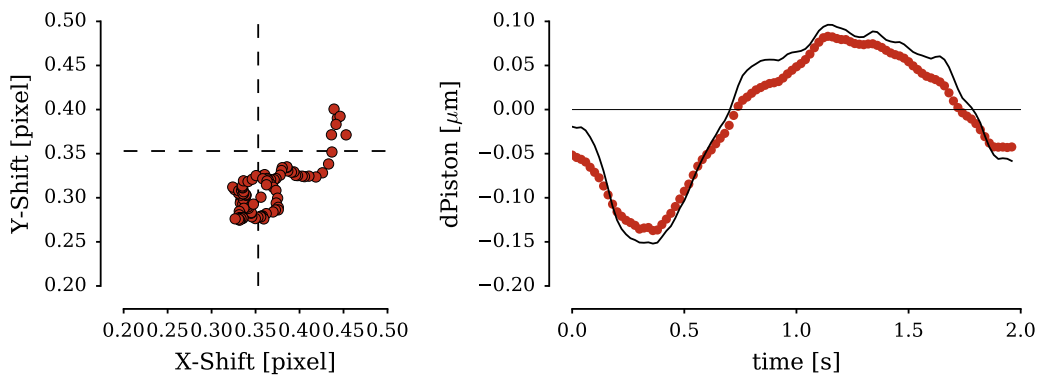


Figure 9.2: Same plots as in Figure 9.1 but this time a moving average is used for the cross correlation, in order to improve the wind vector measurement. In this case the RMSE is $0.426 \mu\text{m}$.

AO system	Single or multilayer	Moving average	Wind measurement	RMSE
			m s^{-1}	
SCAO	single	✗	9.42 ± 0.82	0.087
	single	✓	9.56 ± 0.45	0.066
	multi	✗	9.28 ± 1.59	0.506
	multi	✓	9.42 ± 0.85	0.426
GLAO	multi	✗	9.33 ± 0.97	0.281
	multi	✓	9.41 ± 0.63	0.195

Table 9.1: Wind measurements for different AO systems. The multilayer consists of nine layers and the moving average is taken over 200 ms, while the usual average is only taken over 20 ms. The theoretical wind speed of the ground layer is 10 m s^{-1} . The RMSE is, as usual, taken over a two second measurement.

The second error source of the multilayer atmosphere is that the cross correlation detects the dominant wind vector from the ground layer, but the tip and tilt are measured over the whole atmosphere. Therefore, P-REx calculates the product of the ground layer wind with the whole tip and tilt. This is not a huge problem as one expects the layers to move in similar directions, it does, however, introduce an additional error in the final piston reconstruction.

A possible way to reduce the error from the wind measurement is, as discussed earlier, the moving average for the wind detection. This is done for the results shown in Figure 9.2 and lead to a wind measurement of $(9.42 \pm 0.85) \text{ m s}^{-1}$, which is very similar to the single layer measurement without moving average. For a comparison of the different wind measurements see Table 9.1. The result that the wind speed is in general a little underestimated is due to the peak detection from the cross correlation. The peak detection tends to slightly underestimate the peak movement, especially for small shifts, as discussed in chapter 7.

With the moving average, the RMSE values of the reconstructed piston over two seconds are in the range between 0.3 to 0.5 μm , dependent on the used atmosphere. An example for the reconstructed piston is shown in Figure 9.3. Considering the error ranges, as discussed before, this means that the piston reconstruction can be usable from these values for observations in the NIR and MIR. An usage of the P-REx system for observations in the optical seems difficult, at least over a timespan of two seconds. However, Figure 9.3 shows a very good reconstruction in the first 0.5 s. Considering only this timespan, the RMSE drops down to below 0.2 μm . With this in mind, it could be possible to use P-REx, but on shorter timescales as tested here. The important conclusion from this data is that the P-REx system is able to detect and follow the piston movement, even for a realistic atmosphere with several layers.

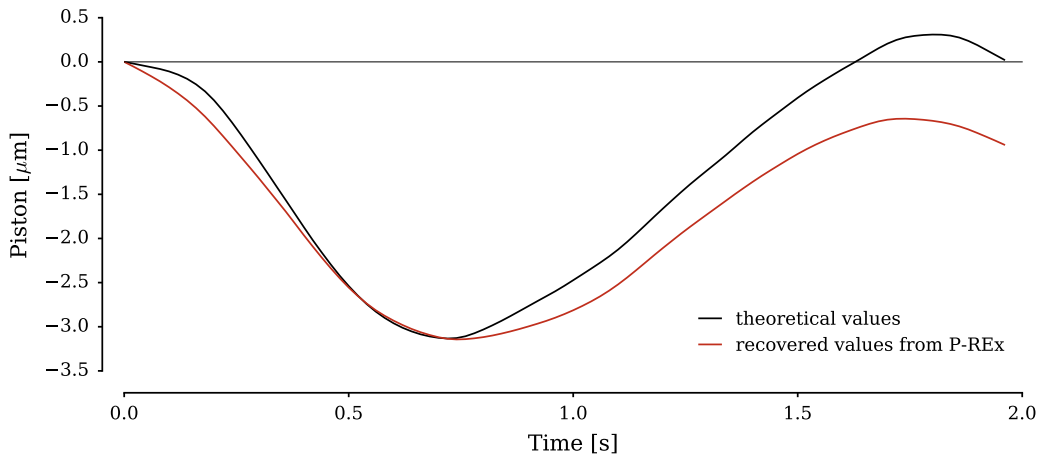


Figure 9.3: Piston reconstruction for a SCAO system with a multilayer atmosphere. The theoretical piston is shown in black and the reconstructed piston is shown in red.

9.2 GROUND LAYER ADAPTIVE OPTICS

The same simulations as before are now done for a ground layer adaptive optics system. For the simulation, a system is used that includes four SH WFS which are pointed at four different laser guide stars (LGSs), in order to observe the ground layer turbulence. The LGSs have a separation of $60''$ from the target and are produced by Rayleigh lasers, which are scattered back at a height of approximately 12 km. An additional 2x2 SH WFS is used with a natural guide star at the center of the field of view, in order to measure the tip and the tilt from the atmosphere, as this cannot be done with the LGSs. The YAO parameter file for this simulation can be found in Appendix C. Such a system could also be used with NGSs (as for example done for LINC-NIRVANA), but the approach with LGSs is more common. The here used system is similar to ARGOS at the LBT, which uses three Rayleigh lasers for the GLAO system.

The idea for the GLAO system is that one can get a better wind vector measurement from the data, as the noise due to the upper layers of the atmosphere is reduced. An important point for the piston reconstruction is that one has to use the wind vector from the ground layer, but the tip and tilt from the whole atmosphere. Otherwise one would only measure the piston of the atmosphere and neglect all the other layers. The approach of taking the tip and tilt from the whole atmosphere works, as long as the different layers move in a similar direction. If the layers would move in totally different directions, the results would probably not be very convincing. Luckily, atmospheric studies have shown that the wind direction stays fairly stable with increasing height. Furthermore, this approach is also more realistic, as the measurement from the LGS does not include the tip and tilt. As the light of the lasers crosses the atmosphere twice, the tip and tilt information is canceled out. Therefore the tip and tilt have to be measured with a NGS, which always gives values for the whole atmosphere. Consequently, the approach with the complete tip and tilt values gives better results and is also more practical for a real use of the system.

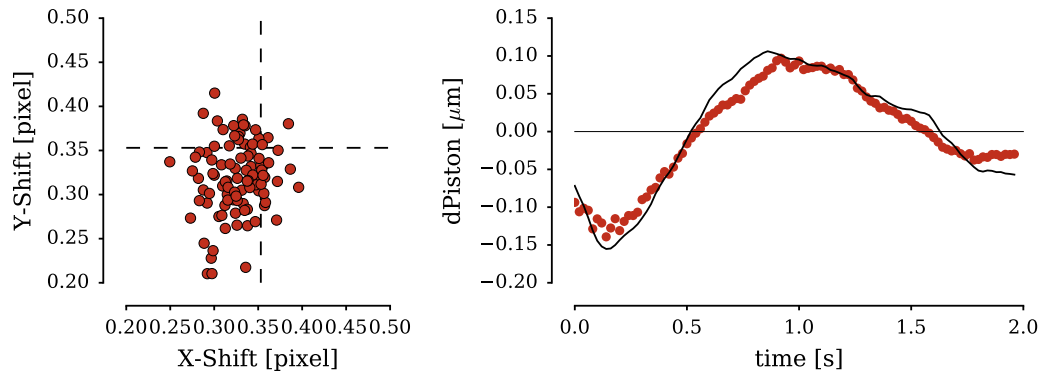


Figure 9.4: P-REx performance for a GLAO system with a multilayer atmosphere. The left image shows the detected wind speeds as red dots, with the theoretical speed of the ground layer shown by the dashed cross. The right image shows the reconstructed differential piston as red dots with the theoretical values as a black line. The RMSE from this simulation is $0.281 \mu\text{m}$ (see Table 9.1).

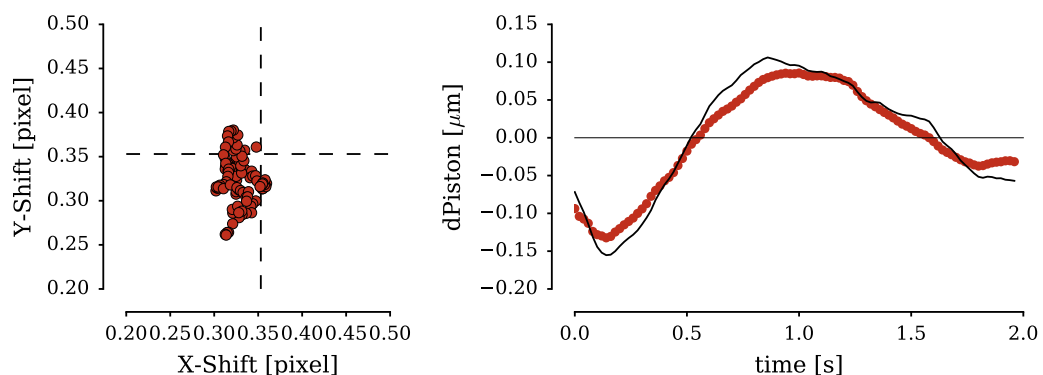


Figure 9.5: Same plots as in Figure 9.4 but this time a moving average over 200 ms is used for the cross correlation, in order to improve the wind vector measurement. The RMSE from this simulation is $0.195 \mu\text{m}$.

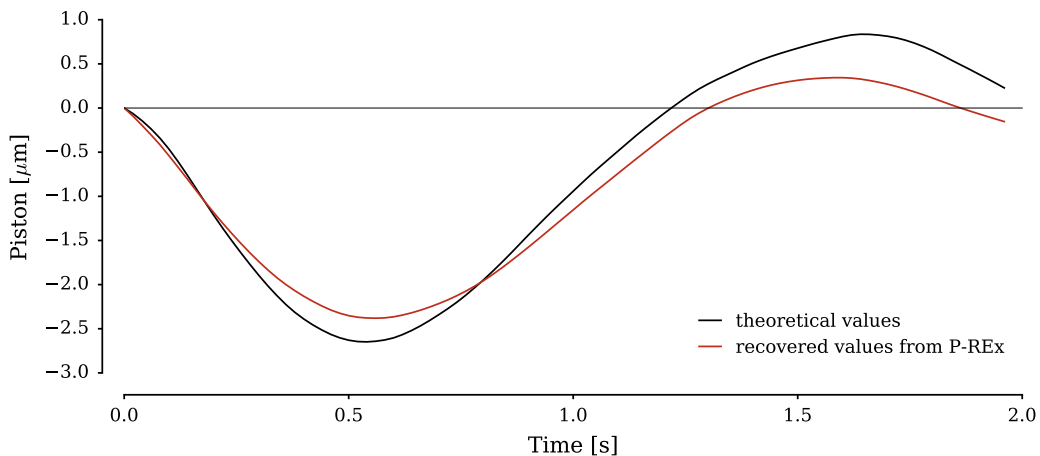


Figure 9.6: Piston reconstruction for a GLAO system with a multilayer atmosphere. The theoretical piston is shown in black and the reconstructed piston is shown in red.

The results for the ground layer simulations are shown in Figure 9.4 and Figure 9.5. Both figures show the results from a multilayer atmosphere, but the first one with the usual average and the second one with the moving average. The measurement of the wind speed gives $(9.33 \pm 0.97) \text{ m s}^{-1}$ for the normal average and $(9.41 \pm 0.63) \text{ m s}^{-1}$ for the moving average. As before, the values are within the error range of the real wind speed of 10 m s^{-1} . However, for the GLAO system the standard deviation of the wind measurement is indeed smaller than for the SCAO system and comparable to the results from a single layer simulation (see Table 9.1).

The result of the complete piston reconstruction for the used atmosphere is shown in Figure 9.6. In comparison to the same plot from the SCAO system (see Figure 9.3), the results from the GLAO measurement are slightly better, which leads to an improved RMSE in the range of 0.2 to $0.3 \mu\text{m}$. This can also be seen in the RMSE values from the individual simulations, which are shown in Table 9.1. This means that the piston reconstruction for a GLAO system shows results which are good for observations in the NIR and may even be usable, under good conditions, for optical wavelengths. As mentioned for the SCAO systems, this even improves when looking on shorter timescales.

When comparing the piston reconstruction for the SCAO and GLAO system (Figure 9.3 and Figure 9.6), one can see that the theoretical piston values are not exactly the same. The reason for this difference is that the GLAO system has a larger field of view and therefore the input atmosphere from YAO is slightly different than for a SCAO system.

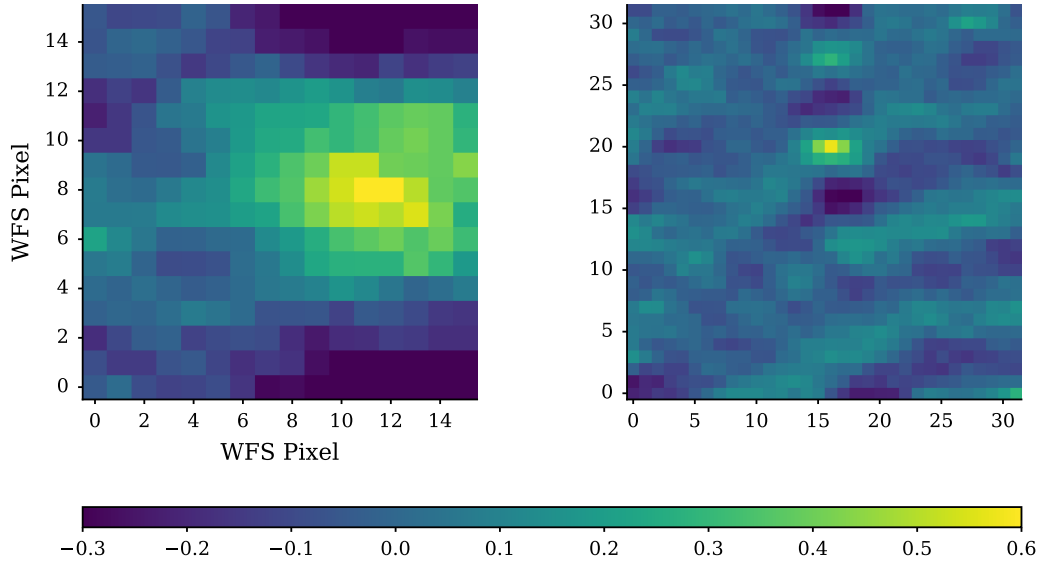


Figure 9.7: Wind detection from a MCAO system for the ground layer wind in the left image and the upper layer wind in the right image.

9.3 MULTI-CONJUGATED ADAPTIVE OPTICS

A MCAO system has two separate optical systems with several WFSs and DMs which are conjugated to different layers. Therefore, one can in theory detect the wind velocity from different layers. I tested this in simulations of a MCAO system and a two layer atmosphere. The atmosphere consists of a ground layer moving in positive x direction and an upper layer moving in positive y direction. Figure 9.7 shows the cross correlations of the ground layer WFSs and the high layer WFSs. The system conjugated to the ground layer and the one conjugated to the high layer clearly detect different movements, with approximately 90 degrees difference between them. This shows that such a system is able to detect the wind from different layers.

Such a measurement could be used together with a specific turbulence profile, as the one in Figure 2.2, in order to calculate the piston evolution from different layers. However, this has to be tested for a very specific case in order to match the real wind measurements with a real turbulence profile, but there is currently no working MCAO system available at the LBT or VLTI. Therefore, the use of a MCAO system is an idea for further research, as it should theoretically work, but is not of main interest here.

9.4 CONCLUSION FROM SIMULATIONS

The simulations generally show a good performance of the piston reconstruction. The main results from the simulations are listed in the following:

- The piston reconstruction works well for a single layer atmosphere under typical seeing conditions.
- The most important criterion is to have a sufficiently high WFS sampling, typically larger than 10x10 subapertures with an individual subaperture size in the order of r_0 . The higher the sampling, the more precise is the wind measurement.
- The best results for realistic systems were achieved for an 8 m telescope with a 30x30 element WFS. This is given for example by the FLAO system at the LBT, but also the CIAO and MACAO systems at VLT showed promising results in the simulations.
- In order to get a reliable wind vector from SCAO or GLAO WFS data, the majority of the turbulence has to be located in the ground layer, which is usually the case. The ground layer wind vector can be reliably determined also from a realistic multilayer atmosphere, even at the existence of high layer turbulence.
- P-Rex is able to reconstruct the piston evolution under realistic conditions.
- The use of a GLAO system can further improve the result in comparison to a SCAO system, due to the cleaner wind measurement of the dominating ground layer. This can also be interesting for a multilayer instrument, such as LINC-NIRVANA at the LBT.

The only effect that was not considered yet in the simulation, is the temporal evolution of the atmosphere beyond the assumption of TFFH, namely the boiling. As mentioned earlier, there are possible ways to include boiling into the simulations. However, the main parameters of boiling, such as the strength, are not clear and simulating a phase screen with chaotic behavior is not well understood. Therefore, in the next part I show how good the concepts work for real data. So far I can say that there is no critical parameter in the simulation which precludes the use of P-Rex. From the results until here it looks very good that P-Rex can deliver a reliable piston reconstruction under good conditions.

Part III

WORKING WITH LBT DATA

WIND VECTOR MEASUREMENT

10

In order to better understand the effects of a real atmosphere on the piston reconstruction, I now use data from the LBT first light AO (FLAO) system. This chapter first introduces the used data and then shows the capability of measuring a wind vector from the data. As the wind measurement is crucial for the piston reconstruction, this is a very important first step in order to understand the capabilities of the system for real data.

10.1 INTRODUCTION TO THE DATA

The used data are from the early tests of the first light AO (FLAO) system at the LBT. As mentioned earlier, FLAO uses a pyramid sensor which can be used with different binning modes. The data here has been observed in the highest binning mode, which means that it consists of 30x30 slopes. The high binning is important in order to get the best wind measurement. Apart from the WFS data, the datasets consist of the DM voltages and the IM, which are necessary to reconstruct the POL slopes. Further data, such as the wind velocity measured at the LBT and the seeing, are used for verification of the measurements, but are in principle not necessary for P-REx.

The data consists of 17 datasets with measurements over four seconds. It is taken at two different nights in 2012, with a very good seeing in the first night and medium conditions in the second night. Both datasets are from the left of the two LBT telescopes (usually referred to as SX). The data has been provided by A. Puglisi in personal communication. The main parameters of the datasets are listed in Table 10.1.

	Night 1	Night 2
Date	17.9.2012	20.9.2012
Number of datasets	12	5
Average seeing	0.50''	0.90''
Average wind velocity	2.31 m s^{-1}	4.51 m s^{-1}

Table 10.1: Main properties of the used data from the LBT FLAO system. The seeing and the wind velocity are averages over the datasets, measured at the LBT.

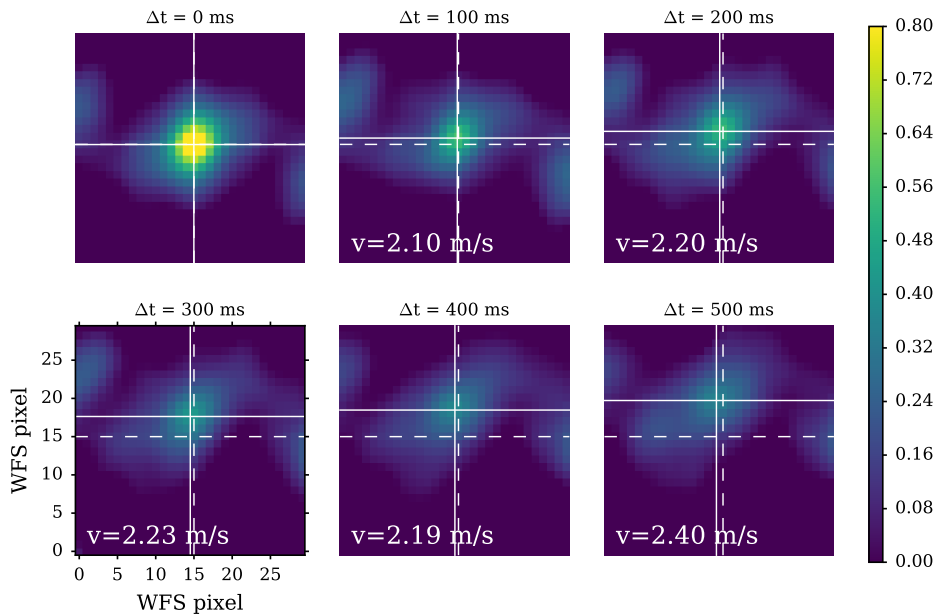


Figure 10.1: Wind measurement from FLAO data. The elapsed time in the cross correlation is increasing from the top left to the bottom right with steps of 100 ms per image. The center of the image is shown with a dashed cross and the peak of the image with a solid cross. The measured wind velocity is given for each image.

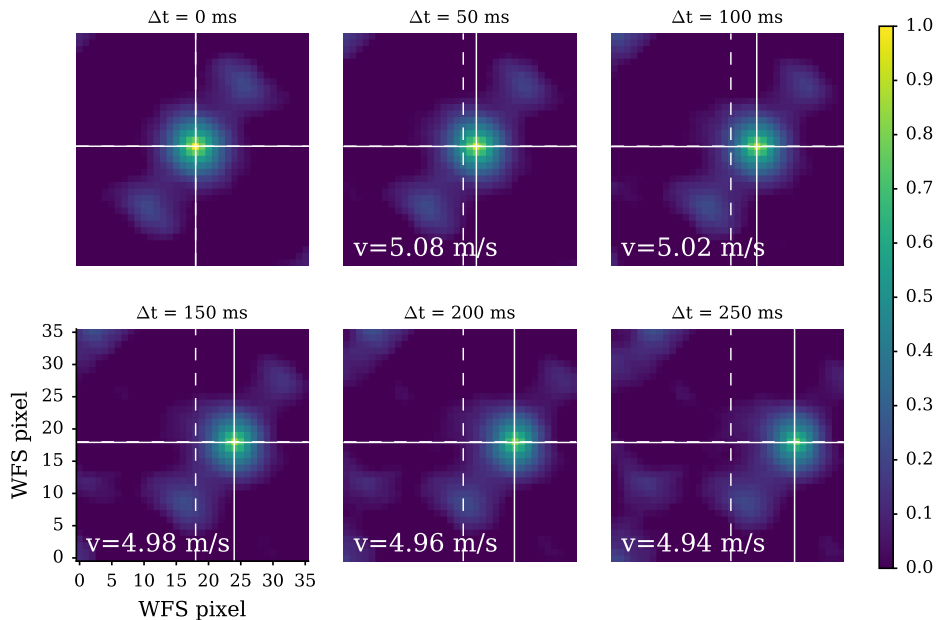


Figure 10.2: Wind measurement from simulated FLAO data for a single layer atmosphere with a theoretical wind speed of 5 m s^{-1} in x direction. The elapsed time in the cross correlation is increasing from the top left to the bottom right with steps of 50 ms per image.

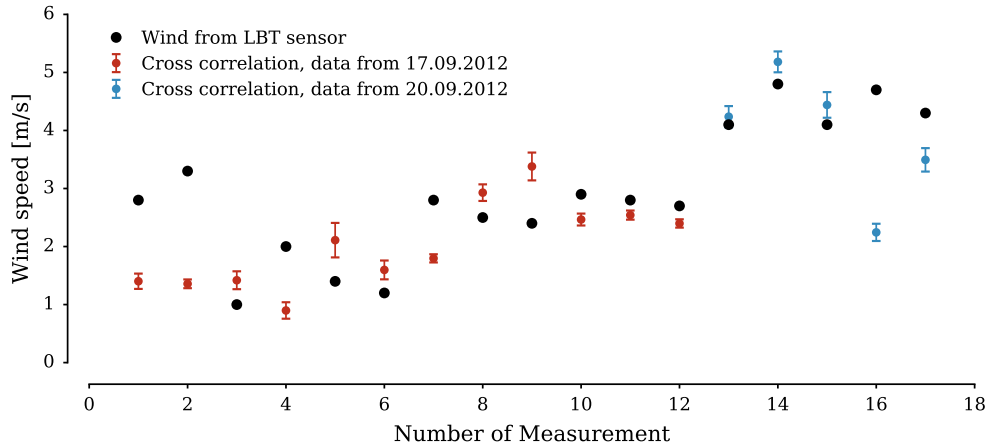


Figure 10.3: Comparison of the wind velocity measured from the cross correlation (red for the first night, blue for the second) and the wind sensor directly measured at the LBT (black). The error bars are the standard deviation over the individual dataset of four seconds.

10.2 WIND MEASUREMENT

A first test of the LBT data has the goal to see whether it is possible to measure the dominant wind vector. This is a crucial measurement, as the wind vector is absolutely necessary for the use of P-REx. Figure 10.1 shows the cross correlation of the POL slope data for different time shifts, taken from one single dataset. It is clearly visible that the peak position shows an increasing distance from the center of the image, as it is expected for an increasing time difference. From the peak position one can directly calculate the wind velocity, under the assumption that the ground layer is the dominant layer. The wind velocity stays nearly constant over the measurement of half a second, as shown in Figure 10.1. Unlike earlier cross correlations from simulations, the measurements here are the average over a timespan of half a second. This is done by calculating the individual cross correlation several times with a fixed time shift and then taking the average of the results. In this data, an average of 500 cross correlations gave the most stable wind measurement. Without such a long average, the SNR in the results is very low. This is probably due to the different effects of the real atmosphere that add additional noise to the measurement.

In order to verify this result, Figure 10.2 shows the same measurement from the simulation of the FLAO system. The simulation also uses a 30x30 pyramid WFS and a single layer atmosphere, moving with a wind velocity of 5.0 m s^{-1} . The main difference in comparison to the real data, apart from the single layer atmosphere, is that the cross correlations for the simulated data are calculated with only half of the time difference, as the wind velocity is approximately twice the one from the data.

The comparison of Figure 10.1 and Figure 10.2 shows a very similar behavior of the cross correlation, which verifies the measurement and the wind detection method. The main difference between the figures is that the intensity of the correlation peak in Figure 10.2 stays more or less constant, while the peak intensity in Figure 10.1 clearly decreases. This is expected, as the real atmosphere does not only show a translation but also changes due to

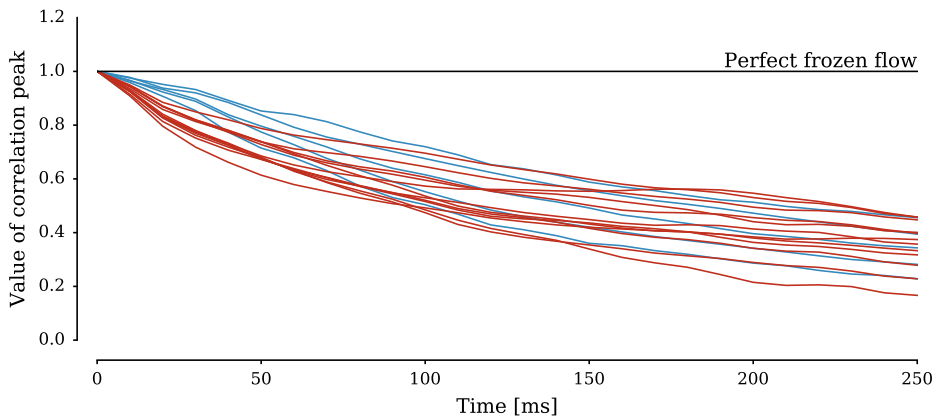


Figure 10.4: Evolution of the correlation peak over time. Every line is from a single dataset, with data in red from the first night and in blue from the second night.

boiling, which reduces the intensity of the correlation peak (see section 2.3 and Figure 2.5). The decreasing peak value can therefore be used to verify the intensity of boiling, as I show in the following section.

Looking just at Figure 10.1, the wind measurement seems reliable. In order to confirm this measurement, some other tests can be done. The wind strength is also measured directly at the LBT with a usual wind measurement and these data can be compared to the results from the cross correlation. Figure 10.3 shows the wind measurement from the cross correlation and the LBT measurement. The results are not identical, but are in a similar range. Also, the main trends in the data, such as a higher wind velocity in the second night, are visible in both measurements. The error bars in the cross correlation are not from the fit of the correlation peak, but from the standard deviation over the individual data set. The comparably small errors show that the wind is changing only little over the four second data.

The difference between the two measurements can be explained with the fact that the sensor at the LBT only measures the wind velocity directly at the telescope, while the cross correlation sees the whole atmosphere. As mentioned earlier, the wind measurement should be dominated by the ground layer, but a certain discrepancy to the wind directly measured at the telescope is understandable.

10.3 BOILING

As mentioned in the previous section, it is now possible to use these data to analyze the strength of the boiling in the atmosphere. Results from a similar analysis from Schöck and Spillar (2000) are shown in Figure 2.5. For an atmosphere solely moving by the wind velocity in perfect frozen flow, the intensity of the cross correlation peak would stay constant at one. By mapping the intensity of the peak over time one can therefore measure to what degree TFFH is valid in the actual data. In real data one expects the peak to decrease as the

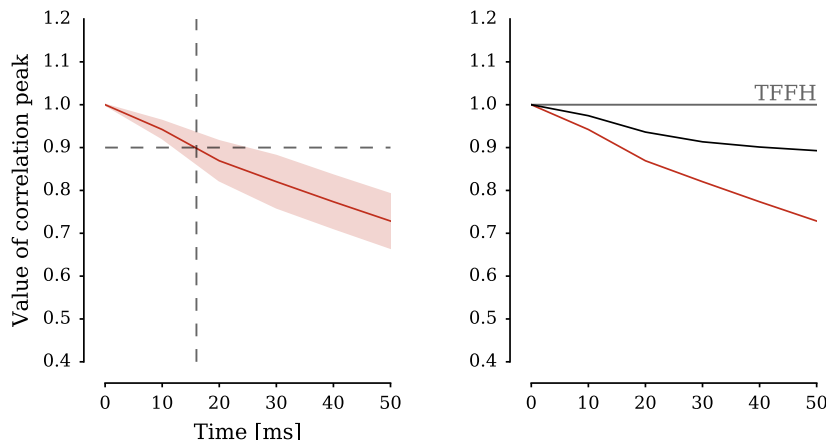


Figure 10.5: Evolution of the mean correlation peak over time as a red line. Left: The shaded area shows the standard deviation of the data. The dashed lines show the time at which the peak is at 90 % of its initial value. Right: In black the peak intensity from the multilayer simulation is shown and the gray line represents the value for a perfectly valid TFFH.

TFFH is not perfectly valid. The decrease in peak intensity is due to boiling, but as well due to the different layers of atmosphere moving into different directions. The evolution of the cross correlation peak intensity is shown in Figure 10.4 for all of the available FLAO datasets. What one can directly see is that the intensity is decreasing over time, as it is expected.

In order to further quantify this result, Figure 10.5 shows the same plot, but with the average value over all data sets for the first 50 ms. A value to quantify the impact of TFFH is t_{90} , the time over which TFFH is responsible for 90 % of the atmospheric evolution. From these data, one can conclude that t_{90} is approximately 16 ms. This result is a little less than what Schöck and Spillar (2000) found, as they had an average t_{90} of 25 ms. However, the results are comparable. This furthermore confirms the assumption that TFFH is responsible for the main atmospheric evolution over short timescales and verifies the used timescales of 10 to 20 ms. For comparison, the black line in the right plot of Figure 10.5 shows the result of the same analysis but with the data from the multilayer simulation of chapter 9. In these data there is no boiling and therefore the decrease in intensity is only due to the multilayer movement of the atmosphere. As expected the decrease in intensity is slower in these data, however it is still clearly visible. From this behavior one can see that both, the multilayer movement as well as the boiling, are contributing to the decorrelation of the atmosphere.

In conclusion this boiling analysis shows that boiling is not a limiting factor for the usage of P-REx. The wind vector measurement can be done on timescales where boiling is clearly present, without loosing sensitivity. This is shown in 10.1, where the correlation peak is visible over timescales of 0.5 s. By decoupling the wind measurement and the piston drift reconstruction, it is easily possible to run P-REx on timescales in the order of 10 ms, where the frozen flow clearly dominates. One can therefore conclude that boiling has only little effect on the performance of P-REx.

This chapter is now dedicated to test the usability of P-REx with the FLAO data. As the used data is only from one telescope, I use reconstructed interferometric data by cutting out two subregions of the slope data and by comparing it to the same regions in a reconstructed phase front. This method is first applied to simulation data, in order to show its usability, and then used with the LBT FLAO data.

11.1 PRINCIPLE OF THE VERIFICATION METHOD

Ideally, one has to test the P-REx algorithm on interferometric data and compare it to the fringe tracker measurement from the same dataset. However, it is also possible to test the usability of P-REx on single aperture data. In order to do so, a different verification method has to be applied.

This method involves cutting out two circular regions from the actual slope data. The idea is then to think of these two regions as virtual telescopes and to calculate the piston evolution for both of them. By subtracting the two measurements one gets the same measurement as for a real interferometer, which can be compared to the piston evolution for the same regions from a reconstructed wavefront. The principle of this *single aperture method* is illustrated in Figure 11.1 and is explained in more detail in the following paragraphs.

RECONSTRUCTION

Starting with the verification part of the single aperture method, the first step is to reconstruct the wavefront from the POL slopes. For the reconstruction of the wavefront the same method is used as earlier for the full P-REx algorithm. This consists of building a reconstructor to calculate the Zernike modes from the slope and then image the wavefront from these modes. More information on this can be found in Appendix A. As there is no piston information in the slopes, the reconstructed wavefront \widehat{WF} differs from the real wavefront WF , as it is reduced by the piston $\langle WF \rangle$ and has an average value of zero:

$$\widehat{WF} = WF - \langle WF \rangle \Rightarrow P_{\widehat{WF}} = \langle \widehat{WF} \rangle = 0 \quad (11.1)$$

In the following formulas, the notation with a hat, such as \widehat{WF} , always corresponds to the piston reduced value. As shown in the left part of Figure 11.1, the next step is to cut out two circular frames, \hat{f}_1 and \hat{f}_2 , from the big wavefront. In the same way as for the complete

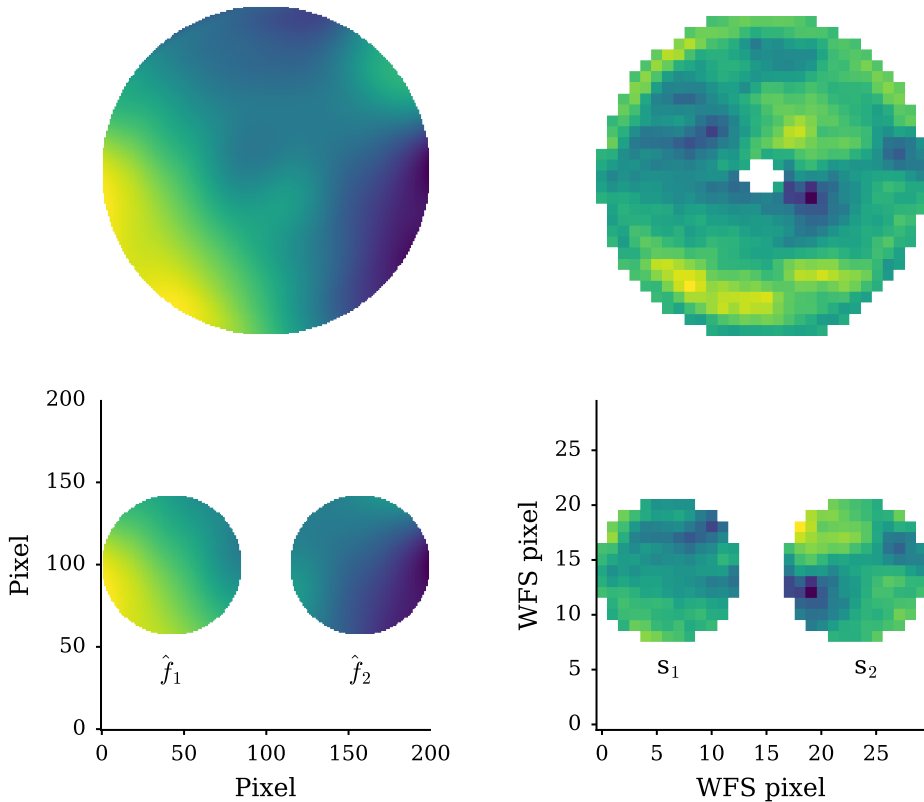


Figure 11.1: Explanation of the single aperture mode with the two subapertures from the reconstruction (left) and from the slope data (right).

wavefront, the main piston is reduced from these two frames. However, as this is not the piston of the frames, they have an individual piston value:

$$\begin{aligned}\hat{f}_i &= f_i - \langle WF \rangle \\ \Rightarrow P_i &= \langle \hat{f}_i \rangle \neq 0\end{aligned}\tag{11.2}$$

The value which is now of interest is the piston difference between the two frames which is equivalent to the real piston difference between these two regions of the atmosphere, as can be seen in the following calculation:

$$\begin{aligned}dP_{\text{recon}} &= P_1 - P_2 = \langle \hat{f}_1 \rangle - \langle \hat{f}_2 \rangle \\ &= \langle f_1 - \langle WF \rangle \rangle - \langle f_2 - \langle WF \rangle \rangle \\ &= \langle f_1 \rangle - \langle f_2 \rangle\end{aligned}\tag{11.3}$$

This value is then called the reconstructed piston difference (dP_{recon}) and is, calculated for each time step, the reference value for this P-REx test.

SLOPES

The actual measurement is then done on the POL slopes, as shown in the right part of Figure 11.1. Again, one has two cut out the same regions from the slope data, which are now named s_1 and s_2 . For these two regions one can then calculate the differential piston with the P-REx algorithm (see Equation 5.8):

$$\Delta P_i(t) = [\langle s_{ix} \rangle \cdot v_x + \langle s_{iy} \rangle \cdot v_y] \cdot \Delta t \quad (11.4)$$

By adding up the differential piston for each of the two parts, one gets the piston evolution $P_{i,sl}$, which is correct except for a constant factor, the initial piston value $P_{i,t=0}$:

$$P_{i,sl}(T) = \sum_{t=0}^T \Delta P_i(t) = P_i(T) - P_{i,t=0} \quad (11.5)$$

The difference of these two piston evolutions is then the result of this part, the piston difference from the slope measurement dP_{sl} :

$$\begin{aligned} dP_{sl}(T) &= \sum_{t=0}^T \Delta P_1(t) - \sum_{t=0}^T \Delta P_2(t) \\ &= P_{1,sl} - P_{2,sl} - \underbrace{(P_{1,t=0} - P_{2,t=0})}_{=C} = dP - C \end{aligned} \quad (11.6)$$

which is again the real piston difference between these two regions, except for the difference of the initial values.

COMBINATION

The last step is to show that the measured values can be compared. From the fact that the reconstructed piston difference is the actual piston difference, one gets:

$$dP_{\text{recon}}(t) = dP(t) = dP_{sl}(t) + C \quad (11.7)$$

From the condition that $dP_{sl}(t = 0) = 0$, one gets: $C = dP_{\text{recon}}(t = 0)$ and with that:

$$dP_{\text{recon}}(t) - dP_{\text{recon}}(t = 0) = dP_{sl}(t) \quad (11.8)$$

This means that by subtracting the initial value from dP_{recon} , the results of the two measurements are equal.

11.2 TEST ON SIMULATION

The advantage of first testing the single aperture method on simulation data is that one can better understand the reliability and possible error sources of the method. I therefore run a simulation with an AO system comparable to FLAO. The single aperture method is then

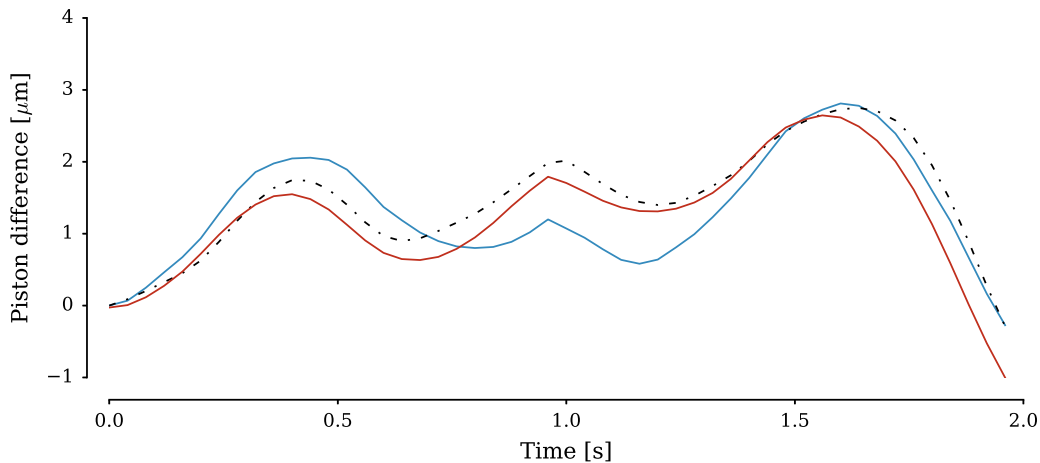


Figure 11.2: Single aperture method used on data from a YAO simulation. The red line shows the piston difference calculated from P-REx, the blue line from the reconstructed wavefronts and the black dashed line the real values.

applied to the simulation data exactly in the same way as it has to be done with the LBT data. The simulated data offers an additional verification step, as the input atmosphere is known. One can therefore cut out the same regions from the real atmosphere as in the reconstructed wavefront and calculate the real theoretical piston difference. This is done for Figure 11.2, where the piston difference from the slopes, from the reconstructed wavefront, and from the real atmosphere is shown.

The first thing one can see in Figure 11.2 is that the values from the reconstructed wavefront and the real values are not equal. The difference between these two measurements is probably due to the non perfect reconstruction of the wavefront. As already discussed in chapter 8 and shown in Figure 8.5, the wavefront reconstruction with Zernike modes is not completely correct, as it mainly lacks of small scale structure and includes a certain fitting error. This disagreement between the real atmosphere and the reconstructed wavefront becomes a bigger problem here, as the missing small scale structure gets more important by cutting out sub regions from the big phase screen. This then leads to the mismatch between the two theoretical values in Figure 11.2.

The error in the control loop leads to the result that the P-REx values from the single aperture method seem to be worse than they actually are. The RMSE between the P-REx values and the values from the reconstructed wavefront is $0.47 \mu\text{m}$ for this simulation, while the RMSE between the P-REx values and the measurement from the real atmosphere is only $0.34 \mu\text{m}$. These results show that the single aperture method only gives a lower limit for the quality of the reconstructed piston, as the control values are not perfectly correct.

Furthermore, the RMSE of $0.34 \mu\text{m}$ is worse than one would expect from previous tests. This is mainly due to the fact that the P-REx results improve with the sampling of the WFS. By cutting out the two regions, one decreases this sampling from one 30×30 WFS to two 12×12 WFSs. Therefore, the result should be better for using the whole aperture than it is

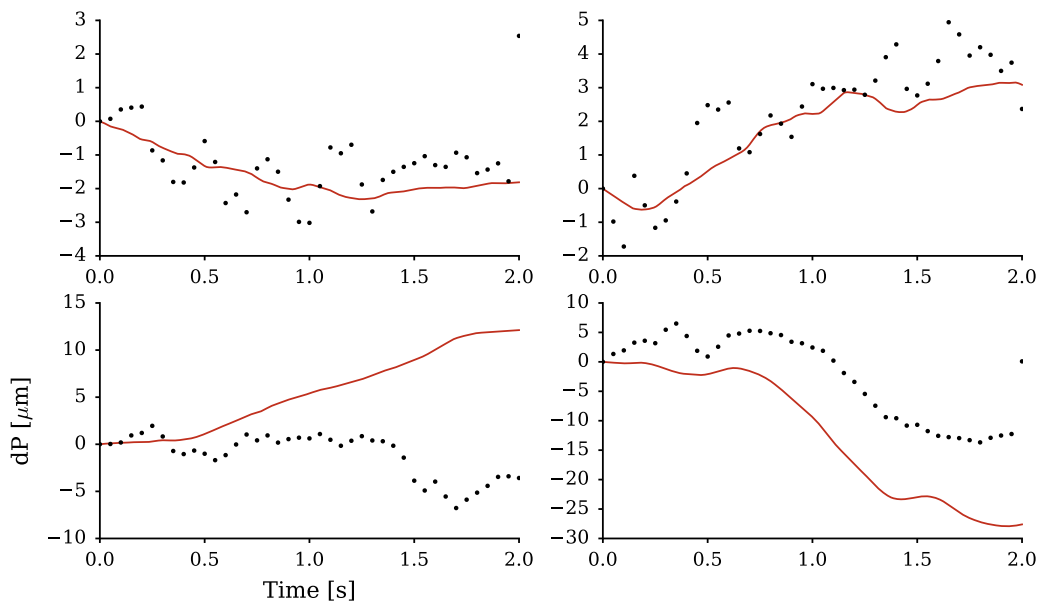


Figure 11.3: Four examples from the results of the single aperture method for LBT FLAO data. In all plots the red line is from the P-REx measurement and the black dots are from the reconstructed wavefront. The examples show the full range of results, with a good reconstruction for two examples in the upper row and two bad examples in the bottom row.

for the subregions used here. Despite the flaws of this method, one can still use it on the LBT data to give an indication whether P-REx can work under real conditions.

11.3 RESULTS FROM LBT DATA

The single aperture method is now applied to the LBT FLAO data. As mentioned earlier, the wind measurement needs a relatively long average in order to give consistent results. Therefore, the wind is measured over one second with a moving average. The P-REx calculation is then not limited by the wind measurement and can basically be done with the same frequency as the wavefront sensing. In order to improve the SNR of the measurement, an average over five tip and tilt measurements is taken, which corresponds to a timespan of 5 ms. This means that the P-REx algorithm would run with approximately 200 Hz in this specific case.

The results from the data are non-uniform. The results from the P-REx measurement of some datasets show a very similar behavior as the results from the wavefront reconstruction, while in other datasets the two measurements show a very different behavior in the piston difference. This is shown for four examples in Figure 11.3. With this four examples one can see the full range of possible results. For the upper two plots in Figure 11.3 the reconstruction is very similar to the theoretical values over the whole time. The two lower plots show two

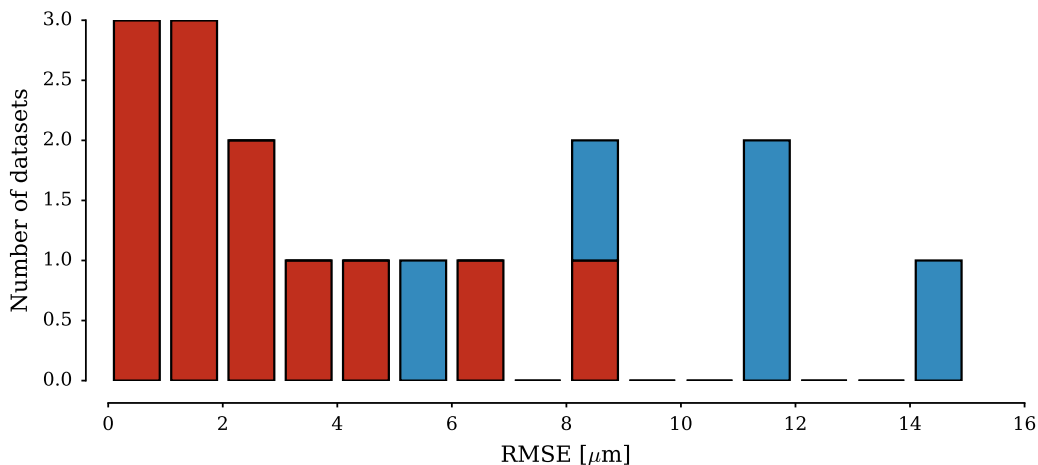


Figure 11.4: Histogram of the RMSE of the 12 FLAO datasets from the single aperture method. The datasets from the first night are shown in red and the datasets from the second night are shown in blue.

	Night 1	Night 2
Average seeing	0.50''	0.90''
Wavelength	650 nm	650 nm
r_0	27 cm	37 cm
$D/r_0(D=8\text{ m})$	30	22
$D/r_0(D=3.5\text{ m})$	13	9

Table 11.1: Atmospheric properties of the used data from the LBT FLAO system.

of the bad examples. While both of them lead to a high RMSE (5.9 and 8.0 μm), the actual trend is very different. While the reconstruction in the left plot is completely wrong, the reconstruction in the right plot shows the trend of the theoretical piston evolution rather good. However, a piling up error from the beginning decreases the final result. This is therefore an example where one can see that a low frequency fringe tracker would very much improve the result.

The large range of different results shows that a conclusive statement from these data is challenging. In order to get some statistics from the data, Figure 11.4 shows a histogram of the RMSE between the piston difference from P-REx results and from the reconstructed wavefront.

A first conclusion from this histogram is that the results from the first night (shown in red) are in general better than from the second night (shown in blue). This confirms the result from the simulations that the piston reconstruction improves for better atmospheric conditions. In order to further understand the results, one needs to compare them to the expected values from simulations. Table 11.1 summarizes the atmospheric conditions during the observations. With these data one can use Figure 8.11 to analyze the expected quality

of the piston reconstruction. As the single aperture method does only use sub apertures of the whole telescope, the telescope size of the used aperture is roughly 3.5 m. This leads to a D/r_0 of 13 for the first night and of 9 for the second night. For the present r_0 , the wavefront sampling is in the order of 0.75 measurements per r_0 . Looking at Figure 8.11, a sampling of 0.75 measurements per r_0 for a D/r_0 of roughly 10 gives expected RMSE values in the order of 1 μm . Looking at the data in Figure 11.4, one can see that half of the datasets from the first night have a RMSE below 2 μm and two thirds below 3 μm . Considering the fact that the reconstructed values are not perfectly correct, as was shown in simulations, these results are reasonably close to the values expected from the simulations. Furthermore, the simulations are done for a single layer atmosphere and therefore the results from the real atmosphere are expected to be a little worse.

The comparison of the results from real data and from simulations lead to some important conclusions. First of all, the results fit together within a reasonable range, which shows that the assumptions done in the simulations were valid. This mainly approves that the boiling can be neglected over very short timescales. One can furthermore conclude that the results from simulations are accurate, which then also means that the results from P-REx should significantly improve by using the whole telescope with a much higher D/r_0 , as shown in the simulations. However, Figure 11.4 also indicates that the results from the piston reconstruction heavily depend on the atmospheric conditions and that P-REx is most usable under good seeing conditions.

ATMOSPHERIC CONDITIONS ADVERSE TO P-REX

Despite some positive conclusions from the different datasets, the question remains why some of the data from the first night show comparably bad results from the piston reconstruction. The seeing conditions were not varying much during that night, but there are still some datasets which do not deliver good results. In order to look at different possibilities for that, Figure 11.5 shows the RMSE from the different measurements as a function of the wind stability. This is done in two different ways: The first one is to study the temporal variance of the wind velocity, as shown in the upper plot of Figure 11.5, by plotting the RMSE against the standard deviation of the wind measurement over the four second dataset. The lower plot shows RMSE in comparison to the spatial variance of the wind velocity. This is done by measuring the wind in four different sub apertures and taking the standard deviation of these four measurements. This means that data points on the right side of the plots show an unstable wind over time (upper plot) or over the size of the telescope aperture (lower plot). In order to better track the individual datasets, they are numbered from 1 to 17 and the number is printed next to the data point.

A first outcome of these plots is that the wind is much less stable in the second night. This was somehow expected, as the atmospheric conditions are in general worse in that night. Focusing on the data from the first night, one can see that the datasets with the biggest RMSE, which are datasets 8 and 9, show either a high temporal instability (9) or a high spatial variability (8). This shows that a bad result of the piston reconstruction can be the effect of a quickly changing or unstable wind vector. However, one also has to point out that this is not necessarily the case, as some data sets, such as number 5 and 6, show a high

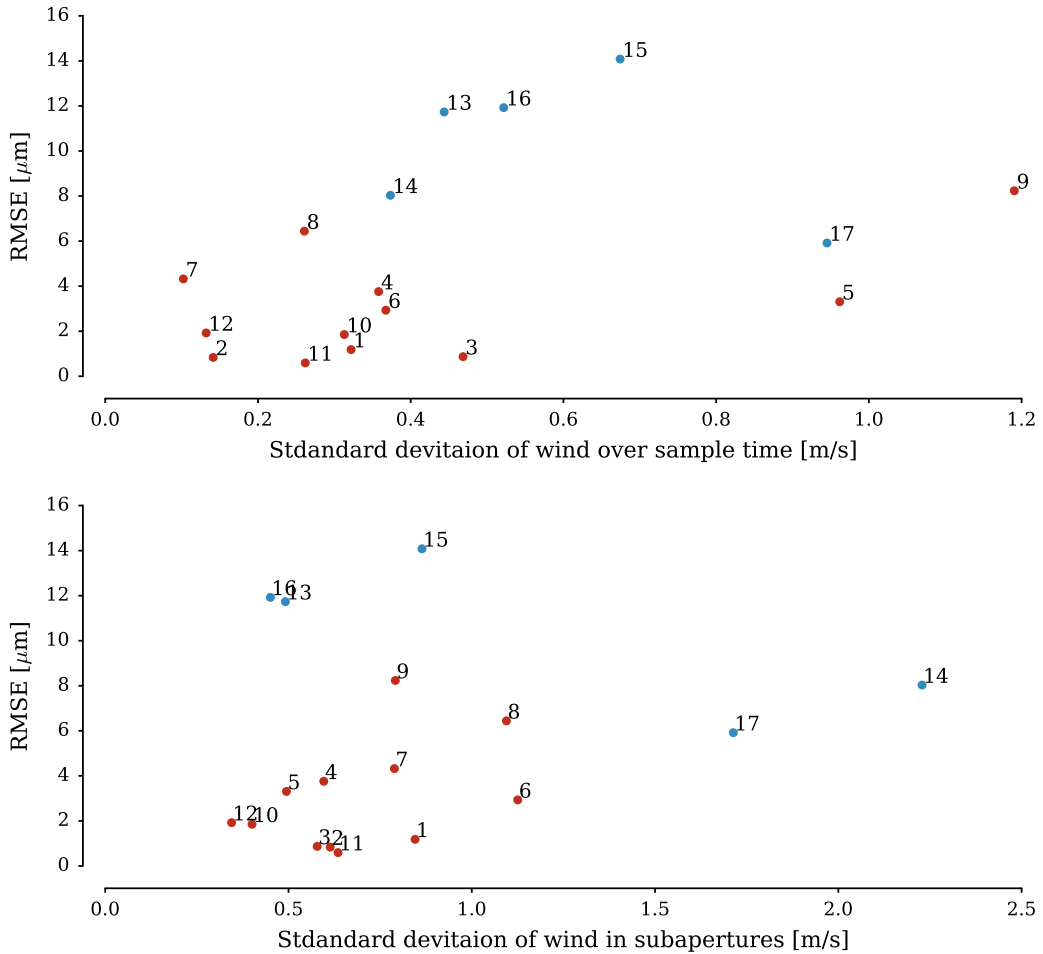


Figure 11.5: Statistics of the single aperture mode with LBT FLAO data: the y axis in both images gives the RMSE value of the reconstruction with the single aperture method. The x axis of the upper image shows the standard deviation of the wind over the four seconds of the measurement (small values show a stable wind vector). The lower image shows the standard deviation of the wind measurement in four sub apertures of the telescope (small values mean a uniform wind over the whole aperture). The number of the measurement is given for each data point in both plots with the number next to the data point. Data from the first night is shown in red, data from the second night is shown in blue.

instability, but a good piston reconstruction. Therefore, the changing wind vector can be a factor but does not necessarily has to be.

11.4 CONCLUSION FROM LBT DATA

Before finishing this work with the final discussion, I shortly want to summarize the main results from the test on the LBT data, which largely confirm the results from the simulations (see section 9.4):

- A wind vector is clearly detectable in all the datasets, which is a prerequisite for the real application of P-REx.
- The boiling intensity and timescale in these data are similar to previous studies. The found timescales confirm that boiling has only little impact on the result of P-REx.
- The performance of the piston drift reconstruction is similar to the expectations from simulations. This suggests that the main assumptions in the simulations were valid and approves the results from simulations. One can therefore assume that the P-REx results for a full aperture of an 8 m class interferometer are significantly better than for the here presented single aperture tests with the two small subregions.
- The P-REx tests on the FLAO data with good atmospheric conditions give mixed results for one third of the datasets. For the other two thirds, P-REx delivers an OPD RMSE below $3 \mu\text{m}$.
- The tests showed that a varying wind vector and bad atmospheric conditions influence the quality of the P-REx results.
- The results show a possible usability of the piston reconstruction, which would encourage experiments with a MIR science wavelength. Further performance predictions would require two telescope interferometric data, due to the discussed limitations of the single aperture testing method. A comparison of high-resolution AO data with fringe tracking data would therefore be the next step.

The most important points to take from the tests on a single aperture are, that the atmosphere is, under good observation conditions, sufficient well structured and stable, in order to measure the dominant wind vector and apply the piston reconstruction algorithm. This leads to a principal usability of the Piston Reconstruction Experiment.

CONCLUSION AND OUTLOOK

12

The goal of this work was to develop and test a method to reconstruct the piston drift evolution over a single telescope, in order to improve the sensitivity of large optical and NIR interferometers. With the Piston Reconstruction Experiment presented in this work such a reconstruction of the piston drift evolution has been studied for the first time, both in realistic simulations and with real data. The idea for the final application is to implement the piston reconstruction system at an existing interferometer. With the support of P-REx the interferometric fringes can be stabilized over short timescales, which would allow the existing fringe tracker to run at much lower frequencies than usual. This would decrease the problems of the fringe trackers as well as improve their sensitivity, which should possibly lead to a more stable fringe position and therefore to an increasing sensitivity of the interferometer.

In this work, the main principle of the P-REx and its theoretical usability have been demonstrated. Extensive tests with data from simulated adaptive optics systems proved the possibility of the piston reconstruction under usual atmospheric conditions. These tests led to the result that the limiting factors for the quality of the piston reconstruction are the multilayer atmosphere and the spatial sampling of the wavefront sensor. A mandatory prerequisite for the piston reconstruction is therefore an atmosphere with a dominant ground layer, containing at least 60 % of the total atmospheric turbulence. As different studies showed that this is often the case, the multilayer behavior of the atmosphere should not be a show-stopper. A usually critical aspect for systems which try to retrace the atmospheric behavior, such as P-REx, is the chaotic evolution of the atmosphere due to boiling. In order to analyze the impact of boiling on the piston reconstruction, as well as its usability under real conditions, the last part of this work dealt with the application of P-REx on real AO data. Although the used data was not ideal to test the system, the results were promising. The piston reconstruction showed good results for around two thirds of the data with good seeing conditions. For these data a reconstruction of the piston drift with an error smaller than $3 \mu\text{m}$ is possible. This result however does not yet describe the best possible performance, as the testing method itself is limited by wavefront reconstruction errors. Furthermore, the results would significantly improve for a real system, as I only used a simulated interferometer with two small subapertures from the whole 8 m aperture. A real interferometer would have a higher wavefront sampling, which directly improves the piston reconstruction. Nevertheless, the results from the LBT data proved the assumptions on the structure of the turbulence and showed that under good atmospheric conditions, boiling is not a limiting factor for the performance of P-REx.

A further important result from the simulations is that P-REx achieves the best results for a ground layer adaptive optics system. Although the current interferometers do not have a GLAO system, this can be a promising possibility for the future, as a GLAO system in

combination with P-REx would not be limited by the sensitivity of the fringe tracker and could achieve a larger sky coverage with the use of laser guide stars. As P-REx should work even better with a GLAO system than with a SCAO system, a GLAO-LGS system with P-REx would significantly improve the sky coverage and the observing robustness in comparison to the existing SCAO systems.

Based on all the tests in this work, I come to the conclusion that the proposed piston reconstruction has good possibilities to work, especially for observations at infrared science wavelength, as they impose less tight constraints on the fringe stability. My tests fully exploited the simulations and the used single aperture LBT data to examine the performance of P-REx. In order to make final conclusions about the potential of P-REx and especially about the possible increase in sensitivity of an interferometer with this system, it is now necessary, and well motivated by this work, to further test P-REx with interferometric data, in combination with fringe tracking measurements.

The next step in order to explore the capabilities of P-REx is therefore to apply it to data from two telescopes of an interferometer and compare the results with the associated fringe tracking data. By doing this over longer timespans and over a wider range of atmospheric conditions than was possible within this thesis, the performance predictions of P-REx can be further improved.

The final goal is to apply the here developed techniques to an interferometric instrument. A good possibility for doing this would be the LBTI and the LINC-NIRVANA instruments, as the binocular telescope operation with the very short baseline offers the advantage to test the system with less additional noise due to long delay lines, and with full control of the vibrations in the telescope. Another possible instrument to apply P-REx to would be MATISSE, the mid-infrared spectro-interferometer for VLTI. As MATISSE observes in the mid-infrared, it imposes less constraints on the fringe stability and on the OPD noise. Increasing the coherence time for MATISSE operations would allow the observation of fainter targets, and at higher spectral resolution.

To conclude this work, I can summarize that the Piston Reconstruction Experiment is a promising technique for the interferometric instruments of the near future. In order to apply the system to an interferometer, there is still some research to do, but the results from this work clearly show the potential and the usability of the Piston Reconstruction Experiment.

APPENDICES

ZERNIKE RECONSTRUCTION



The usual way to describe optical aberrations, or in this case wave fronts, is with the help of Zernike polynomials. They were first introduced by F. Zernike in 1934 (Zernike 1934) and have the main advantage that they are already defined on a unit circle. Therefore, one can easily apply them on the circular shape of optical devices. Another advantage is that the lower orders of the Zernike polynomials represent the main properties and classical aberrations of a wavefront, such as for example tip, tilt, coma and astigmatism.

The Zernike polynomials are defined for an even and an odd case:

$$\begin{aligned} Z_n^m(\rho, \phi) &= R_n^m(\rho) \cos(m\phi) \\ Z_n^{-m}(\rho, \phi) &= R_n^m(\rho) \sin(m\phi) \end{aligned} \quad (\text{A.1})$$

where n and m are non-negative integers with $n \geq m$, ρ is the radial distance and ϕ the azimuthal angle. The radial part of the polynomials is defined as follows:

$$R_n^m(\rho) = \sum_{k=0}^{(n-m)/2} \frac{(-1)^k (n-k)!}{k! \left(\frac{n+m}{2} - k\right)! \left(\frac{n-m}{2} - k\right)!} \rho^{n-2k} \quad (\text{A.2})$$

for $(n-m)$ even, and $R_n^m(\rho) = 0$ for $(n-m)$ odd. The representation of the first 10 polynomials is shown in Figure A.1. A complete wavefront can then be reconstructed by the superposition of the individual polynomials:

$$\Psi(\rho, \phi) = \sum_{i=1}^{\infty} a_i Z_i(\rho, \phi) \quad (\text{A.3})$$

The Zernike polynomials can therefore be used to show a wavefront, but another essential problem is to reconstruct the wavefront from a SH WFS slope measurement. In order to do so, one has to calculate a reconstruction matrix, which directly maps the slopes into Zernike modes. This matrix is determined by calculating the two dimensional representation of an individual Zernike mode. By deriving the derivative of this representation in x and y direction, one gets the principal x and y slopes for each pixel. This two dimensional derivative has then to be mapped into the actual grid of the wavefront sensor lenslets. By doing this one gets for one individual Zernike mode a vector, which represents this mode in slope measurements. For a WFS with N lenslets this vector is given by the following representation: $Z_{sl,i} = (s_{x1}, s_{x2}, \dots, s_{xN}, s_{y1}, s_{y2}, \dots, s_{yN})$. The whole reconstruction matrix can then be calculated by doing this for every mode till the desired maximum mode M and writing the vectors into a matrix. One then has to calculate the pseudo-inverse of this matrix to get the calculation from given slopes to the Zernike polynomials:

$$\text{RECON} = [Z_{sl,1} \ Z_{sl,2} \ \dots \ Z_{sl,M}]^{-1} \quad (\text{A.4})$$

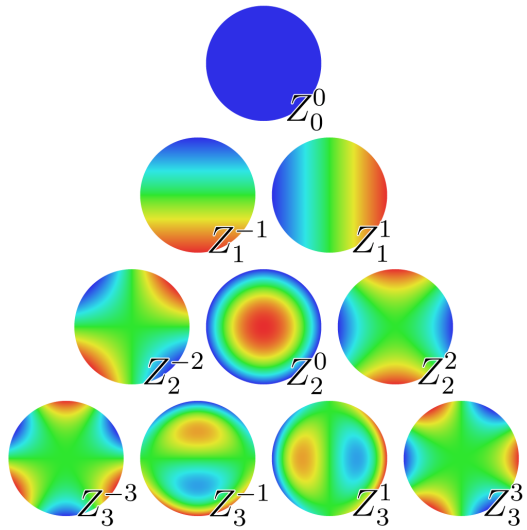


Figure A.1: Representation of the first 10 Zernike polynomials

The calculation of this matrix is comparably difficult and time expensive. However, one only has to calculate it once for a certain WFS, as the reconstruction can then be done by simply multiplying the reconstruction matrix with the measured slope vector.

CODE EXAMPLES



The code examples in the following are only snippets of a larger code, which shall demonstrate the principle and will most likely not work on their own. For the full working Python module behind this work see <https://github.com/widmannf>.

B.1 WIND DETECTION

This section shows the main functions that are needed in order to detect the shift between two images.

```
1 def winddetection(image, kernel, crop=5, size=0.5, laplace=False):
2     """
3         Function to detect the shift from to images Image & kernel),
4         using a cross correlation and a 2D Gaussian Fit
5         Input: the two images
6         Output: x and y shift in pixel
7     """
8     nxcorr = nxcorrelation(image, kernel, laplace=laplace)
9     maxpos = maxgauss(nxcorr, crop=crop, size=size)
10    x, y = [j-len(nxcorr)//2 for j in maxpos]
11    return x, y
12
13 # Sub functions for the winddetection
14 def nxcorrelation(kernel, image, pupil=None, laplace=True):
15     if laplace:
16         image2 = scipy.ndimage.filters.laplace(image)
17         kernel2 = scipy.ndimage.filters.laplace(kernel)
18     else:
19         image2 = image.astype(float)
20         kernel2 = kernel.astype(float)
21     xcorr = xcorrelation(kernel2, image2)
22
23     # If no pupil shape given, use quadratic array
24     if pupil is None:
25         ones1 = np.ones_like(image2)
26         ones0 = np.ones_like(kernel2)
27         onescorr = xcorrelation(ones0, ones1)
28     else:
29         if pupil.shape == image.shape:
30             onescorr = xcorrelation(pupil, pupil)
31
32     nxcorr = xcorr / (np.std(image2) * np.std(kernel2) * onescorr)
```

```

33     return nxcorr
34
35 def xcorrelation(image, kernel):
36     outdims = np.array([image.shape[dd]+kernel.shape[dd]-1 for
37                         dd in range(image.ndim)])
38     corr = fftpack.fftshift(fftpack.ifftn(np.multiply(fftpack.fftn
39                                         (image, outdims), np.conj(fftpack.fftn(kernel, outdims)))))
40     xcorr = np.abs(corr)
41     return xcorr
42
43 def maxgauss(nxcorr, crop=10, size=2):
44     maxpos = np.unravel_index(nxcorr.argmax(), nxcorr.shape)
45     # Cut image to get a better result
46     smallnxcorr = nxcorr[maxpos[0]-crop:maxpos[0]+crop,
47                           maxpos[1]-crop:maxpos[1]+crop]
48     smalldimx = smallnxcorr.shape[0]
49     smalldimy = smallnxcorr.shape[1]
50
51     # Renew fit boundaries
52     initial_guess = (0.7, smalldimx/2, smalldimy/2, size, size, 0, 0)
53     x = np.linspace(0, smalldimx-1, smalldimx)
54     y = np.linspace(0, smalldimy-1, smalldimy)
55     x, y = np.meshgrid(x, y)
56     smallnxcorr = smallnxcorr.reshape(smalldimx*smalldimy)
57     popt, pcov = opt.curve_fit(_2Dgauss, (x, y), smallnxcorr,
58                                 p0=initial_guess)
59     popt[2] += (maxpos[0]-crop)
60     popt[1] += (maxpos[1]-crop)
61
62     return popt[2], popt[1]

```

B.2 P-REX

The code here shows the piston reconstruction experiment as used for the tip tilt method. The main part is the wind detection from the previous code.

```

1 def prex(datacube, average, windaverage=1, crop=5, size=0, 5):
2     """
3         Function to calculate the differential piston from slope data
4         using the Tip-Tilt concept
5
6         input data:
7             datacube: list with 2D xslopes data, 2D yslopes, tip and tilt
8             average: number of images for the average
9             windaverage: set to use a larger average for the wind value
10
11        output: List of differential piston
12        """
13        xslopes = datacube[0]
14        yslopes = datacube[1]

```

```
15     tip = datacube[2]
16     tilt = datacube[3]
17
18     difpiston = []
19     tiplist = []
20     tiltlist = []
21     maxx = []
22     maxy = []
23     for i in range(0, len(tip)-average, average):
24         image_x = np.mean(xslopes[i:i+average], axis=0)
25         kernel_x = np.mean(xslopes[i+average:i+2*average], axis=0)
26         nxcorr_x = nxcorrelation(image_x, kernel_x, laplace=False)
27         image_y = np.mean(yslopes[i:i+average], axis=0)
28         kernel_y = np.mean(yslopes[i+average:i+2*average], axis=0)
29         nxcorr_y = nxcorrelation(image_y, kernel_y, laplace=False)
30         nxcorr = (nxcorr_x+nxcorr_y)/2
31         maxpos = maxgauss(nxcorr, crop=crop, size=size)
32         x, y = [j-len(nxcorr)//2 for j in maxpos]
33
34         maxx.append(x)
35         maxy.append(y)
36         av_tip = np.mean(tip[i:i+2*average])
37         av_tilt = np.mean(tilt[i:i+2*average])
38
39         if windaverage != 1:
40             difpiston.append(av_tip * np.mean(maxy[-windaverage:])+av_tilt * np.mean(maxx[-windaverage:])))
41         else:
42             difpiston.append(av_tip * y + av_tilt * x)
43
44     return difpiston
```


YAO PARAMETER FILES



In the following two parameter files for the YAO simulation are shown. The first one simulates a typical single-conjugated adaptive optics system with a NGS. The second one is a full ground layer adaptive optics system with four LGSSs and one NGS for the tip and tilt measurement.

C.1 SCAO SYSTEM

```
1 //-----
2 sim.name      = "SCAO example , 20x20 SH-WFS";
3 sim.pupildiam = 200;
4 sim.debug     = 0;
5 sim.verbose   = 0;
6 go_quiet     = 1;
7 //-----
8 atm.dr0at05mic = 40;
9 atm.screen     = &("screen_" +["1","2","3","4","5","6","7","8"]+ ".fits");
10 atm.layeralt   = &([0,400,1000,1800.,2500.,5000.,8000.,13000.]);
11 atm.layerspeed  = &([10.,12.,10.,8.,6.,10.,20.,20.]);
12 atm.layerfrac   = &([0.45,0.13,0.11,0.09,0.06,0.05,0.04,0.07]);
13 atm.winddir     = &([45,50,40,35,30,40,55,65]);
14 //-----
15 tel.diam       = 8;
16 tel.cobs       = 0.;
17 //-----
18 nwfs           = 1;
19 wfs = array(wfss,nwfs);
20 n   = 1;
21 wfs(n).type    = "hartmann";
22 wfs(n).lambda   = 0.65;
23 wfs(n).gpos     = [0.,0.];
24 wfs(n).gsalt    = 0.;
25 wfs(n).gsmag    = 5.;
26 wfs(n).shmethod  = 2;
27 wfs(n).shnxsub  = 20;
28 wfs(n).pixsize   = 0.3;
29 wfs(n).npixels   = 10;
30 wfs(n).noise     = 1;
31 wfs(n).ron       = 6.0;
32 wfs(n).shthreshold = 0.;
```

```

33 wfs(n).nintegcycles = 1;
34 //-----
35 ndm = 1;
36 dm = array(dms,ndm);
37 n = 1;
38 dm(n).type = "stackarray";
39 dm(n).iffile = "";
40 dm(n).nxact = 20;
41 dm(n).pitch = 10;
42 dm(n).alt = 0.;
43 dm(n).unitpervolt = 0.01;
44 dm(n).push4imat = 100;
45 dm(n).elt = 1;
46 //-----
47 mat.condition = &([50.]);
48 mat.file = "";
49 //-----
50 target.lambda = &([2.20]);
51 target.xposition = &([0.]);
52 target.yposition = &([0]);
53 target.dispzoom = &([1.]);
54 //-----
55 loop.gain = 0.6;
56 loop.framedelay = 1;
57 loop.niter = 1000;
58 loop.ittime = 2e-3;
59 loop.startskip = 10;
60 loop.skipevery = 1000;
61 loop.skipby = 10000;

```

C.2 GLAO SYSTEM

```

1 //-----
2 sim.name = "GLAO example, 4 20x20 SHWFS, \w TT subsystem";
3 sim.pupildiam = 200;
4 sim.debug = 0;
5 sim.verbose = 0;
6 go_quiet = 1;
7 //-----
8 atm.dr0at05mic = 40;
9 atm.screen = &("screen_" + [ "1" , "2" , "3" , "4" , "5" , "6" , "7" , "8" ] + ".fits");
10 atm.layeralt = &([0,400,1000,1800.,2500.,5000.,8000.,13000.]);
11 atm.layerspeed = &([10.,12.,10.,8.,6.,10.,20.,20.]);
12 atm.layerfrac = &([0.45,0.13,0.11,0.09,0.06,0.05,0.04,0.07]);
13 atm.winddir = &([45,50,40,35,30,40,55,65]);
14 //-----
15 tel.diam = 8;
16 tel.cobs = 0.;
17 //-----
18 nwfs = 5;
19 wfs = array(wfss,nwfs);

```

```

20 // subsystem 1, TT detection
21 n = 1;
22 wfs(n).type          = "hartmann";
23 wfs(n).subsystem     = 1;
24 wfs(n).lambda        = 0.65;
25 wfs(n).gpos           = [ 0., 0.];
26 wfs(n).gsalt          = 0.;
27 wfs(n).gsmag          = 5.;
28 wfs(n).shmethod       = 2;
29 wfs(n).shnxsub        = 2;
30 wfs(n).pixsize        = 0.5;
31 wfs(n).npixels         = 4;
32 wfs(n).shthreshold    = 0.;
33 wfs(n).nintegcycles   = 1;
34 wfs(n).noise           = 1;
35 wfs(n).ron             = 6.0;
36 // subsystem 2, GLAO
37 for (n=2;n<=5;n++) {
38     wfs(n).type          = "hartmann";
39     wfs(n).subsystem     = 2;
40     wfs(n).lambda        = 0.65;
41     wfs(n).gsalt          = 12000.;
42     wfs(n).laserpower    = 22.;
43     wfs(n).filtertilt    = 1;
44     wfs(n).correctUpTT   = 1;
45     wfs(n).uplinkgain    = 0.1;
46     wfs(n).shmethod       = 2;
47     wfs(n).shnxsub        = 20;
48     wfs(n).pixsize        = 0.3;
49     wfs(n).npixels         = 10;
50     wfs(n).noise           = 1;
51     wfs(n).ron             = 6.0;
52     wfs(n).shthreshold    = 0.;
53     wfs(n).nintegcycles   = 1;
54 }
55 wfs(2).gpos           = [ 60., 0.];
56 wfs(3).gpos           = [ 0., 60.];
57 wfs(4).gpos           = [ -60., 0.];
58 wfs(5).gpos           = [ 0., -60.];
59 //-----
60 ndm = 2;
61 dm = array(dms,ndm);
62 n = 1;
63 dm(n).type            = "tiptilt";
64 dm(n).subsystem        = 1;
65 dm(n).iffile           = "";
66 dm(n).alt              = 0.;
67 dm(n).unitpervolt      = 0.0005;
68 dm(n).push4imat        = 10;
69 dm(n).gain              = 0.3;
70 n = 2;
71 dm(n).type            = "stackarray";

```

```
72 dm(n).subsystem      = 2;
73 dm(n).iffile         = " ";
74 dm(n).nxact          = 20;
75 dm(n).pitch          = 10;
76 dm(n).alt             = 0.;
77 dm(n).unitpervolt    = 0.01;
78 dm(n).push4imat     = 100;
79 dm(n).elt             = 1;
80 //-----
81 mat.condition        = &([50.,50.]);
82 mat.file             = " ";
83 //-----
84 target.lambda        = &([2.23]);
85 target.xposition     = &([0.]);
86 target.yposition     = &([0]);
87 target.dispzoom      = &([1.]);
88 //-----
89 loop.gain            = 0.6;
90 loop.framedelay      = 1;
91 loop.niter           = 1000;
92 loop.ittime          = 2e-3;
93 loop.startskip       = 10;
94 loop.skipevery      = 1000;
95 loop.skipby          = 10000;
96 loop.method          = "closed-loop";
```

LIST OF FIGURES

2.1	Image of a point source disturbed by the atmosphere	5
2.2	Example of a typical $C_N^2(h)$ profile	7
2.3	Comparison of Kolmogorov and van Karman spectrum	8
2.4	Example for a wind speed profile	11
2.5	Evolution of the maximum value of the deconvolution peak	13
2.6	Cross correlation with increasing time difference	13
3.1	Sketch of a simple AO system	16
3.2	Principle of a Shack-Hartmann wavefront sensor	17
3.3	Principle of a Pyramid WFS	18
3.4	Principle of a curvature WFS	18
3.5	Scheme of a GLAO and MCAO system	21
4.1	Interference pattern of a double-slit experiment	24
4.2	Geometry of light propagation for the Van Cittert-Zernike theorem . .	25
4.3	Schematic presentation of an interferometer with two telescopes	26
4.4	Measurement of the group delay in a fringe tracker	30
4.5	Fringe tracker performance for different star magnitudes	32
4.6	OPD residuals and optimal frequency for different magnitudes	33
5.1	Schematic representation of the two P-REx concepts	37
5.2	P-REx concept in 1D	38
5.3	Sketch for the use of P-REx	41
7.1	Comparison of the two cross correlation methods	49
7.2	Atmospheric time series from YAO	49
7.3	Normalized cross correlation	50
7.4	Normalized cross correlation with Laplace filter	50
7.5	Multilayer detection	51
7.6	Wind detection from SH data	53
7.7	Wind detection from a curvature WFS	54
7.8	Error of the wind measurement	55
8.1	Workflow of a YAO simulation	58
8.2	Differential piston from first simulations	60
8.3	Reconstructed piston from first simulations	60
8.4	Histogram of piston reconstruction	61
8.5	Example of the wavefront reconstruction	62
8.6	Dependency of piston reconstruction on the atmosphere	64

8.7	Dependency of the piston reconstruction on the time average	65
8.8	Wind determination with moving average	66
8.9	Dependency of the piston reconstruction on the guide star luminosity .	67
8.10	Dependency of the piston reconstruction on spatial sampling	67
8.11	P-REx performance for different SCAO systems	68
8.12	Dependency of the piston reconstruction on the layer of the atmosphere	70
9.1	P-REx performance for a SCAO systems	72
9.2	P-REx performance for a SCAO systems with moving average	72
9.3	Piston reconstruction for a SCAO system	74
9.4	P-REx performance for a GLAO systems	75
9.5	P-REx performance for a GLAO systems with moving average	75
9.6	Piston reconstruction for a GLAO system	76
9.7	Wind detection from a MCAO system	77
10.1	Wind measurement from FLAO data	82
10.2	Wind measurement from simulated FLAO data	82
10.3	Comparison of the wind velocity measurement	83
10.4	Evolution of the correlation peak over time	84
10.5	Evolution of the mean correlation peak over time	85
11.1	Explanation of the single aperture mode	88
11.2	Single aperture method for YAO simulation	90
11.3	Single aperture mode on LBT FLAO data	91
11.4	RMS error of the 12 FLAO datasets	92
11.5	Statistics of the single aperture mode with LBT FLAO data	94
A.1	Representation of the first 10 Zernike polynomials	102

LIST OF TABLES

2.1	Example values for seeing and the fried parameter	9
2.2	Composition of a multilayer atmosphere	12
3.1	Basic properties of current AO systems at VLTI and LBT	22
8.1	Properties of the AO system for general tests	59
8.2	Uncertainty ranges for the piston reconstruction	63
9.1	Wind measurements for different AO systems	73
10.1	Properties of the FLAO data	81
11.1	Properties of the atmosphere from FLAO data	92

BIBLIOGRAPHY

- Akondi, Vyas, Castillo, Sara, and Vohnsen, Brian; **2013**. *Opt. Express*, 21, pp. 18261–18272.
- Andersen, D. R. et al.; **2006**. *The Publications of the Astronomical Society of the Pacific*, 118, pp. 1574–1590.
- Arsenault, R. et al.; **2003**. *Proc. SPIE*, 4839, pp. 174–185.
- Assémat, François, Wilson, Richard W., and Gendron, Eric; **2006**. *Opt. Express*, 14, pp. 988–999.
- Avila, R., Masciadri, E., Vernin, J., and Sánchez, L. J.; **2004**. *The Publications of the Astronomical Society of the Pacific*, 116, pp. 682–692.
- Avila, R. et al.; **2006**. *The Publications of the Astronomical Society of the Pacific*, 118, pp. 503–515.
- Berdja, A. and Borgnino, J.; **2007**. *Monthly Notice of the Royal Astronomical Society*, 378, pp. 1177–1186.
- Bertram, T. et al.; **2006**. *Proc. SPIE*, 6268, 62683P.
- Bharmal, N. A.; **2015**. *Journal of Physics: Conference Series*, 595, p. 012003.
- Briechle, Kai and Hanebeck, Uwe D.; **2001**. *Proc. SPIE*, 4387, pp. 95–102.
- Buscher, D. F.; **2015**. *Practical Optical Interferometry*.
- Buscher, D. F. et al.; **1995**. *Applied Optics LP*, 34, p. 1081.
- Cassen, P., Guillot, T., and Quirrenbach, A.; **2007**. *Extrasolar Planets: Saas Fee Advanced Course 31*. Saas-Fee Advanced Course. Springer Berlin Heidelberg. ISBN: 9783540314707.
- Choquet, E. et al.; **2010**. *Proc. SPIE*, 7734, 77341Z.
- Choquet, É. et al.; **2014**. *Astronomy & Astrophysics*, 569, A2.
- Clénet, Y. et al.; **2010**. *Proc. SPIE*, 7736, 77364A.
- Conan, R., Ziad, A., Borgnino, J., Martin, F., and Tokovinin, A. A.; **2000**. *Proc. SPIE*, 4006, pp. 963–973.
- Conan, R. et al.; **2002**. *Astronomy & Astrophysics*, 396, pp. 723–730.
- Cortés, A. et al.; **2013**, p. 81.
- Cox, A. N. and Pilachowski, C. A.; **2000**. *Physics Today*, 53, p. 77.
- Dai, Guang ming; **1996**. *J. Opt. Soc. Am. A*, 13, pp. 1218–1225.
- Davies, R. and Kasper, M.; **2012**. *Annual Review of Astronomy and Astrophysics*, 50, pp. 305–351.
- Defrère, D. et al.; **2014**. *Improving the Performances of Current Optical Interferometers & Future Designs*, pp. 37–44.
- Egner, S. E., Masciadri, E., McKenna, D., Herbst, T. M., and Gaessler, W.; **2006**. *Proc. SPIE*, 6272, p. 627257.
- Esposito, S. and Riccardi, A.; **2001**. *Astronomy & Astrophysics*, 369, pp. L9–L12.
- Esposito, S. et al.; **2012**. *Proc. SPIE*, 8447, 84470U.
- Fried, D. L.; **1965**. *Journal of the Optical Society of America*, 55, pp. 1427–1431.
- Gai, M. et al.; **2004**. *Proc. SPIE*, 5491, p. 528.

- Gendron, E. and Léna, P.; **1996**. *Astrophysics and Space Science*, 239, pp. 221–228.
- Gentry, Bruce M., Chen, Huailin, and Li, Steven X.; **2000**. *Optics Letters*, 25, pp. 1231–1233.
- Glindemann, A.; **2011**. *Principles of Stellar Interferometry*.
- Gonté, F. Y. J. et al.; **2016**. *Proc. SPIE*, 9907, p. 990720.
- GRAVITY Collaboration; **2017**. *ArXiv e-prints*,
- Guesalaga, A., Neichel, B., Cortés, A., Béchet, C., and Guzmán, D.; **2014**. *Monthly Notices of the Royal Astronomical Society*, 440, pp. 1925–1933.
- Guyon, O.; **2005**. *The Astrophysical Journal*, 629, pp. 592–614.
- Haniff, C.; **2007**. *New Astronomy Reviews*, 51, pp. 565–575.
- Hardy, J. W.; **1998**. *Adaptive Optics for Astronomical Telescopes*. Oxford series in optical and imaging sciences. Oxford University Press.
- Herbst, T. M., Ragazzoni, R., Eckart, A., and Weigelt, G.; **2012**. *Proc. SPIE*, 8445, p. 84450V.
- Hinz, P. M. et al.; **2016**. *Proc. SPIE*, 9907, p. 990704.
- Jackson, Neal; **2008**. “Principles of interferometry.” In: *Jets from Young Stars II: Clues from High Angular Resolution Observations*, Lect. Notes Phys. 742. Ed. by F. Bacciotti, E. Whelan, and L. Testi. Springer.
- Jähne, B.; **2005**. *Digital Image Processing*. Springer Berlin Heidelberg.
- Jenkins, Gwilym M. and Watts, Donald G.; **1968**. *Spectral analysis and its applications*. eng. Holden-Day, XVIII, 525 S.
- Kendrew, S. et al.; **2012**. *Proc. SPIE*, 8446, 84467W.
- Le Bouquin, J.-B. et al.; **2008**. *Proc. SPIE*, 7013, p. 701318.
- Lewis, John P; **1995a**. “Fast template matching.” In: *Vision interface*. Vol. 95. 120123, pp. 15–19.
- Lewis, JP; **1995b**. “Fast normalized cross-correlation.” In: *Vision interface*. Vol. 10. 1, pp. 120–123.
- Lippa, M. et al.; **2016**. *Proc. SPIE*, 9907, p. 990722.
- Madec, P.-Y.; **2012**. *Proc. SPIE*, 8447, p. 844705.
- Marchetti, E. et al.; **2008**. *Proc. SPIE*, 7015, 70150F.
- Masciadri, E., Stoesz, J., Hagelin, S., and Lascaux, F.; **2010**. *Monthly Notice of the Royal Astronomical Society*, 404, pp. 144–158.
- Meisner, J. A., Jaffe, W. J., and Le Poole, R. S.; **2012**, 8445, p. 84451L.
- Menu, J., Perrin, G., Choquet, E., and Lacour, S.; **2012**. *Astronomy & Astrophysics*, 541, A81.
- Mérand, A., Patru, F., Berger, J.-P., Percheron, I., and Poupar, S.; **2012**. *Proc. SPIE*, 8445, 84451K.
- Monnier, J. D.; **2003**. *Reports on Progress in Physics*, 66, pp. 789–857.
- Müller, A. et al.; **2014**. *Astronomy & Astrophysics*, 567, A98.
- Noll, R. J.; **1976**. *Journal of the Optical Society of America (1917-1983)*, 66, pp. 207–211.
- Peters, M. A. et al.; **2008**. *Proc. SPIE*, 7015, 70156G.
- Pfuhl, O. et al.; **2010**. *Proc. SPIE*, 7734, 77342A.
- Pott, J. U., Fu, Q., Widmann, F., and Peter, D.; **2016**. *Proc. SPIE*, 9907, 99073E–14.
- Poyneer, L., van Dam, M., and Véran, J.-P.; **2009**. *Journal of the Optical Society of America A*, 26, p. 833.
- Rabien, S. et al.; **2010**. *Proc. SPIE*, 7736, 77360E–77360E–12.
- Ragazzoni, Roberto; **1996**. *Journal of Modern Optics*, 43, pp. 289–293.
- Reddy, B. S. and Chatterji, B. N.; **1996**. *Trans. Img. Proc. 5*, pp. 1266–1271.
- Rigaut, F. and Van Dam, M.; **2013**. *Proceedings of the Third AO4ELT Conference*, p. 18.

- Rigaut, F. et al.; **2014**. *Monthly Notice of the Royal Astronomical Society*, 437, pp. 2361–2375.
- Roddier, F.; **1981**. *Progress in optics*, 19, pp. 281–376.
- Roddier, F. and Roddier, C.; **1988**. *European Southern Observatory Conference and Workshop Proceedings*, 30, p. 667.
- Rohlfs, K. and Wilson, T. L.; **1996**. *Tools of Radio Astronomy*. Springer.
- Roopashree, MB, Vyas, Akondi, and Prasad, B Raghavendra; **2013**. *Journal of the Indian Institute of Science*, 93, pp. 67–84.
- Sahlmann, J. et al.; **2009**. *Astronomy & Astrophysics*, 507, pp. 1739–1757.
- Saint-Jacques, D.; **1998**. *PhD thesis, Cambridge University*,
- Saint-Jacques, D. and Baldwin, J. E.; **2000**. *Proc. SPIE*, 4006, pp. 951–962.
- Scargle, J. D.; **1989**. *The Astrophysical Journal*, 343, pp. 874–887.
- Schöck, M. and Spillar, E. J.; **2000**. *J. Opt. Soc. Am. A*, 17, pp. 1650–1658.
- Schöck, Matthias and Spillar, Earl J.; **1998**. *Opt. Lett.* 23, pp. 150–152.
- Straubmeier, C. et al.; **2006**. *Proc. SPIE*, 6268, p. 62681I.
- Tango, W. J. and Twiss, R. Q.; **1980**. *Progress in optics*, 17, pp. 239–277.
- Tatarskii, V. I.; **1961**. *Wave Propagation in Turbulent Medium*. McGraw-Hill.
- Taylor, G. I.; **1938**. *Proceedings of the Royal Society*, 164, pp. 476–490.
- Thompson, A. R., Moran, J. M., and Swenson Jr., G. W.; **2017**. *Interferometry and Synthesis in Radio Astronomy, 3rd Edition*.
- Tokovinin, A. and Travouillon, T.; **2006**. *Monthly Notice of the Royal Astronomical Society*, 365, pp. 1235–1242.
- Tyson, R.K.; **2015**. *Principles of Adaptive Optics, Fourth Edition*. CRC Press.
- Wang, Jianfeng, Liu, Ke, Li, Yanqiu, Wang, Hai, and Li, Guanghui; **2011**. *Proc. SPIE*, 8197, 81970A.
- Wilson, R. W.; **2002**. *Monthly Notice of the Royal Astronomical Society*, 337, pp. 103–108.
- Woillez, J. et al.; **2014**, 9146, 91461H.
- Zernike, v. F.; **1934**. *Physica*, 1, pp. 689–704.

ERKLÄRUNG

Ich versichere, dass ich diese Arbeit selbstständig verfasst habe und keine anderen als die angegebenen Quellen und Hilfsmittel benutzt habe.

Heidelberg, July 25, 2017

Felix Widmann